

General Disclaimer

One or more of the Following Statements may affect this Document

- This document has been reproduced from the best copy furnished by the organizational source. It is being released in the interest of making available as much information as possible.
- This document may contain data, which exceeds the sheet parameters. It was furnished in this condition by the organizational source and is the best copy available.
- This document may contain tone-on-tone or color graphs, charts and/or pictures, which have been reproduced in black and white.
- This document is paginated as submitted by the original source.
- Portions of this document are not fully legible due to the historical nature of some of the material. However, it is the best reproduction available from the original submission.

PB82-229220

**Exploitation of SAR Data for Measurement of
Ocean Currents and Wave Velocities**

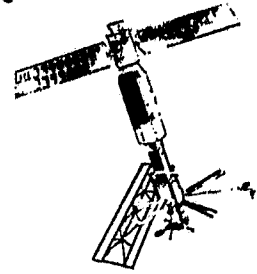
**Environmental Research Inst. of Michigan
Ann Arbor**

Prepared for

**National Earth Satellite Service
Washington, DC**

Sep 81

**U.S. Department of Commerce
National Technical Information Service
NTIS**



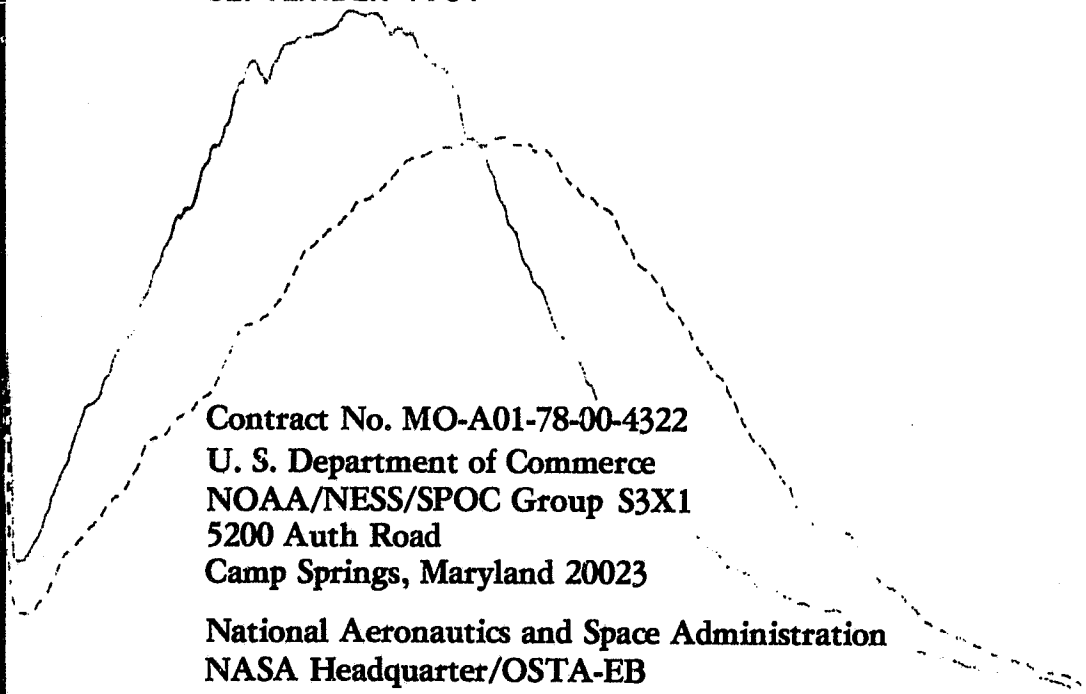
137600-1-F

Final Report

EXPLOITATION OF SAR DATA FOR MEASUREMENT OF OCEAN CURRENTS AND WAVE VELOCITIES

R. A. SHUCHMAN, D. R. LYZENGA,
and A. KLOOSTER, JR.
Radar and Optics Division

SEPTEMBER 1981



Contract No. MO-A01-78-00-4322
U. S. Department of Commerce
NOAA/NESS/SPOC Group S3X1
5200 Auth Road
Camp Springs, Maryland 20023

National Aeronautics and Space Administration
NASA Headquarter/OSTA-EB
600 Independence Avenue
Washington D. C. 20546

ENVIRONMENTAL
RESEARCH INSTITUTE OF MICHIGAN
BOX 8618 • ANN ARBOR • MICHIGAN 48107

TECHNICAL REPORT STANDARD TITLE PAGE

1. Report No.	2. Government Accession No.	PB82-229220	
4. Title and Subtitle Exploitation of SAR Data for Measurement of Ocean Currents and Wave Velocities		5. Report Date September 1981	6. Performing Organization Code
7. Author(s) R. A. Shuchman, D. R. Lyzenga and A. Klooster		8. Performing Organization Report No. 137600-1-F	
9. Performing Organization Name and Address Environmental Research Institute of Michigan Radar and Optics Division P. O. Box 8618 Ann Arbor, MI 48107		10. Work Unit No.	11. Contract or Grant No. MO-A01-78-00-4322
12. Sponsoring Agency Name and Address U. S. Department of Commerce NOAA/NESS/SPOC Group S3X1 5200 Auth Road Camp Springs, Maryland 20023		13. Type of Report and Period Covered Final Report 15 August 1978 through 1 September 1981	
15. Supplementary Notes The NOAA Technical Monitor for this report was Clifford Rufenach		14. Sponsoring Agency Code	
16. Abstract This report discusses methods of extracting information on ocean currents and wave orbital velocities from SAR data by an analysis of the Doppler frequency content of the data. The theory and data analysis methods are discussed, and results are presented for both aircraft and satellite (Seasat) data sets. A method of measuring the phase velocity of a gravity wave field is also described. This method uses the shift in position of the wave crests on two images generated from the same data set using two separate Doppler bands. Results of the current measurements are presented for 11 aircraft data sets and 4 Seasat data sets. Positive results have been obtained using aircraft X-band data for currents ranging from 0.5 to 2.0 m/sec. Results obtained from Seasat data are mixed, but are encouraging in view of the non-optimum configuration of the Seasat SAR for this application. Considerations are discussed for the design of a more optimum satellite SAR system for measuring ocean currents. Limited results of the orbital velocity and phase velocity measurements are presented using two aircraft data sets. Preliminary results are positive but further evaluation of these methods is needed.			
17. Key Words Synthetic aperture radar Oceanography Currents Doppler shift		18. Distribution Statement The distribution of this report is unlimited.	
19. Security Classif. (of this report) Unclassified	20. Security Classif. (of this page) Unclassified	21. No. of Pages xi + 118	22. Price

PREFACE

The work described in this report was conducted by the Radar and Optics Division of the Environmental Research Institute of Michigan (ERIM). This work was jointly supported by the National Oceanic and Atmospheric Administration (NOAA) and the National Aeronautics and Space Administration (NASA) as part of the Seasat Announcement of Opportunity Program under Contract No. MO-A01-78-00-4322. This report summarizes the entire contract performance period which commenced on 15 August 1978 and was completed 1 September 1981. The Technical Monitors for this project were Clifford L. Rufenach and John W. Sherman III of NOAA.

The Principal Investigator for the project was Robert A. Shuchman. Technical contributions were made by David R. Lyzenga in the development of the theoretical basis for the investigations, and by Alex Klooster in making the SAR optical measurements.

This project was a joint research effort between ERIM and NOAA scientists. Specifically, Clifford L. Rufenach of the Boulder NOAA/Environmental Research Laboratory (ERL) and Frank I. Gonzalez of NOAA/Pacific Marine Environmental Laboratory (PMEL) contributed their expertise in interpreting the SAR Doppler phase histories analyzed in year one.

ACKNOWLEDGEMENTS

The timely analysis of satellite data is never possible without the cooperation of many people. It is a pleasure to specifically acknowledge the help of the following individuals: Clifford Rufenach of the Boulder NOAA/ERL Laboratory for his contribution to the theory and his review of the overall report; Frank Gonzalez of NOAA/PMEL for providing oceanographic sea truth and reduction of the first year Doppler current measurements; James Gower of the Institute of Ocean Sciences (IDS) at Patricia Bay, British Columbia for providing sea truth information; the staff at the Jet Propulsion Laboratory (JPL), in particular, Walter Brown and Benjamin Holt, for providing Seasat SAR data in a timely manner; and Robert Gray of the Canadian Communications Research Centre (CRC) for providing complex (I and Q) Seasat SAR data of the Cape Flattery Test Site. Ralph Mitchell, Ralph Hamilton, Jack Walker, and Richard Larson of ERIM are thanked for reviewing this report.

TABLE OF CONTENTS

PREFACE	iii
ACKNOWLEDGEMENTS	v
LIST OF FIGURES	ix
LIST OF TABLES	xi
1.0 INTRODUCTION	1
2.0 BACKGROUND	3
3.0 CURRENT AND ORBITAL VELOCITY MEASUREMENTS	7
3.1 Theory of Doppler Analysis Methods	8
3.2 Data Set Description	16
3.3 Current Measurements	19
3.4 Orbital Velocity Measurements	54
3.5 Error Analysis	58
3.5.1 Anisotropic Scattering	59
3.5.2 Recording System Non-uniformities	61
3.5.3 Recording System MTF and Noise	62
3.5.4 Aperture and Illumination Effects	63
4.0 PHASE VELOCITY MEASUREMENTS	69
4.1 Theory	69
4.2 Measurements	71
5.0 CONCLUSIONS AND RECOMMENDATIONS	79
REFERENCES	83
APPENDIX A: THE FEASIBILITY OF MEASUREMENT OF OCEAN SURFACE CURRENTS USING SYNTHETIC APERTURE RADAR	A-1
APPENDIX B: OCEAN SURFACE CURRENT DETECTION BY SYNTHETIC APERTURE RADAR	B-1
APPENDIX C: SEASAT SAR OCEAN SURFACE CURRENT AND SHALLOW WATER WAVE REFRACTION	C-1

LIST OF FIGURES

1. Simplified Schematic Diagram of a SAR Optical Processing System . . .	5
2. SAR Viewing Geometry for a Point Target	9
3. Example of Doppler Spectrum Broadening Due to Wave Orbital Velocity, for Three Values of the Scaled Wave Amplitude $\left(\frac{\Omega a}{\beta v}\right)$	15
4. Doppler Spectra for Marineland (Pass 1) X-band Data	21
5. Doppler Spectra for Marineland (Pass 1) L-band Data	22
6. Doppler Spectra for Marineland (Pass 3) X-band Data	23
7. Doppler Spectra for Marineland (Pass 7) X-band Data	24
8. Doppler Spectra for Marineland (Pass 7) L-band Data	25
9. Doppler Spectra for Gulf Stream (Pass 13) X-band Data	27
10. Doppler Spectra for Porlier Pass (Pass 6) X-band Data	28
11. Doppler Spectra for Active Pass (Pass 10) X-band Data	29
12. Doppler Spectra for Active Pass (Pass 11) X-band Data	30
13. Doppler Spectra for Active Pass (Pass 12) X-band Data	31
14. Aircraft X-band Modulation Transfer Function for CV-580 Data . . .	35
15. Digitally Recorded and Corrected Doppler Spectra for Porlier Pass X-band Aircraft Data	36
16. Digitally Recorded and Corrected Doppler Spectra for Porlier Pass L-band Aircraft Data	37
17. Seasat System Modulation Transfer Function as Measured on the ERIM Optical Processor	39
18. (a) Doppler Spectrum for Columbia River (Seasat Orbit 150)	40
(b) Doppler Spectrum for Land Area Adjacent to Columbia River (Seasat Orbit 150)	41
19. (a) Doppler Spectrum for Dover Straits Area 1 (Seasat Orbit 762)	43
(b) Doppler Spectrum for Dover Straits Area 2 (Seasat Orbit 762)	44
(c) Doppler Spectrum for Land North of Dover Straits (Seasat Orbit 762)	45

LIST OF FIGURES
(Concluded)

20.	(a) Doppler Spectrum for Stationary Water Area Off Florida Coast (Seasat Orbit 651)	46
	(b) Doppler Spectrum for Gulf Stream Off Florida Coast (Seasat Orbit 651)	47
21.	(a) Doppler Spectrum for Land Area in Digitally Processed Data Set for Straits of Juan de Fuca (Seasat Orbit 681)	49
	(b) Doppler Spectrum for High-Signal Water Area in Digitally Processed Data Set for Straits of Juan de Fuca (Seasat Orbit 681)	50
	(c) Doppler Spectrum for Low-Signal Water Area in Digitally Processed Data Set for Straits of Juan de Fuca (Seasat Orbit 681)	51
22.	Doppler Centroid Versus Range Sample Number for Internal Wave Pattern in Straits of Juan de Fuca	55
23.	Signal Amplitude Versus Range Sample Number for Internal Wave Pattern in Straits of Juan de Fuca	56
24.	Doppler Broadening Factor Versus Scaled Wave Amplitude $\left(\frac{\Omega a}{\beta v}\right)$ for Aircraft X-band Aircraft Data with Antenna Beamwidth of 1.1° and Platform Velocity of 75 m/sec	57
25.	Doppler Spectra Measured for Goldstone Antenna with Image of Antenna (a) at Left Edge of Aperture, (b) Centered in Aperture, and (c) at Right Edge of Aperture	66
26.	Doppler Spectrum for Mainland (Pass 2) L-band Data	73
27.	Correlation Function for Mainland Image Files 1 and 2	76
28.	Correlation Function for Mainland Image Files 3 and 4	78

LIST OF TABLES

1. Summary of Aircraft Data Sets Selected for Doppler Analysis	17
2. Summary of Seasat Data Sets Selected for Doppler Analysis	18
3. Doppler Spectrum Statistics for Three Test Areas in Seasat Orbit 681 Digital Data Set	52
4. Frequency Bands and Corresponding Times for Four Marineland Image Files	72

1
INTRODUCTION

This report describes the present status of several closely related, ongoing investigations of the use of synthetic aperture radar (SAR) data for oceanographic purposes. The common element in these investigations is that they make use of information which is contained within the data recorded by the SAR system but which is not, for the most part, preserved in the processed SAR imagery. The object of these investigations is to obtain information on the motion of the water surface, including currents, orbital velocities and phase velocities of surface gravity waves. Data analysis methods and results are presented for various SAR systems, including both aircraft and satellite platforms.

Two general types of analysis are described in this report. Section 2 provides the background for both analysis techniques by discussing the general principles of SAR data collection and processing. Section 3 describes the Doppler analysis methods which are being investigated for the extraction of current and wave orbital velocity information. Section 4 describes the use of Doppler filtering techniques for measuring phase velocities. Section 5 summarizes the present status of these investigations and makes recommendations for further research.

2
BACKGROUND

A brief description of a synthetic aperture radar (SAR) system, including the data collection and processing methods used for reconstructing an image of the scene, is presented in this section. A more detailed description of the processing methods for extracting current and wave velocity information is contained in the following sections. The system described here uses optical recording and processing methods, but the basic principles involved apply to both optical and digital systems.

A SAR system consists of a pulsed microwave transmitter and receiver mounted in an airborne or spaceborne platform, a recording system, and a ground-based processor. The transmitter sends out a series of short coherent pulses in the broadside direction. These pulses are scattered from the surface and the reflected pulses are received and recorded by the SAR. By time-gating the received pulses, using pulse compression techniques in some cases, a fine resolution is obtained in the cross-track direction.

The method by which the scene is resolved in the along-track direction is the principal difference between synthetic-aperture and real-aperture radars. In a real-aperture radar, each pulse is taken as an independent sample of the scene. The along-track resolution is therefore determined by the antenna beamwidth, which is inversely proportional to the physical length of the antenna. Thus, a large antenna is needed to achieve an acceptable resolution in the along-track direction. In a synthetic aperture radar, a comparable resolution can be obtained using a much smaller antenna by using information from successive pulses to reconstruct an image of the scene. This process, which may be viewed in analogy with either pulse compression or holographic techniques, results in an along-track resolution which theoretically approaches one half of the physical antenna

length [Brown, 1967]. As will be shown in the following sections, the fact that a given object is illuminated by a large number of successive pulses rather than a single pulse also allows information on the velocity of the scatterers to be extracted from the SAR data.

The process by which the SAR data is recorded and processed may be carried out using either digital or optical (analog) techniques. Optical processing techniques are attractive because of the high density of the storage medium (film) and high processing rates. The advantages of digital processing are the greater dynamic range and fidelity of the storage medium and the fact that the processing can be more tightly controlled to avoid noise and nonlinearities.

A schematic diagram of a typical optical processor is shown in Figure 1. A photographic record of the raw data received by the SAR is placed at the signal plane (P_1) and illuminated with a coherent light source. As recorded on film, the signal history for a point object forms a Fresnel zone plate which focuses the light on a point in the image plane (P_2). The purpose of the optical elements between the signal plane and the image plane is to bring the light from all parts of the signal film into focus at a common plane [Kozma, et al., 1972; Cindrich, et al., 1977]. The light intensity distribution at the primary frequency plane (P_1') is essentially the Fourier transform of the signal plane. Thus, by placing a filter or aperture in this plane, as discussed in Section 4, a portion of each Doppler history can, in effect, be selected for processing.

For the purpose of generating an image of the scene, a photographic film is normally placed at the image plane. However, for the measurements described in Section 3, the film is replaced by an aperture which defines the sub-area of the scene selected for Doppler analysis. Light falling on this aperture is passed through another spherical lens (f_5) to the secondary frequency plane (P_2') where its intensity distribution is measured and recorded.

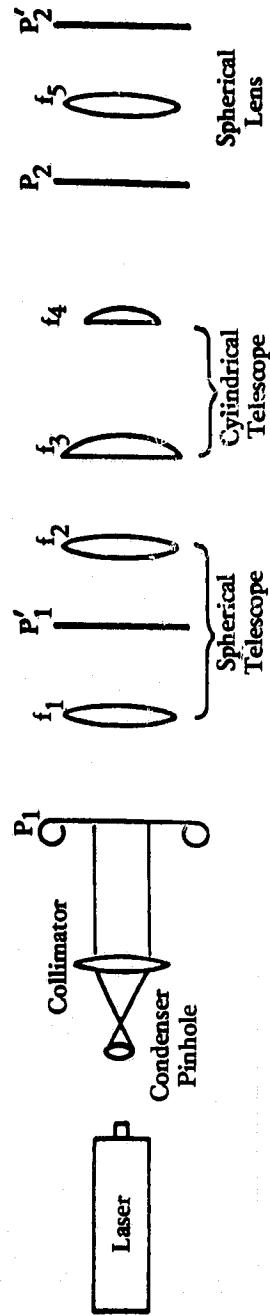


FIGURE 1. SIMPLIFIED SCHEMATIC DIAGRAM OF A SAR OPTICAL PROCESSING SYSTEM.

As will be shown in Section 3, the distribution of the light intensity at P_2' in the along-track direction contains information on the radial (i.e., line-of-sight) velocity of the scatterers within the image-plane aperture. The shape of this distribution is determined primarily by the antenna gain pattern, and the distribution is shifted by an amount proportional to the radial velocity of the scatterers. Thus, if the amount of this shift can be measured, the velocity of the scatterers can be inferred.

CURRENT AND ORBITAL VELOCITY MEASUREMENTS

The sensing of surface currents using conventional SAR data is potentially feasible using one of three techniques. One possible technique is to use the azimuthal displacement in the SAR image of an object which has a velocity component in the range direction [Raney, 1971]. The use of this phenomenon for measuring ocean currents was proposed by Shuchman, et al. [1979] although no data was presented. Measurements of the current in the Columbia River (Oregon) was reported by Shemdin, et al. [1980] using this technique with Seasat data. By measuring the azimuthal shift in the apparent boundary of the current as it flowed past the jetties, the radial line-of-sight velocity (V_r) of the Columbia River was successfully estimated. This method may be feasible where sharp current boundaries exist, but is probably not useful in the open ocean where current boundaries are more diffuse.

A second technique to measure currents from SAR data is summarized by Hayes and Shuchman [1981]*, who showed it is possible to calculate the magnitude and direction of the Gulf Stream by observing gravity wave refraction across the Stream. This method appears to be feasible in deep-water areas where a suitable gravity wave field exists, but fails where such a wave field does not exist or where wave interactions occur with the bottom.

The third technique to measure currents reported by Shuchman, et al. [1979]* and Gonzalez, et al. [1981]*, and the subject of this report, utilizes a measurement of motion-induced Doppler perturbations in the SAR signal history. As described in the following section, this technique requires that the radial (line-of-sight)

*These articles supported by this NOAA contract are found in the appendices to this report.

component of the current be large enough to produce a measurable shift in the Doppler spectrum of the SAR signals. A similar method may be used to infer the orbital velocities of gravity waves by measuring the broadening of the Doppler spectrum.

Data from both aircraft and satellite (i.e., Seasat) systems has been analyzed using Doppler techniques. These data sets are described in Section 3.2, and the results of the analyses are presented in Sections 3.3 and 3.4. Finally, sources of error in these measurements are discussed in Section 3.5.

3.1 THEORY OF DOPPLER ANALYSIS METHODS

The theoretical basis for the Doppler measurement techniques can be understood by considering the simple case of an isolated point reflector. The geometry of this situation is illustrated in Figure 2. The object is assumed to enter the antenna illumination pattern at a time $t = -T/2$ and is broadside to the SAR platform at $t = 0$. The slant range from the antenna to the object is given, to second order in t , by

$$R(t) \approx R_0 - V_r t + \frac{1}{2} \left[(V - V_a)^2 / R_0 - a_r \right] t^2 \quad (1)$$

where R_0 is the range at $t = 0$, V is the platform velocity, V_r is the radial velocity of the object, V_a is the along-track velocity of the object, and a_r is the radial acceleration of the object. The effects of V_a and a_r are neglected in the following discussion, leading to the further simplification

$$R(t) \approx R_0 - V_r t + \frac{V^2 t^2}{2R_0} \quad (2)$$

Note that the variation in $R(t)$ over the imaging time T is small compared with the swath width but is large compared to the radar wavelength. The SAR transmits a series of pulses at time intervals

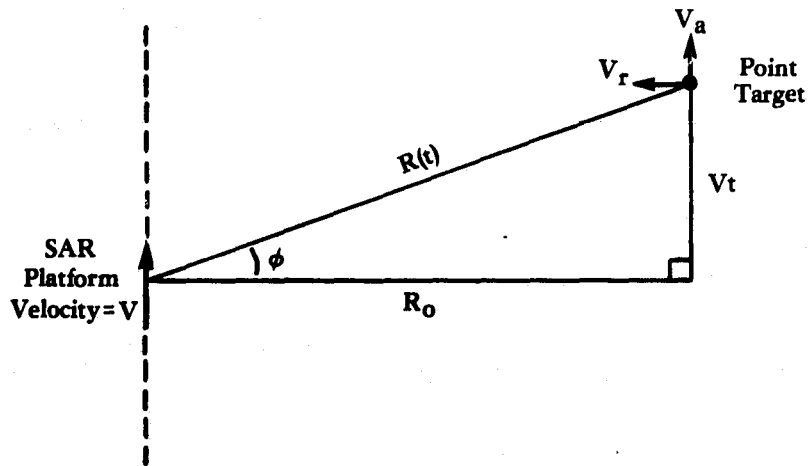


FIGURE 2. SAR VIEWING GEOMETRY FOR A POINT TARGET.

$t = n\Delta t$, receives the reflected pulses, and compares the phase of the received signals with a reference signal of the same frequency. The resulting signal for a point object of unit cross section can be expressed as

$$S_1(t) = A\left(\frac{Vt}{R_0}\right) \exp [j2kR(t)] \quad (3)$$

where $k = 2\pi/\lambda$ is the radar wavenumber and $A(\phi)$ is proportional to the antenna gain pattern in the along-track direction. In the case of optical recording, the real part of this signal is recorded on film at the position (x', y') where x' corresponds to the time t and y' corresponds to the across-track coordinate.

The digital or optical processing of the SAR signal in order to reconstruct an image of the scene may be described in the ideal case as a convolution of this signal with the function

$$q(t) = e^{-jbt^2} \quad (4)$$

where b is normally chosen as $b = kV^2/R_0$ to cancel out the quadratic phase factor in $S_1(t)$. In the case of optical processing, this operation is carried out by simply illuminating the signal film with coherent light and measuring the light intensity at an appropriate distance from the signal film [Kozma, et al., 1972; Cindrich, et al., 1977]. The illumination is assumed for the present to be uniform and the illuminated area is assumed to be much longer than the signal history length. The effects of variations in the illumination and of finite aperture widths are considered in Section 3.5. The processed signal (corresponding to the distribution of the light amplitude in the along-track direction at the image plane of the optical processor) is then given by

$$\begin{aligned}
 S_2(t) &= \int_{-\infty}^{\infty} S_1(t') q(t' - t) dt' \\
 &= e^{-jbt^2} \int_{-\infty}^{\infty} A\left(\frac{vt'}{R_0}\right) e^{j2(bt - kv_r)t'} dt' \\
 &= c e^{-jbt^2} \tilde{A}[2k(vt - \Delta X)]
 \end{aligned} \tag{5}$$

where \tilde{A} denotes the Fourier transform of A , c is a complex constant, and

$$\Delta X = R_0 \frac{v_r}{v} \tag{6}$$

Thus, the image of the point object is essentially the Fourier transform of the antenna pattern displaced by a distance ΔX which is proportional to the radial velocity of the object. This displacement could be used to infer the radial velocity of the object if the proper location of the object were known. However, in most cases, this method is not feasible for mapping ocean currents since the current boundaries are not sufficiently sharp and are accompanied by surface roughness changes which tend to obscure any image displacement. A more promising approach is to consider the Fourier transform of the output signal

$$\tilde{S}_2(\omega) = \int_{-\infty}^{\infty} S_2(t) e^{j\omega t} dt . \tag{7}$$

Using the above expression for $S_2(t)$, it can be shown that

$$|\tilde{S}_2(\omega)|^2 = c' |\tilde{F}(\omega - 2kv_r)|^2 \tag{8}$$

where $F(\omega)$ is the Fourier transform of the function

$$f(t) = A\left(\frac{vt}{R_0}\right) e^{jbt^2} . \tag{9}$$

In the optical processor, $|S_2(\omega)|^2$ corresponds to the light intensity in the secondary frequency plane (P_2'), with the ω axis lying parallel to the longitudinal axis of the film (i.e., the along-track direction). Thus, the spectrum observed in the frequency plane is shifted by an amount $2kV_r$ rad/sec, or $2V_r/\lambda$ Hz, for an object having a radial velocity V_r . If this spectrum shift is an appreciable fraction of the spectrum width, it can, in principle, be detected and used to infer the radial velocity V_r .

The shape of the spectrum is determined primarily by the antenna gain pattern in the along-track direction. If the antenna is a uniformly illuminated linear aperture of length D , the one-way (intensity) gain pattern is given [Brown, 1967] by

$$g(\phi) = \left(\frac{\beta}{\pi\phi}\right)^2 \sin^2\left(\frac{\pi\phi}{\beta}\right) \quad (10)$$

where $\beta = \lambda/D$ is the antenna beamwidth (the 4 dB points are at $\phi = \pm\beta/2$). If this function is approximated by a Gaussian

$$g(\phi) = e^{-\frac{4\phi^2}{\beta^2}} \quad (11)$$

the spectrum has the form

$$|\tilde{F}(\omega)| = c e^{-4\omega^2/\beta'^2} \quad (12)$$

i.e., the spectrum also has a Gaussian form with an equivalent width

$$\beta' = 2 \left[\left(\frac{4V}{R_0\beta}\right)^2 + (kV\beta)^2 \right]^{1/2} \approx 2kV\beta \quad (13)$$

at the 4 dB points.

The current detectability criterion using a Gaussian antenna pattern can be stated as

$$\frac{\text{frequency shift}}{\text{spectrum width}} = \frac{V_r}{\beta v} > \alpha \quad (14)$$

where α is a threshold whose value is determined by the system performance and the size of the sample used for measuring the spectrum (both of which influence the amount of "noise" in the spectrum measurement). The data presented in the following sections indicate that values of $\alpha \sim 0.1$ are achievable for areas on the order of 10^4 resolution elements using optical methods. Preliminary experience with all-digital processing suggests that at least an order of magnitude improvement in the detectability threshold can be obtained with digital methods.

The foregoing discussion has assumed that all the scatterers within the test area are moving with a constant velocity, as in the case of a uniform surface current. When the test area contains surface elements moving at different velocities, the resulting spectrum may be described as a convolution of the uniform-velocity spectrum with the velocity distribution function for the surface. This would be the case, for example, when the test area contains a gravity wave field, because of the orbital motions associated with these waves. If the radar cross section were constant over the entire wave surface, the orbital velocity would cause a symmetrical broadening of the spectrum. In fact, however, the radar cross section is modulated by variations in both the slope and the surface roughness along the wave profile. Describing this effect by the modulation index m [Keller and Wright, 1975], the radar cross section at a given point on a wave of frequency Ω may be written as

$$\sigma(x, y, t) = \sigma_0 [1 + m \cos (Kx \cos \theta_w + Ky \sin \theta_w - \Omega t + \phi)] \quad (15)$$

where σ_0 is the average cross section, $K = \Omega^2/g$ is the water wave number, θ_w is the wave propagation direction relative to the x-axis, and ϕ is the phase angle by which the maximum cross section leads the wave crest. The orbital velocity at this point on the wave surface is (to first order in the wave amplitude)

$$V_x(x, y, t) = a \cos \theta_w \cos (Kx \cos \theta_w + Ky \sin \theta_w - \Omega t) \quad (16)$$

in the cross-track direction, and

$$V_z(x, y, t) = a \sin (Kx \cos \theta_w + Ky \sin \theta_w - \Omega t) \quad (17)$$

in the vertical direction. Thus, the radial component of the orbital velocity for an incidence angle θ_i is

$$V_r(x, y, t) = V_x \sin \theta_i + V_z \cos \theta_i \quad (18)$$

The wave-broadened Doppler spectrum can be obtained by integrating over one complete wave cycle, either in time or space. Integrating over time, we obtain

$$|\tilde{S}_2(\omega)| = \frac{\Omega}{2\pi} \int_0^{2\pi/\Omega} \tilde{F}[\omega - 2kV_r(t)]\sigma(t) dt \quad (19)$$

where the position dependence has been deleted from V_r and σ , since it is cancelled out by the integration process. For a Gaussian antenna pattern, the spectrum may be written as

$$\tilde{S}_2(\omega) = \frac{\sigma_0 \Omega}{2\pi} \int_0^{2\pi/\Omega} \exp \left\{ -4 \left[\frac{\omega}{\beta'} - \frac{2k}{\beta'} V_r(t) \right]^2 \right\} [1 + m \cos (\Omega t + \phi)] dt \quad (20)$$

This spectrum is plotted in Figure 3 for three values of $2k\Omega a/\beta'$ with $\theta_w = \theta_i = 45^\circ$, $m = 0.5$, and $\phi = 45^\circ$. Note that a significant broadening is evident for the case $2k\Omega a/\beta' = 0.5$. The only effect of the modulation (m) appears to be a slight asymmetry and shifting of the spectrum.

As in the case of Doppler shifting, the measurable increase in the Doppler bandwidth due to wave orbital motions depends on the system performance and the sample size. Using $\beta' = 2k\beta V$, we may define the minimum measurable wave amplitude as that which satisfies

$$\frac{\Omega a}{\beta V} > \alpha' \quad (21)$$

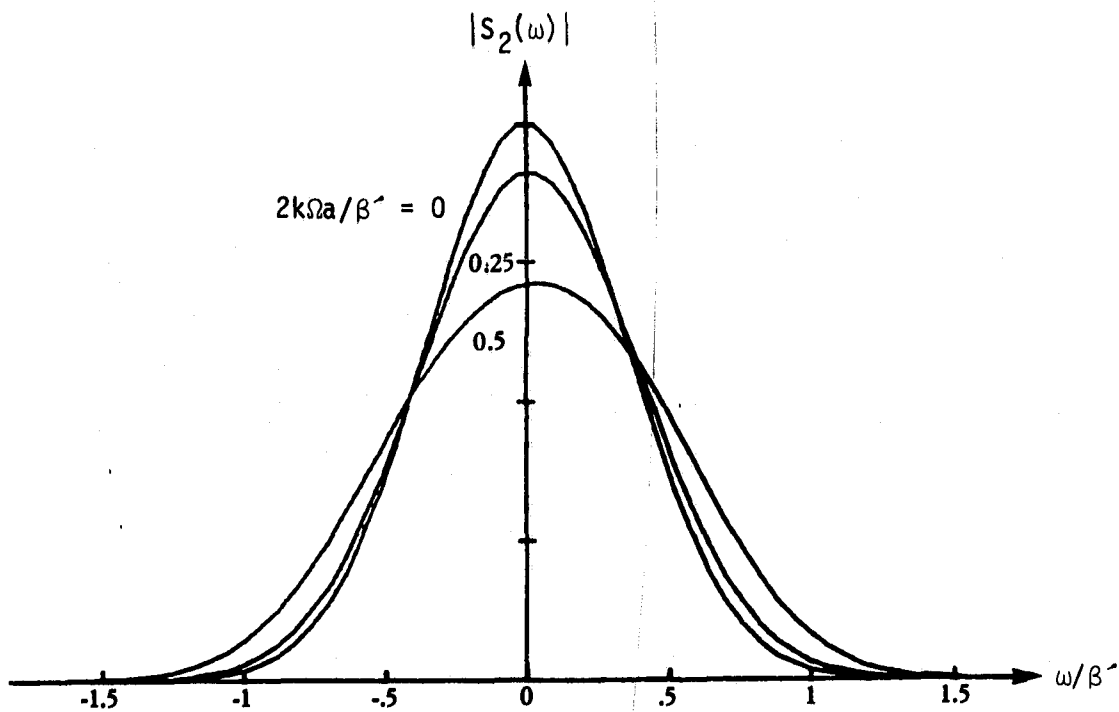


FIGURE 3. EXAMPLE OF DOPPLER SPECTRUM BROADENING DUE TO WAVE ORBITAL VELOCITY, FOR THREE VALUES OF THE SCALED WAVE AMPLITUDE

$$2k\Omega a/\beta' \approx \frac{\Omega a}{\beta v}$$

(Frequency axis is scaled by the stationary-surface Doppler bandwidth β' .)

where α' is a broadening threshold whose value is on the order of 0.5. Examples of wave-broadened Doppler spectra are given in Section 3.3 below.

3.2 DATA SET DESCRIPTION

Doppler measurements were made on the aircraft and Seasat data sets listed in Tables 1 and 2. These data sets are described briefly in this section, and the measurements themselves are discussed in the following section.

The first four data sets listed in Table 1 were collected with the ERIM X-L band SAR system mounted in a C-46 aircraft platform. The first three data sets include an area just off the coast of Florida, while the fourth covers an area further offshore which includes the western boundary of the Gulf Stream. Surface conditions for the first three data sets are characterized by a dominant wavelength of 80 m with a significant wave height of 1.56 m, and an onshore current of 85 cm/sec. The direction of propagation of the 80 m waves was also in the westerly or onshore direction. The Gulf Stream current velocity distribution on 15 December was such that the difference in current velocity for the two areas selected from pass 13 was on the order of 0.5 m/sec.

The remaining data sets listed in Table 1 were collected with the same radar system mounted in a Convair 580 aircraft. These data sets include two inlets into the Straits of Georgia east of Vancouver Island, British Columbia. The 27 July pass was collected during flood tide, at which time a current of approximately 2 m/sec was flowing into the Straits of Georgia. At the time of the 28 July overpass, the current was in the opposite direction at about 1 m/sec. The sea state was fairly calm in these areas on both days, with no visible gravity waves present in the radar imagery.

The Seasat data sets considered in this study are listed in Table 2. The Columbia River pass was collected at ebb tide, with a

TABLE 1
SUMMARY OF AIRCRAFT DATA SETS SELECTED FOR DOPPLER ANALYSIS

<u>Area</u>	<u>Date</u>	<u>Pass</u>	<u>Band</u>	<u>Look Direction</u>	<u>Incidence Angle</u>	<u>Aircraft Speed (m/sec)</u>	<u>Film Speed (mm/sec)</u>
Marineland	14 Dec 75	1	X, L	160°	60°	78	5.83, 2.13
Marineland	14 Dec 75	3	X	70°	60°	86	6.42
Marineland	14 Dec 75	7	X, L	250°	60°	82	5.99, 2.23
Gulf Stream	15 Dec 75	13	X	340°	45°	77	5.63
Porlier Pass	27 Jul 78	6	X, L	226°	35°	148	10.0, 3.63
Active Pass	28 Jul 78	10	X	298°	48°	138	9.40
Active Pass	28 Jul 78	11	X	298°	53°	139	9.40
Active Pass	28 Jul 78	12	X	47°	54°	134	9.07

TABLE 2
SUMMARY OF SEASAT DATA SETS SELECTED FOR DOPPLER ANALYSIS

<u>Area</u>	<u>Date</u>	<u>Orbit</u>	<u>Look Direction</u>
Columbia River	7 July 1978	150	66°
Dover Straits	19 August 1978	762	63°
Gulf Stream	11 August 1978	651	63°
Straits of Juan de Fuca	13 August 1978	681	63°

current of 2.5–3.0 m/sec flowing out of the river. The SDR data for this pass shows an unusually large yaw angle of approximately 3.5 degrees. The current in the English Channel (Dover Straits) at the time of the 19 August overpass was estimated to be 0.5 to 2.0 m/sec at 210° N, based on tide tables for this area.

The Gulf Stream current on 11 August 1978 is not precisely known, but the USCG Weekly Sea Current chart for 30 August 1978 indicates a maximum current of about 2 m/sec in an approximately northward direction for the area covered by Orbit 651. Striations on the Seasat imagery indicate that the Gulf Stream appears to be flowing in a somewhat more easterly direction, at an angle of about 45° to the range direction.

For the Straits of Juan de Fuca, tide tables indicate a current of approximately 0.5 m/sec into the Straits.

The incidence angle for all of the Seasat data is approximately 20° , so that the radial component of the current is about one third of the horizontal current in the cross-track direction.

3.3 CURRENT MEASUREMENTS

Measurements of the Doppler spectrum for selected sub-areas of each data set were made on the ERIM optical processor described in Section 2. Sub-areas were selected for each data set by placing a rectangular aperture in the image plane of the processor, and the distribution of the light intensity in the along-track direction of the frequency plane was measured and recorded. The aperture size was equivalent to a 1 km x 1 km area for the 1975 aircraft data sets. For the 1978 aircraft data sets, the aperture size was 250 meters in azimuth by 500 meters in range. For the Seasat data, the aperture size was typically 3 km x 3 km.

The frequency scale for these plots was established by inserting a grating with a known line spacing at the signal plane and measuring

the separation of the resulting spikes in the frequency plane. This spatial frequency was then converted into a temporal frequency by multiplying by the film speed. The film speeds for the aircraft data sets are shown on Table 1. For Seasat, the film speed was 3.24 cm/sec.

The Doppler spectra for two sub-areas of the Marineland pass 1 X-band (3.2 cm) data over water and land are shown in Figure 4. Although there is a considerable difference in the width of these spectra, the relative shift between the water and land spectra is negligible. The spectrum width, defined as the difference between the 3 dB points, is the 72.8 Hz for the land spectrum and 160.8 Hz for the water spectrum. The L-band (23.8 cm) spectra for water and land are shown in Figure 5. These spectra are nearly the same in both bandwidth and mean frequency.

The X-band spectra for passes 3 and 7, which were flown at $\pm 90^\circ$ with respect to the pass 1 flight path, are shown in Figures 6 and 7. The relative shift between the water and land spectra is 45.8 Hz for pass 3, and -54.3 Hz for pass 7. Using the equation

$$\Delta f = \frac{2V_r}{\lambda} \quad (22)$$

these Doppler shifts imply radial velocities of 0.73 m/sec and -0.87 m/sec, respectively. Dividing by $\sin 60^\circ$, one obtains a horizontal current of 0.85 m/sec for pass 3 and 1.00 m/sec for pass 7. The direction of this current is indicated by the sign of the Doppler shifts for passes 3 and 7, and by the absence of any shift for pass 1, to be in the westerly direction.

The L-band spectra for pass 7 (Figure 8) show a negligible Doppler shift, despite the existence of an apparent radial velocity component as indicated by the X-band data. However, if one calculates the expected Doppler shift at L-band due to this velocity component, one obtains a result of 6 Hz, which is apparently too small in comparison with the bandwidth to be measurable.

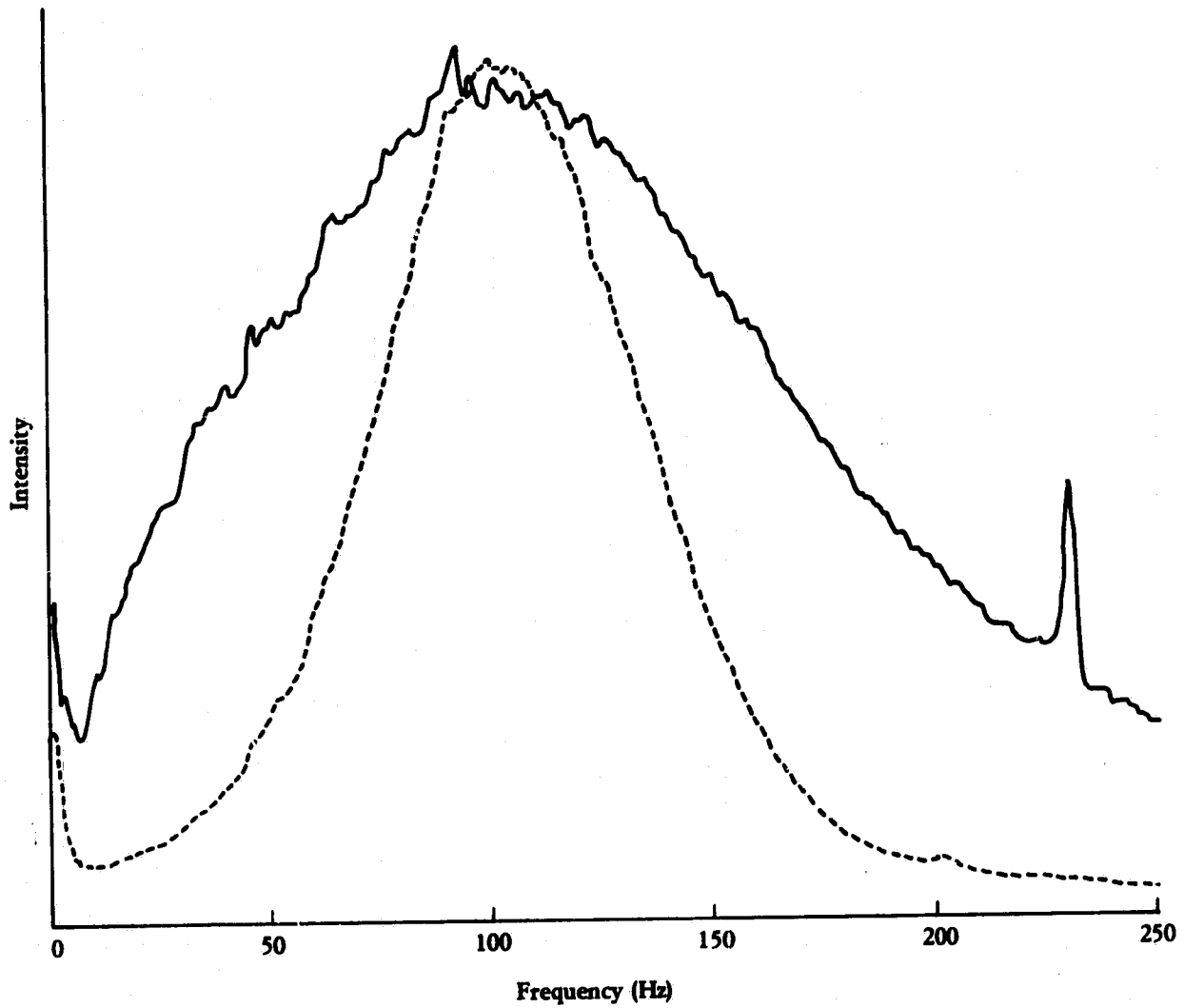


FIGURE 4. DOPPLER SPECTRA FOR MARINELAND (PASS 1) X-BAND DATA.
(Dashed line indicates land spectrum.)

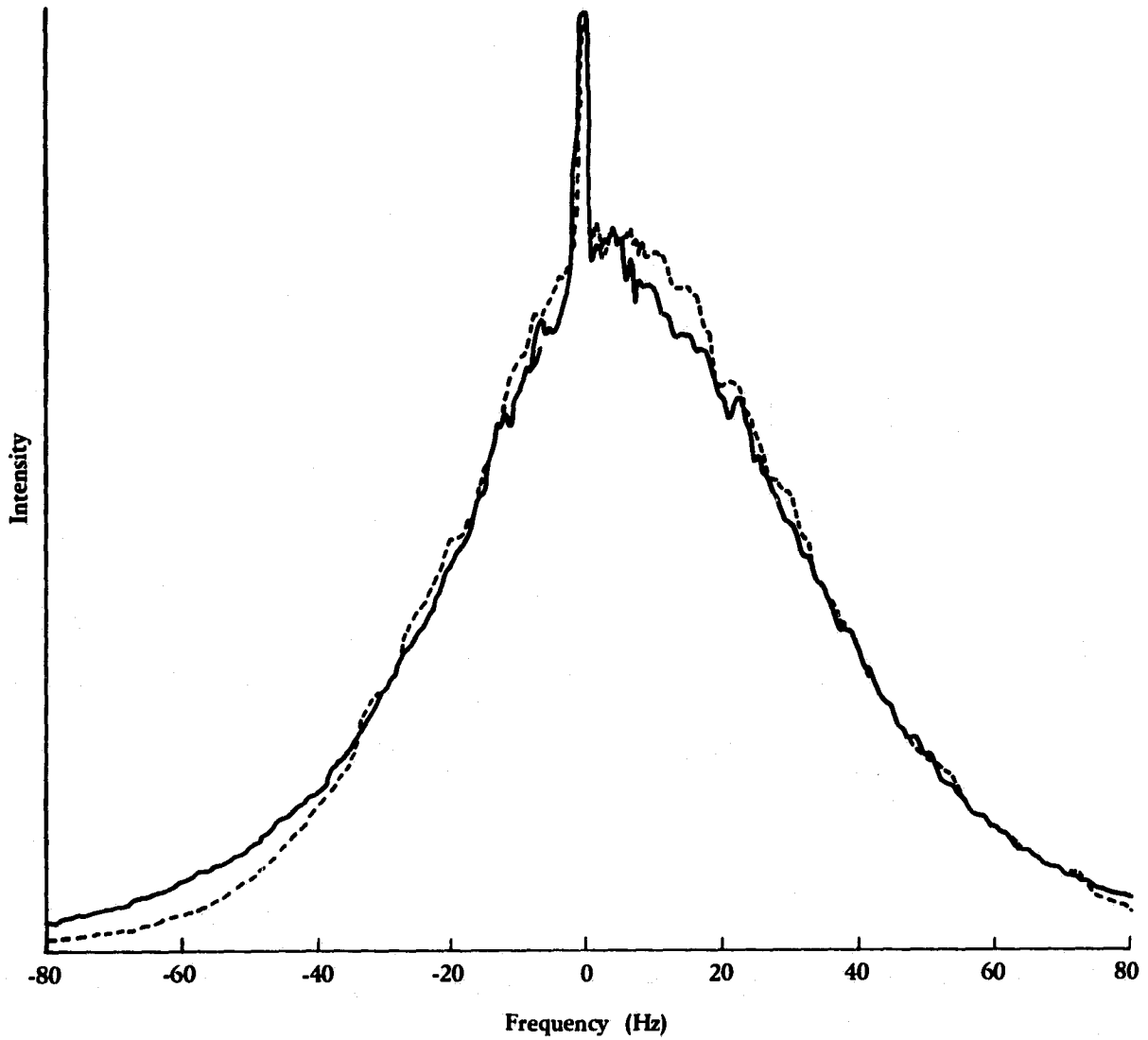


FIGURE 5. DOPPLER SPECTRA FOR MARINELAND (PASS 1) L-BAND DATA.
(Dashed line indicates land spectrum.)

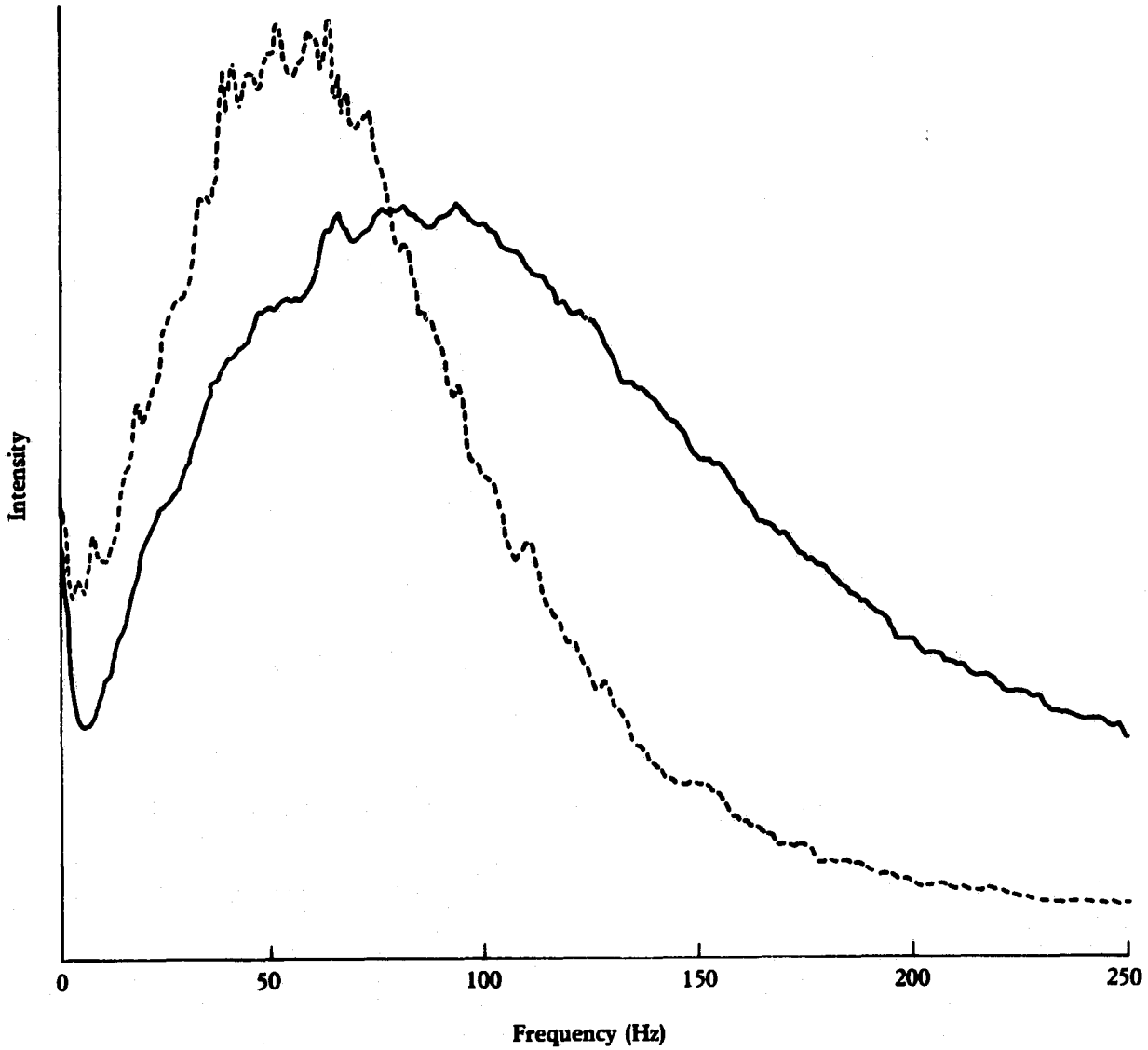


FIGURE 6. DOPPLER SPECTRA FOR MARINELAND (PASS 3) X-BAND DATA.
(Dashed line indicates land spectrum.)

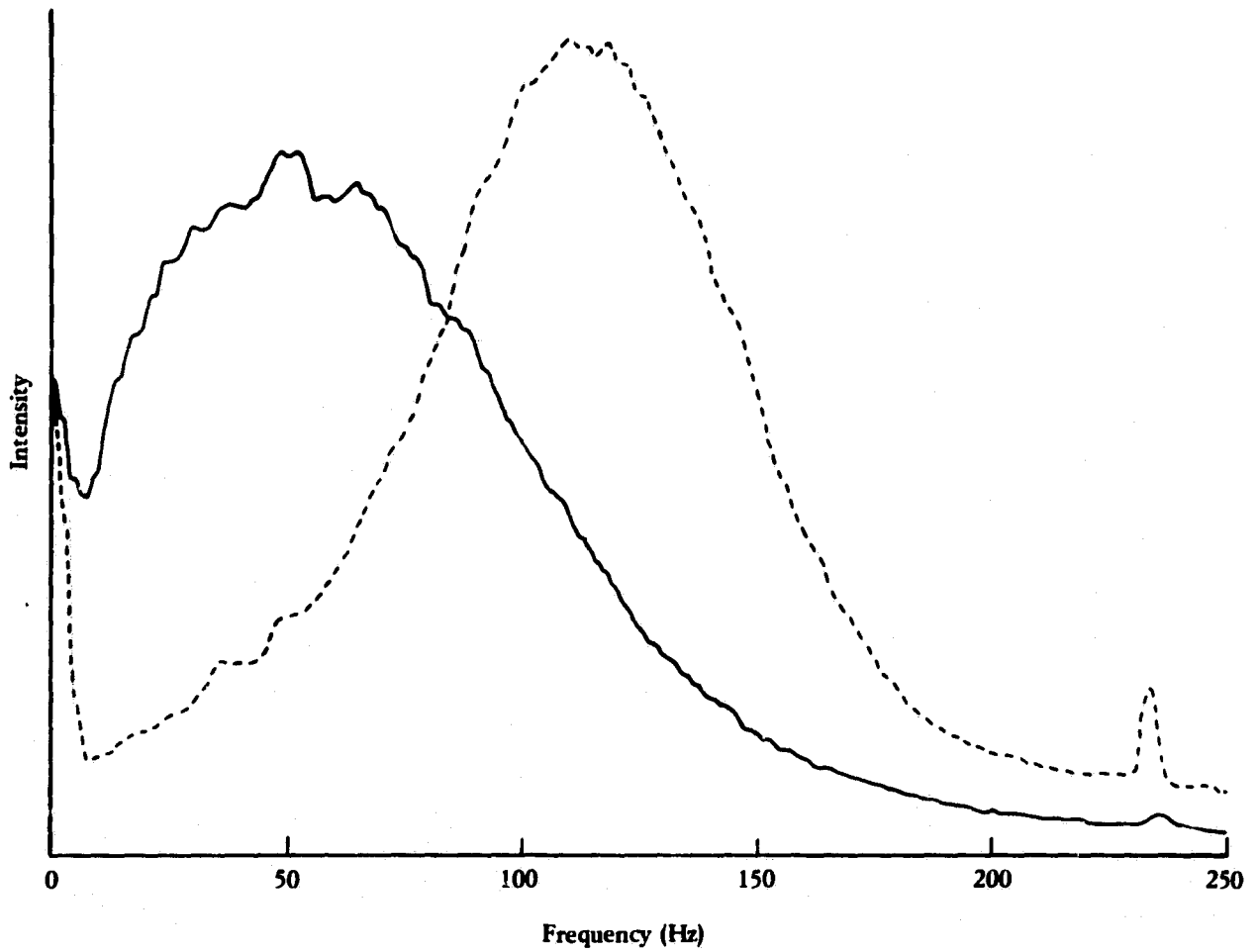


FIGURE 7. DOPPLER SPECTRA FOR MARINELAND (PASS 7) X-BAND DATA.
(Dashed line indicates land spectrum.)

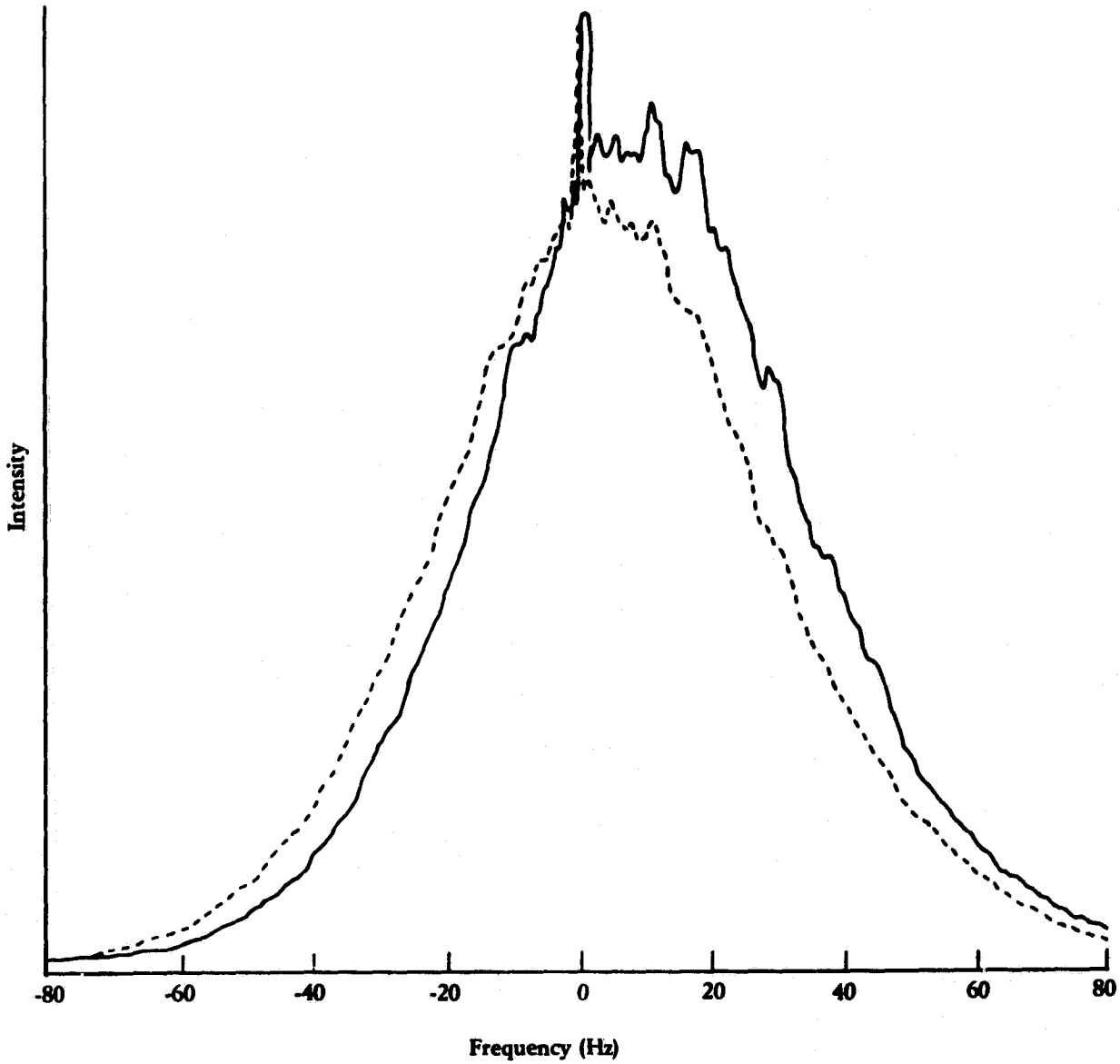


FIGURE 8. DOPPLER SPECTRA FOR MARINELAND (PASS 7) L-BAND DATA.
(Dashed line indicates land spectrum.)

Doppler spectra for two sub-areas of the Gulf Stream data set are shown in Figure 9. These two sub-areas are spaced approximately 3.1 km apart, and are on opposite sides of an apparent current boundary in the image. The relative shift between these spectra is 23.4 Hz, which indicates a difference in radial velocity of 0.37 m/sec or a horizontal current of 0.53 m/sec toward the north for the second sub-area inside the current boundary. This result is consistent with the known direction of the Gulf Stream and with surface observations of the current gradient at this location.

Figure 10 shows two Doppler scans for the Porlier Pass data sets, one from a sub-area within the channel itself and one from an adjacent land area. The spectrum width for this data is larger than that for the 1975 data sets because of the higher aircraft speed of the Convair 580 as compared with the C-46. This increase in the bandwidth, along with the lower signal levels due to the smaller size of the sub-areas, causes a noticeable asymmetry in the recorded spectra. This effect was modeled as an additive noise component which varies linearly with frequency. A straight line was drawn between the high-frequency asymptote and the zero-frequency background, and points along this line were graphically subtracted from the plotted curves. The half-power points were then located on the "corrected" curves and used to calculate the bandwidths and mean frequencies of the spectra. The Doppler shift of 36.4 Hz between the land and water spectra in Figure 10 implies a radial velocity of 0.58 m/sec in the flood direction (i.e., into the Straits of Georgia). Assuming this current to be at an angle of 45° to the cross-track direction, the calculated current speed is 1.43 m/sec. This is smaller than the maximum reported current of about 2 m/sec, possibly because it represents an average value over an area containing currents lower than the maximum.

The Doppler scans for the three Active Pass data sets on 28 July 1978 are shown in Figures 11-13. Passes 10 and 11 are at the same

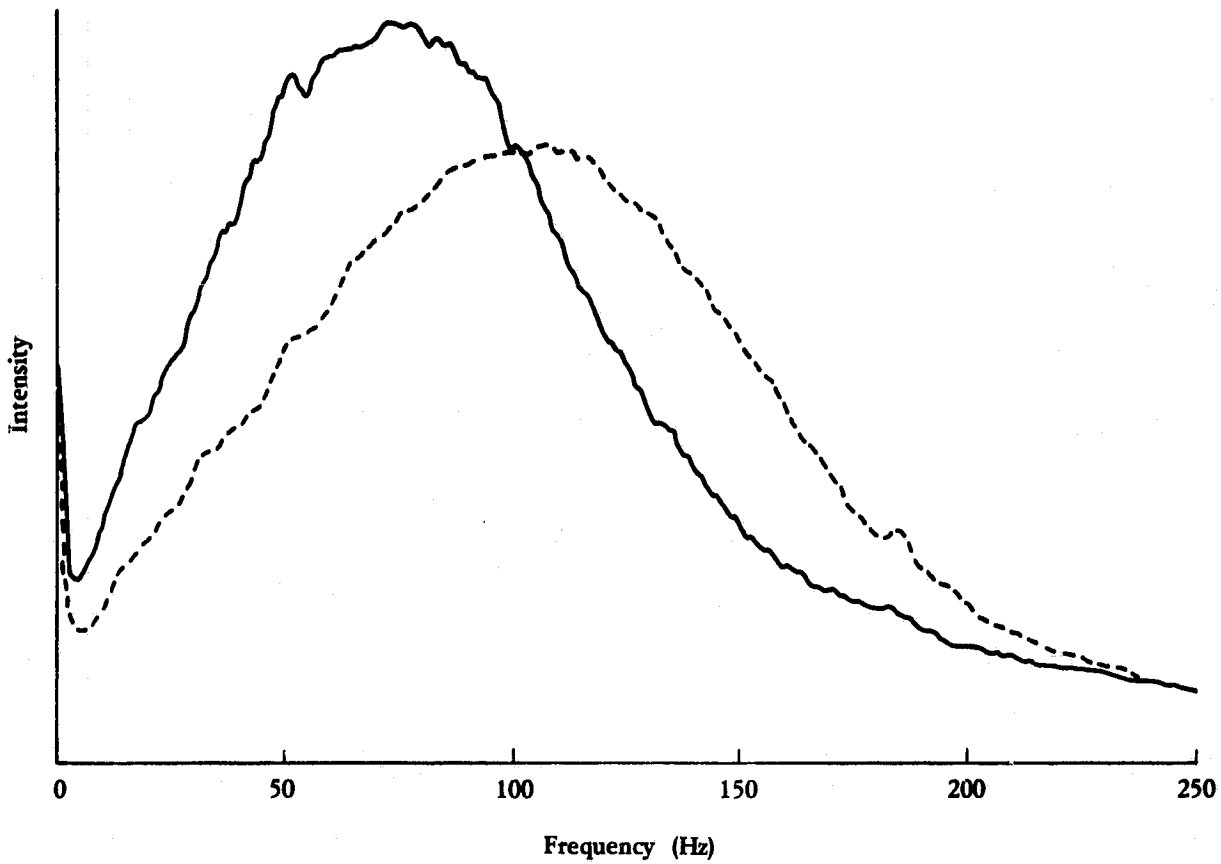


FIGURE 9. DOPPLER SPECTRA FOR GULF STREAM (PASS 13) X-BAND DATA.
(Dashed line indicates stationary water spectrum.)

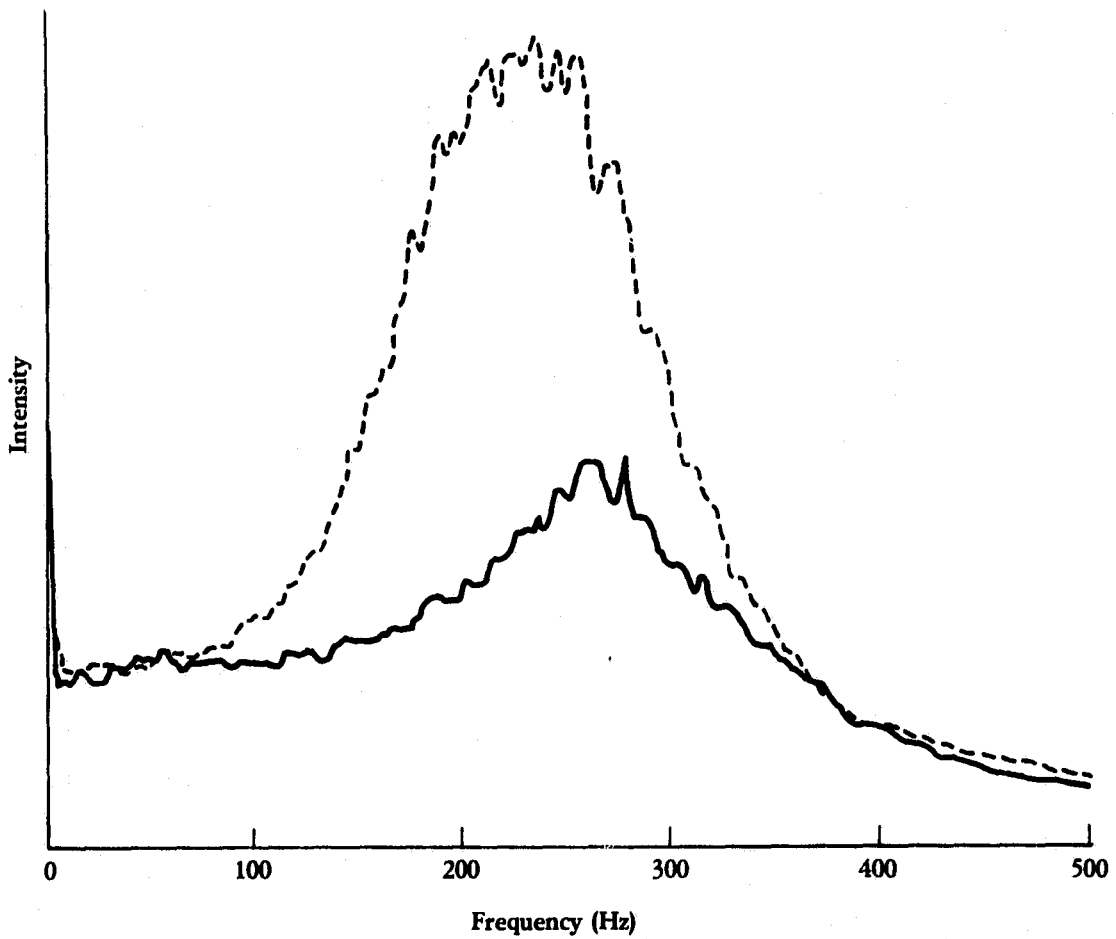


FIGURE 10. DOPPLER SPECTRA FOR PORLIER PASS (PASS 6) X-BAND DATA.
 (Dashed line indicates land spectrum.)

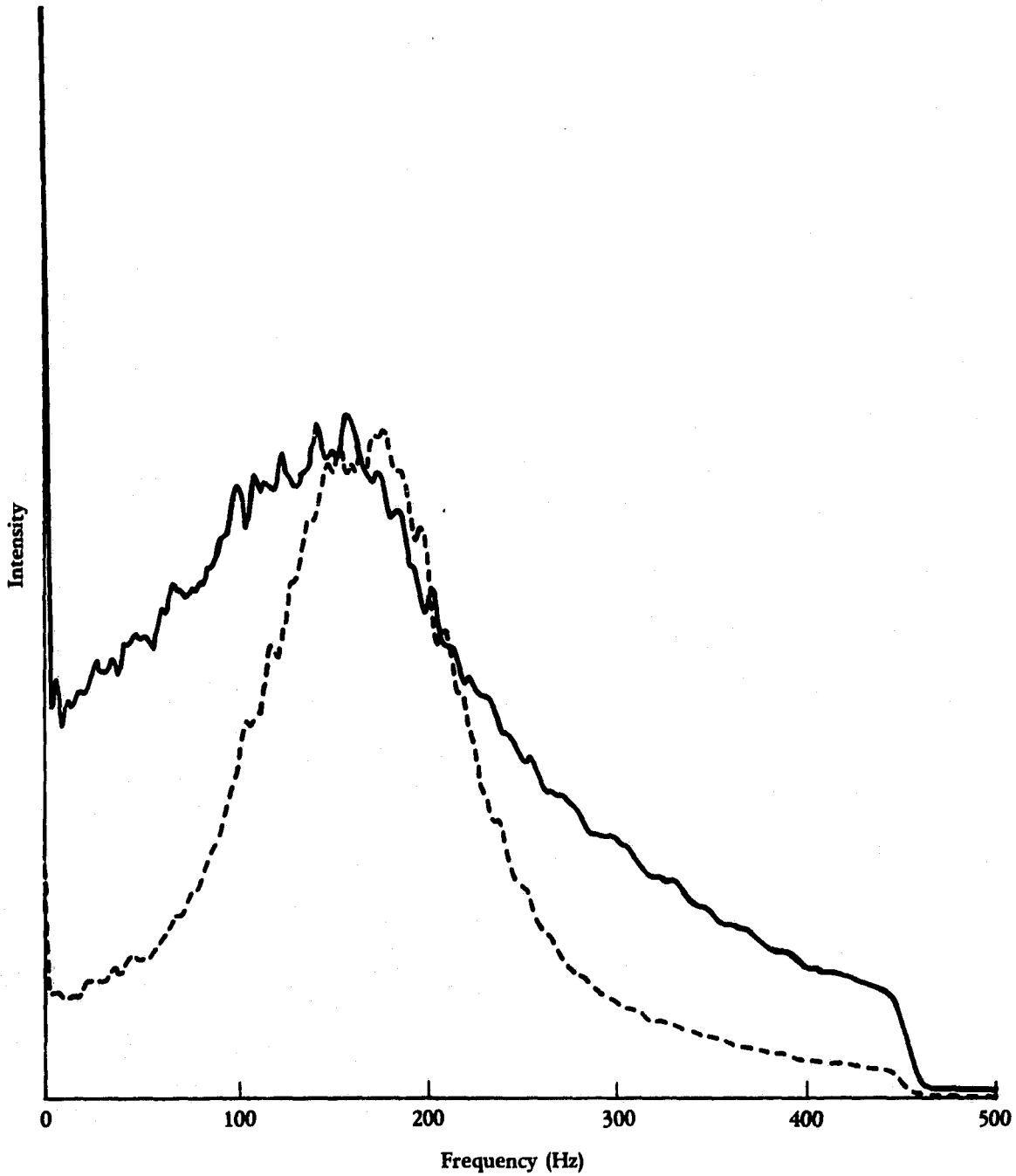


FIGURE 11. DOPPLER SPECTRA FOR ACTIVE PASS (PASS 10) X-BAND DATA.
 (Dashed line indicates land spectrum.)

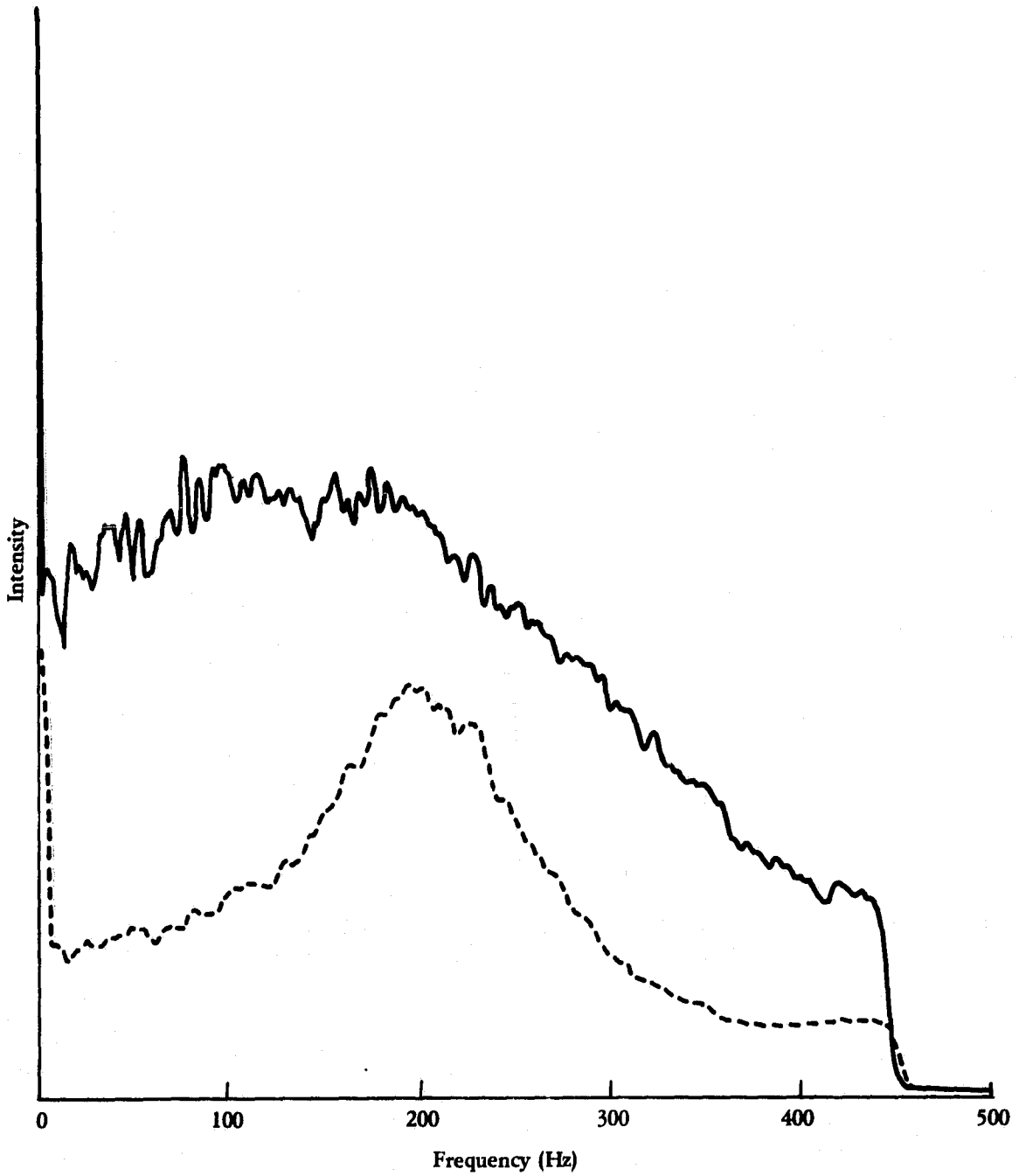


FIGURE 12. DOPPLER SPECTRA FOR ACTIVE PASS (PASS 11) X-BAND DATA.
 (Dashed line indicates land spectrum.)

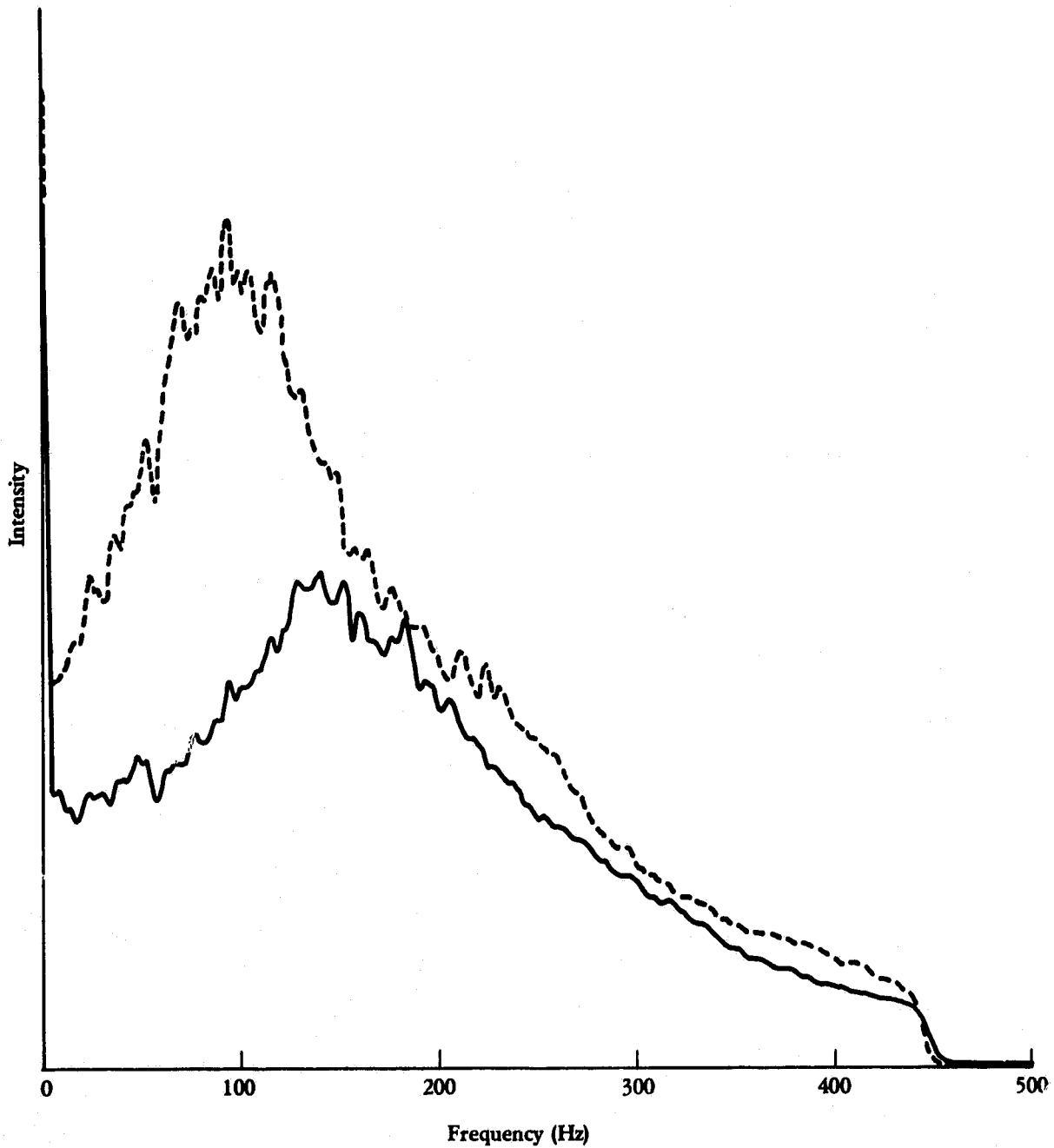


FIGURE 13. DOPPLER SPECTRA FOR ACTIVE PASS (PASS 12) X-BAND DATA.
(Dashed line indicates land spectrum.)

orientation, and show Doppler shifts in the same direction of -21.4 Hz and -18.8 Hz, respectively, for the water spectra relative to the land. These shifts indicate horizontal currents of 0.46 m/sec and 0.38 m/sec in the cross-track direction out of the Straits of Georgia. Pass 12 was flown at a different orientation and shows a positive Doppler shift of 47.1 Hz, which implies a horizontal current of 0.93 m/sec in the same direction. The direction of the current indicated by all three passes is consistent with surface observations, although the magnitude of the current calculated from passes 10 and 11 is somewhat too small.

The system effects which cause the asymmetry in these Doppler scans represent a potentially large source of error in the current measurement, particularly for the higher-bandwidth data. For Seasat data, which has a bandwidth on the order of 1 kHz, the potential error could be expected to be quite large. In order to address this problem, a set of procedures was developed for making corrections for system effects.

The starting point for this set of procedures was the development of a capability for digitally recording the frequency-plane measurements, so that the required manipulations of the data could be more easily carried out by computer. This capability was developed as a modification of the ERIM image dissector facility, which is normally used for digitizing the light distribution in the image plane of the optical processor. In order to scan in the azimuthal direction of the frequency plane, the Fourier transform lens was mounted on a movable platform which was translated by means of a digitally-controlled stepping motor. Scanning is also performed electronically within the image dissector tube in the range direction, but normally the range samples were averaged together.

Once this digital recording facility was developed, a sequence of measurements was made in order to determine the system parameters,

which normally vary from one data set to the next. First, the optical noise introduced by the processor itself was measured by scanning with no film in the signal plane. This set of values was subtracted point-by-point (i.e., for each frequency sample) from all of the subsequent measurements. Next, a scan was performed with a section of signal film which was recorded with no signal input. This data was used in two ways: first, it was taken as a measure of the total system noise and subtracted from the actual Doppler frequency scans for each image subset. In addition, the measurement was used to estimate the modulation transfer function (MTF) of the SAR system. It may be assumed that the noise input to the receiver is nearly frequency-independent, or at least has a bandwidth larger than the SAR system. Therefore, the frequency distribution of the output noise spectrum is directly proportional to the frequency response, or MTF, of the system. Thus, the noise spectrum was used as a normalization factor for the actual Doppler scans in order to compensate for the falloff in the system response with increasing frequency.

During the initial setup before these measurements were made, it was discovered that the azimuth telescope introduced an excessive amount of distortion into the frequency plane data. To eliminate this distortion, the azimuth telescope was removed from the optical bench. This necessitated the use of two separate image apertures, one in the range focal plane and the other in the azimuth focal plane. After the first trial run, pronounced effects due to a non-uniform illumination of the signal film were also noted, and steps were taken to broaden the illumination pattern. After this adjustment, the illumination at the edges of the 60 mm aperture was 2.2 dB down from the maximum center illumination.

The data reduction process consisted of four steps. In the first step, the data were read from tape and the range samples were averaged together to yield a single intensity reading for each azimuth sample. The resulting set of (typically 3200) samples was written

into a disc file for future access. In the second step, the file representing total system noise was subtracted from each of the data files, and the processor noise was subtracted from the MTF file. In the third step, the file representing the system MTF was smoothed and truncated at a specified fraction of the maximum value (to avoid dividing by zero or a very small number in the next step). In the last step, each data file was normalized by the system MTF and plotted. Additionally, the last step allows the option of smoothing the data and/ or calculating the "median frequency" for each data set. The "median frequency," f_c , is defined as the azimuth frequency for which the area under the spectrum from $f_c - \Delta f/2$ to f_c equals the area from f_c to $f_c + \Delta f/2$. The frequency interval Δf was generally chosen as approximately the 3 dB width of the spectrum.

As a test of this procedure, a set of Doppler scans was obtained from the 27 July 1978 Porlier Pass data set. Doppler scans were obtained for an area inside Porlier Pass at an incidence angle of 32° and for an adjacent land area. These scans were corrected for the system MTF, which was obtained from a section of the signal film which was recorded while the transmitter was turned off. The system MTF is shown in Figure 14, and the corrected Doppler spectra for land and water are shown in Figure 15. The center frequencies calculated for these spectra are 237 Hz and 278 Hz, respectively. This 41 Hz shift implies a radial velocity of 0.66 m/sec, a horizontal across-track current of 1.24 m/sec, and a total current of 1.75 m/sec if the direction is assumed to be 45° with respect to the across-track direction. This result is in somewhat better agreement with the surface observations than the result obtained earlier without the full MTF correction.

The procedure was repeated using the L-band data, resulting in the spectra shown in Figure 16. The center frequencies for these spectra indicate a small and probably not statistically significant Doppler shift of 7.2 Hz.

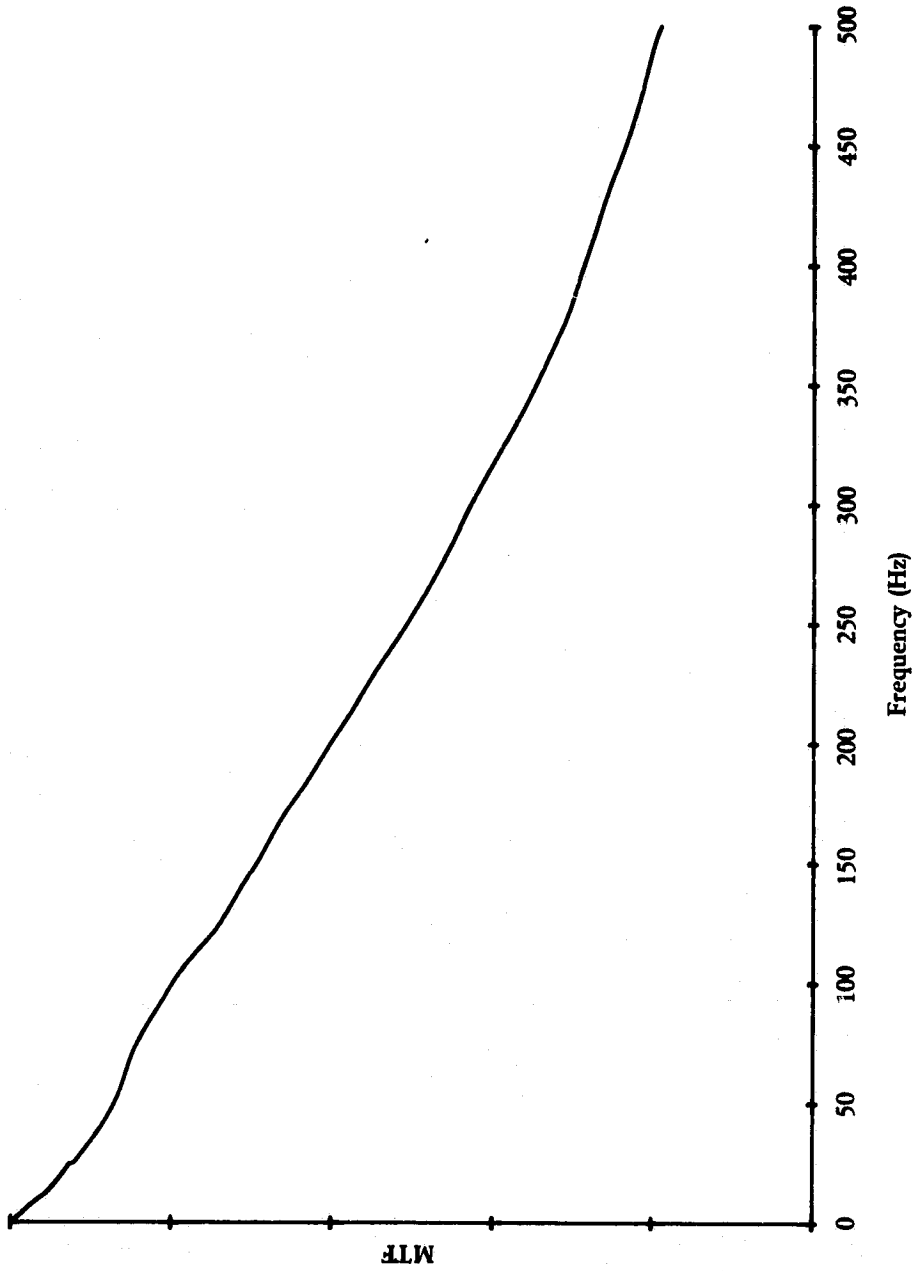


FIGURE 14. AIRCRAFT X-BAND MODULATION TRANSFER FUNCTION FOR CV-580 DATA.

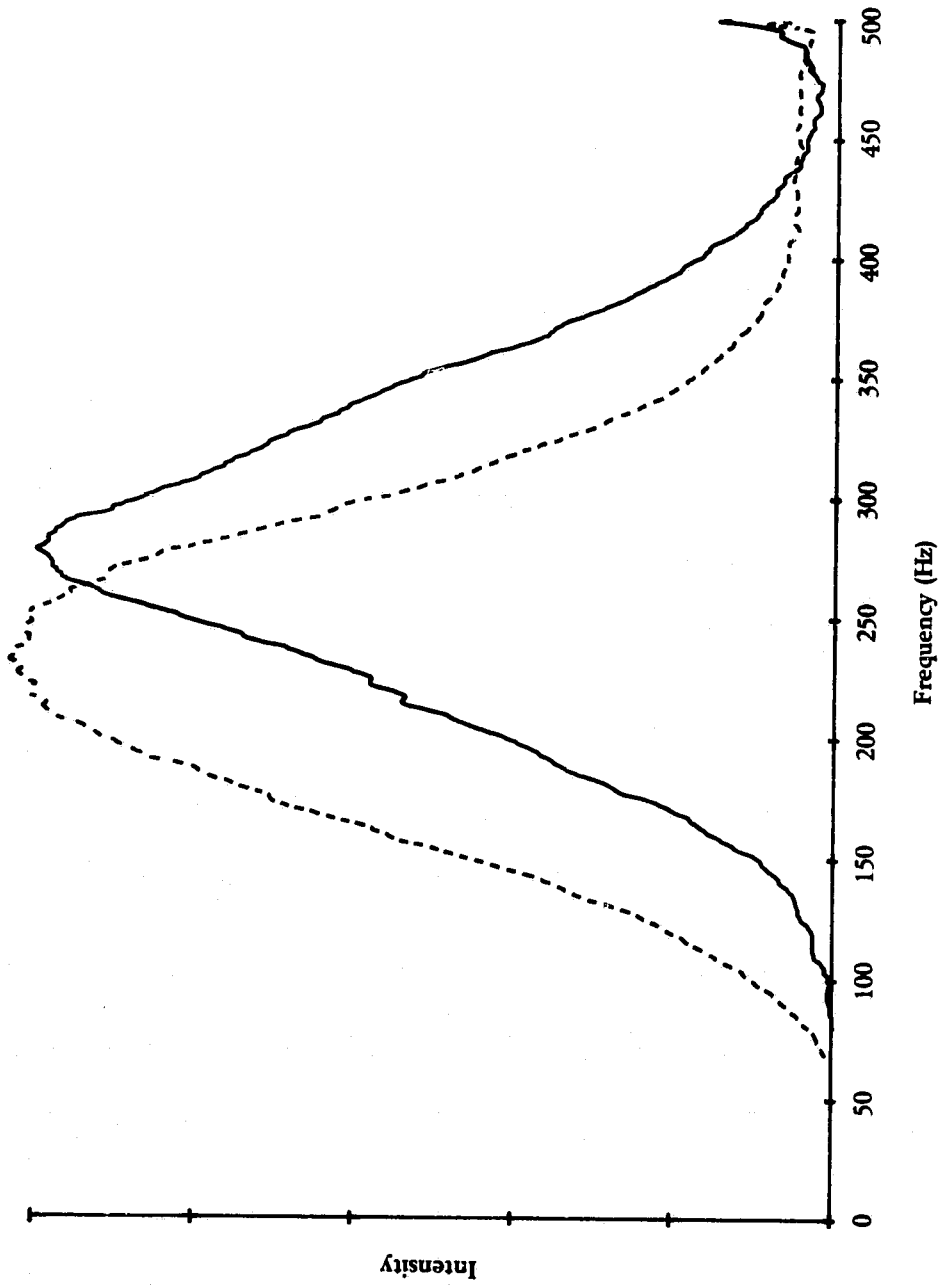


FIGURE 15. DIGITALLY RECORDED AND CORRECTED DOPPLER SPECTRA FOR PORLIER PASS X-BAND AIRCRAFT DATA.
(Dashed line indicates land spectrum.)

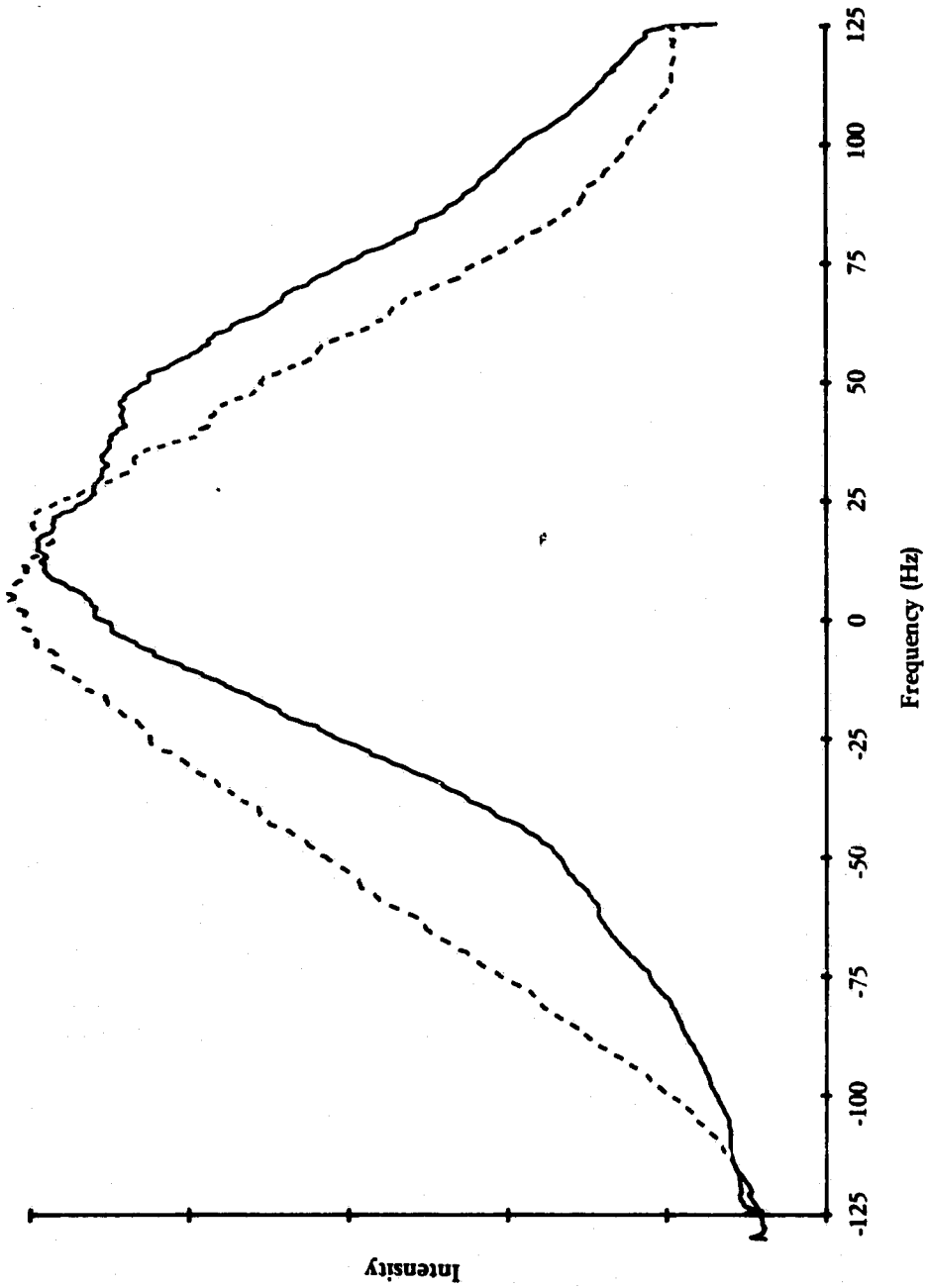


FIGURE 16. DIGITALLY RECORDED AND CORRECTED DOPPLER SPECTRA FOR PORLIER PASS L-BAND AIRCRAFT DATA. (Dashed line indicates land spectrum.)

Next, a set of measurements was attempted for the Seasat data sets listed in Table 2. The Seasat MTF was measured from a section of signal film recorded with a "white noise" input signal, and is shown in Figure 17. It may be noted that the system bandwidth as indicated by this plot is narrower than the expected Doppler bandwidth of 1.2 kHz. Thus, the full Doppler spectrum was not measurable for the Seasat data. It is believed that the system bandwidth is limited primarily by the recording system rather than the processor.

Three Doppler spectra were measured for the Columbia River data set (Orbit 150), including one spectrum over the river itself and two spectra over the land on either side of the river. The centroids of the two land spectra were averaged together and subtracted from the centroid of the water spectrum to yield an apparent Doppler shift of 9.8 Hz. The water spectrum and the average of the two land spectra are shown in Figures 18(a) and (b), respectively. The positive Doppler shift of the water relative to the land indicates a current toward the ground track of the satellite (i.e., west, or out of the river) in agreement with surface truth data. The magnitude of the shift indicates a radial velocity of

$$V_r = \frac{\lambda}{2} \Delta f = 1.15 \text{ m/sec} \quad (23)$$

and a horizontal velocity of

$$V_c = \frac{V_r}{\sin 20^\circ} = 3.37 \text{ m/sec} \quad (24)$$

which is also in fair agreement with the surface truth data. The statistical significance of this result is questionable in view of the large standard deviation of the land spectra (approximately 26 Hz). However, the apparent agreement of the calculated and observed currents is encouraging. Probable causes of the large variance of the land spectra are discussed in Section 3.5.

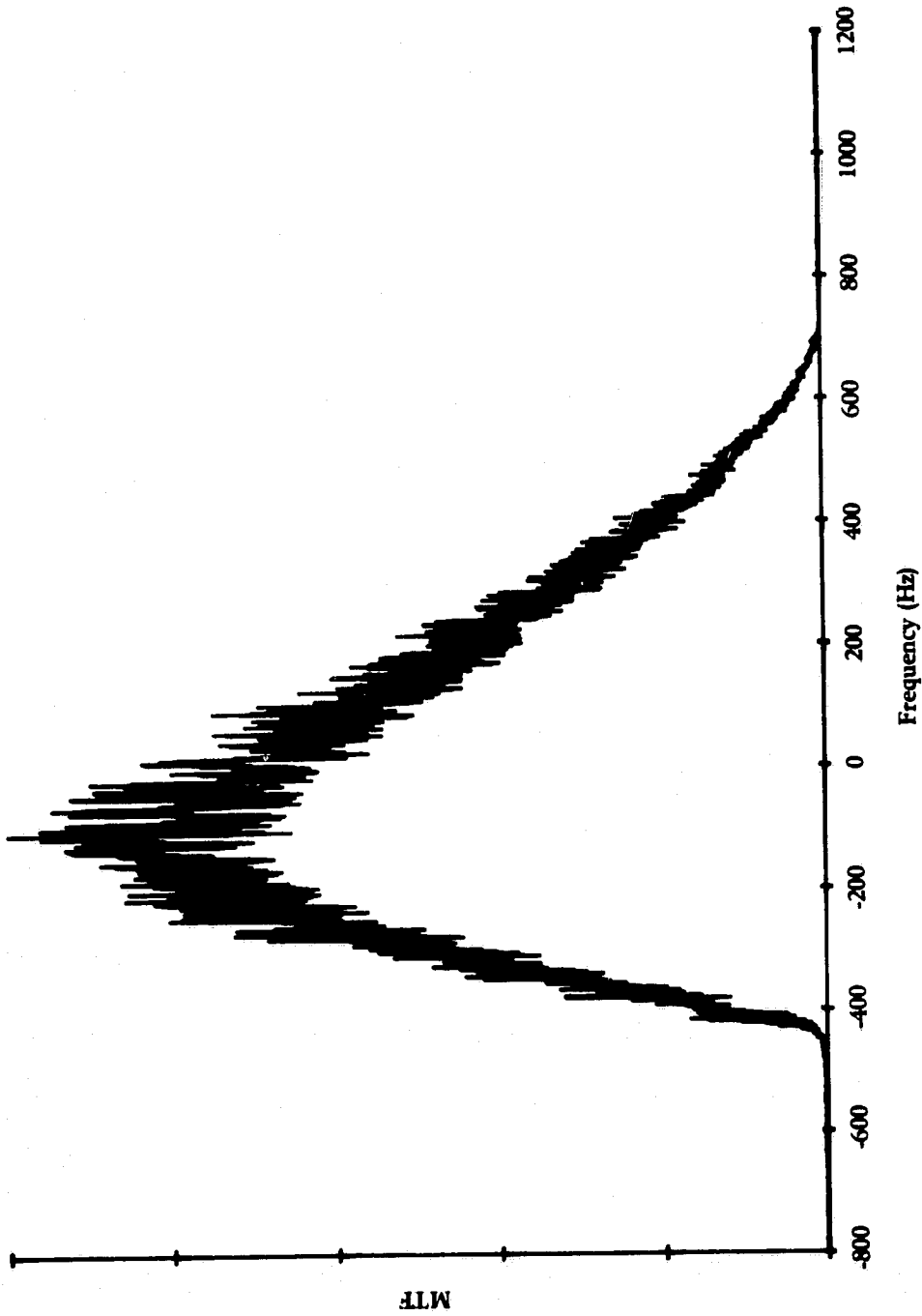


FIGURE 17. SEASAT SYSTEM MODULATION TRANSFER FUNCTION AS MEASURED ON THE ERIM OPTICAL PROCESSOR.

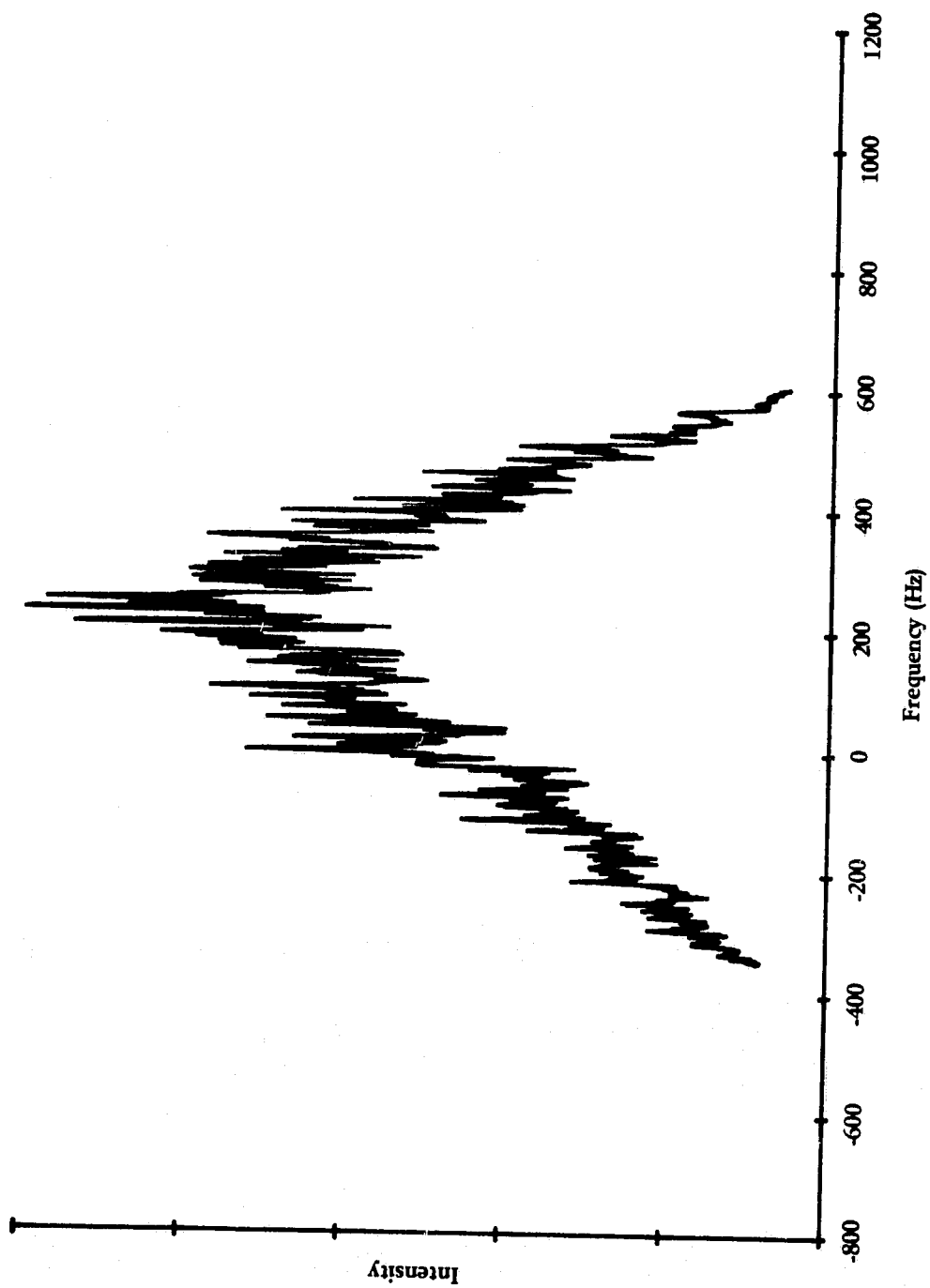


FIGURE 18(a). DOPPLER SPECTRUM FOR COLUMBIA RIVER (SEASAT ORBIT 150).

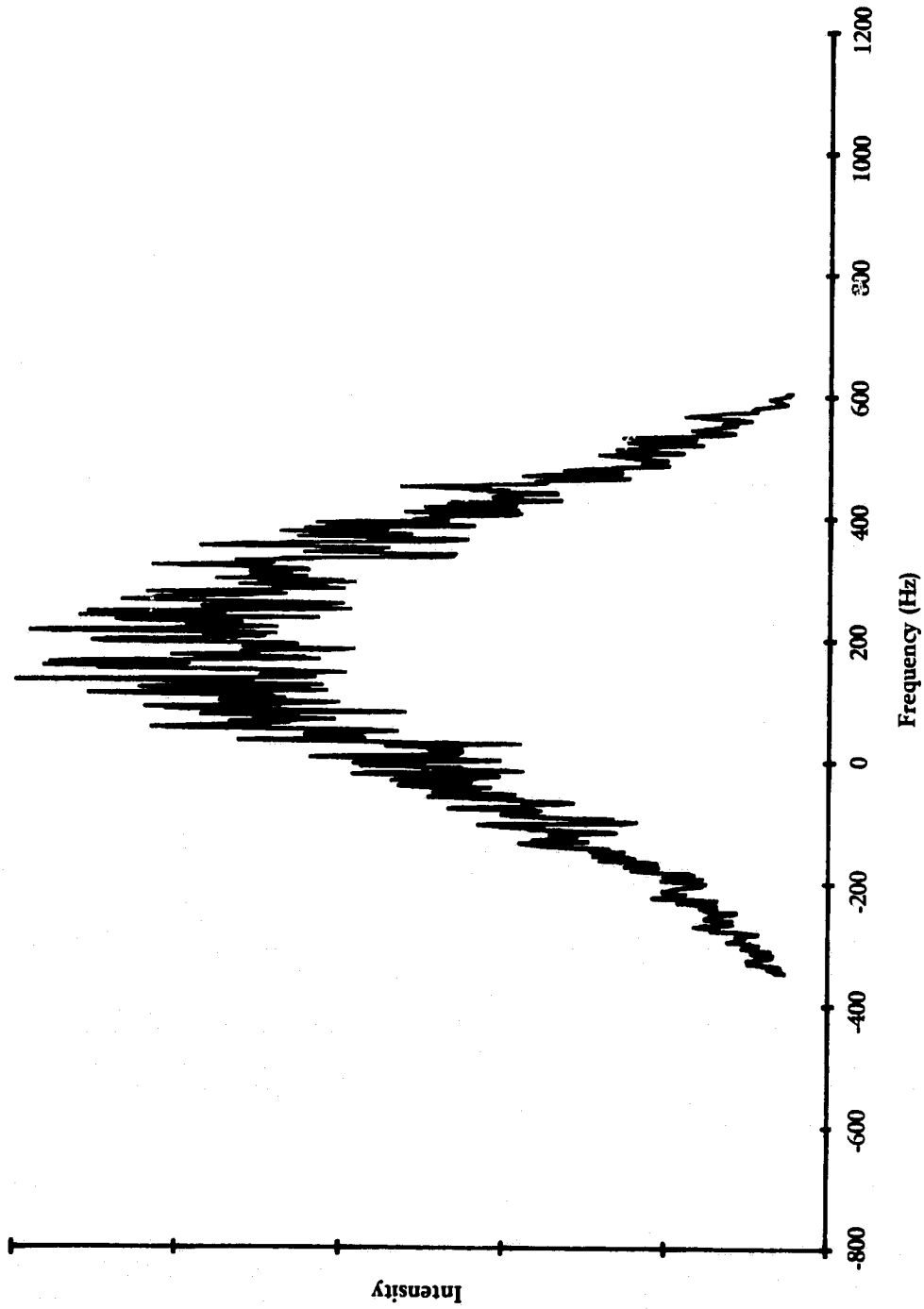


FIGURE 18(b). DOPPLER SPECTRUM FOR LAND AREA ADJACENT TO COLUMBIA RIVER
(SEASAT ORBIT 150).

The next data set processed was taken from Seasat Orbit 762 over the English Channel. Two spectra were measured over water and one over land north of the channel (Figures 19(a)-(c)). The center frequencies of the two water spectra relative to the land spectrum were measured to be 10 Hz and -14 Hz. These Doppler shifts would imply horizontal currents of 3.4 m/sec toward the west, and 4.8 m/sec toward the east, respectively. The first measurement is in the right direction but its magnitude is at least a factor of two too large, as compared with the surface truth data. The second measurement is apparently in the wrong direction. The probable cause of error in the second measurement is the highly variable radar return over the English Channel. As discussed in Section 3.5, such variations in image brightness can cause false spectrum shifts if the signal film illumination is not uniform.

The third set of Seasat measurements was made with data from Orbit 651 over the Gulf Stream off the coast of Florida, at a latitude of approximately 28°N. One spectrum was measured over water near the Florida shoreline and a second was taken from an area assumed to be inside the Gulf Stream, as judged by the apparent position of the Gulf Stream boundary in the image. These spectra are shown in Figures 20(a) and (b). The spectrum from inside the Gulf Stream was found to have a center frequency of 4.2 Hz smaller than that for the stationary water near the shoreline. This would indicate a current having a radial component of 0.5 m/sec, or a horizontal component of 1.4 m/sec in a direction perpendicular to (and away from) the ground track. Since the Gulf Stream boundary appears to be at about a 45° angle from the ground track, this would imply a total current magnitude of

$$\frac{1.4 \text{ m/sec}}{\sin 45^\circ} = 2.0 \text{ m/sec} \quad (25)$$

which is in good agreement with the surface truth information.

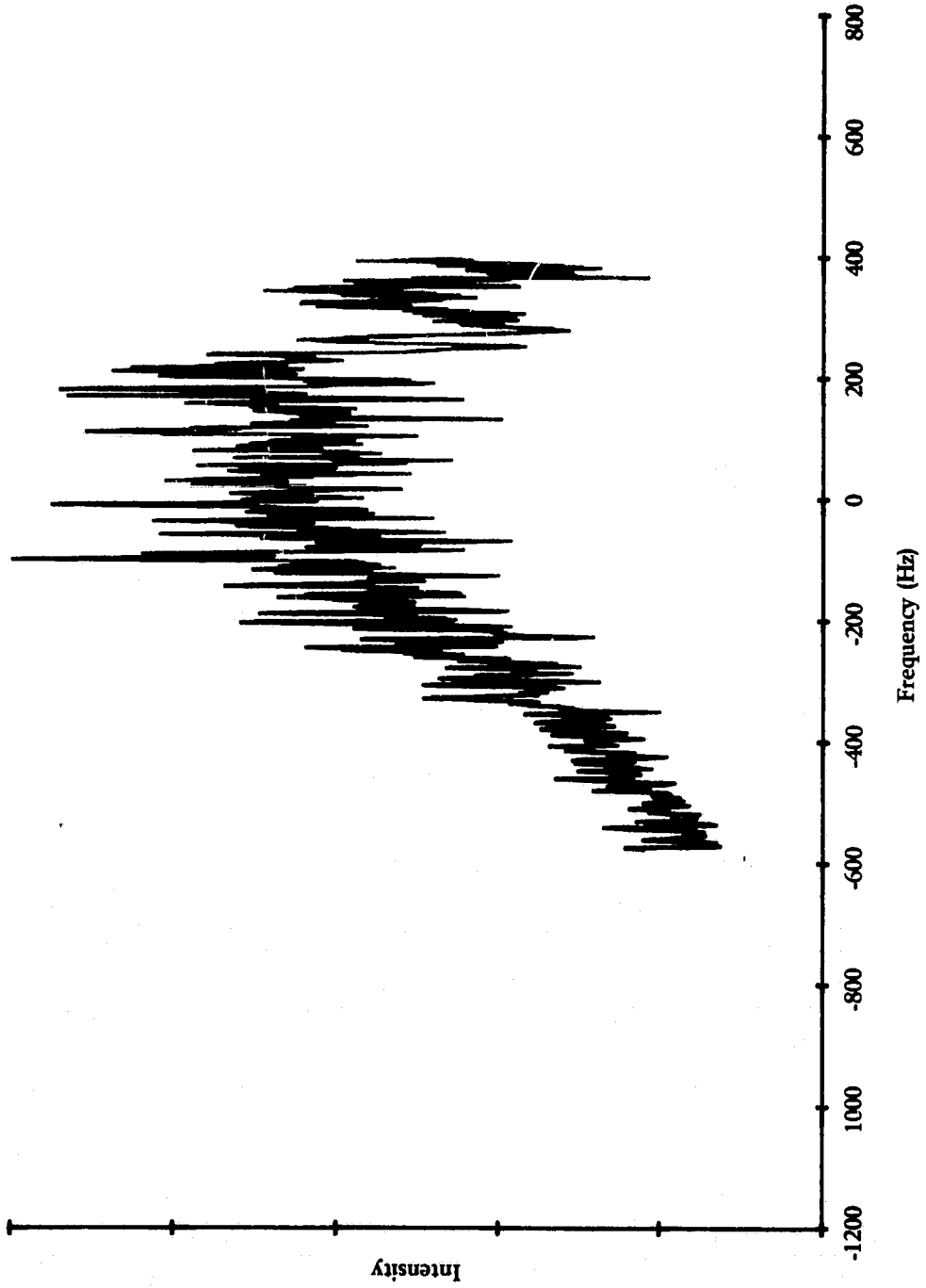


FIGURE 19(a). DOPPLER SPECTRUM FOR DOVER STRAITS AREA 1 (SEASAT ORBIT 762).

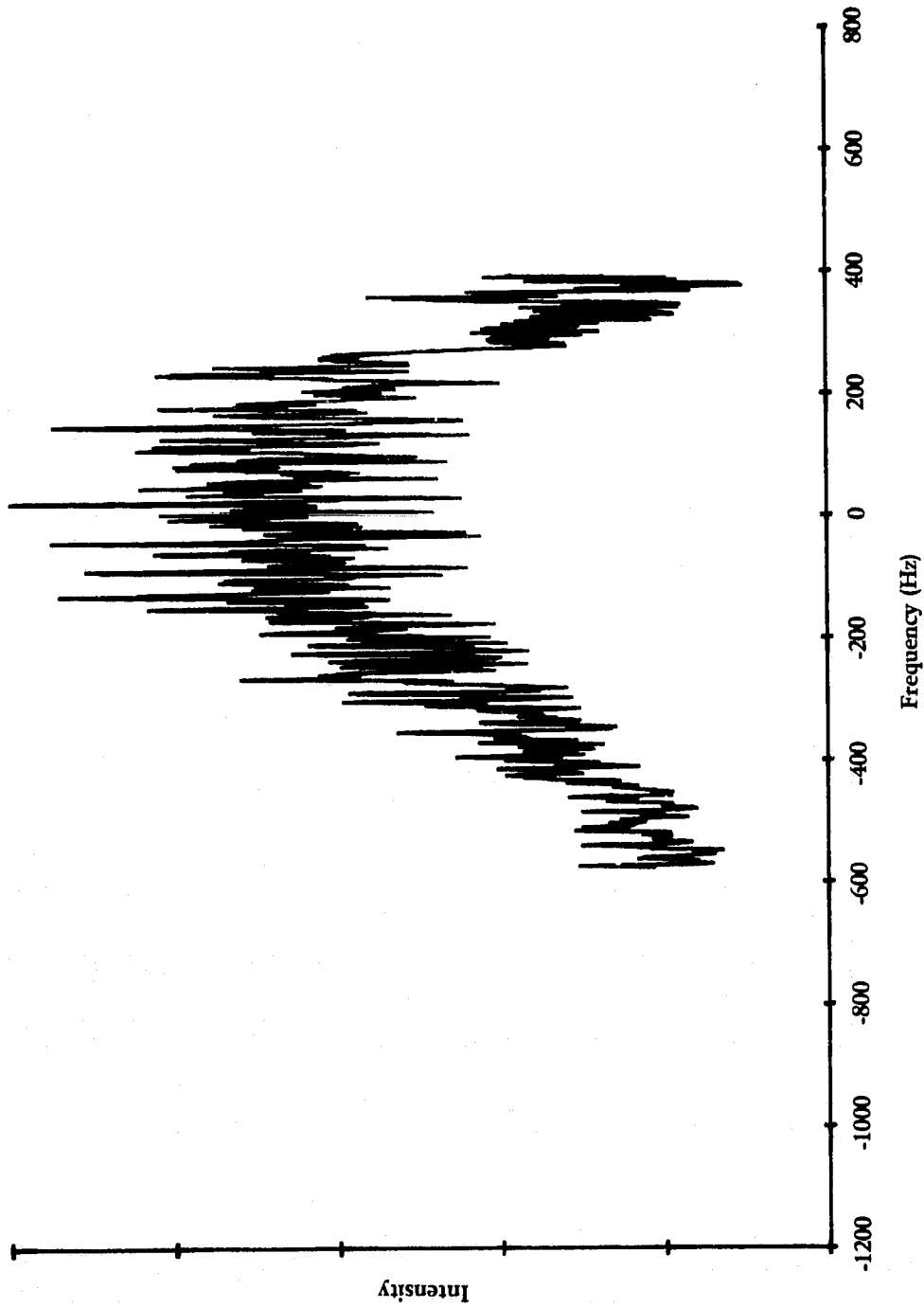


FIGURE 19(b). DOPPLER SPECTRUM FOR DOVER STRAITS AREA 2 (SEASAT ORBIT 762).

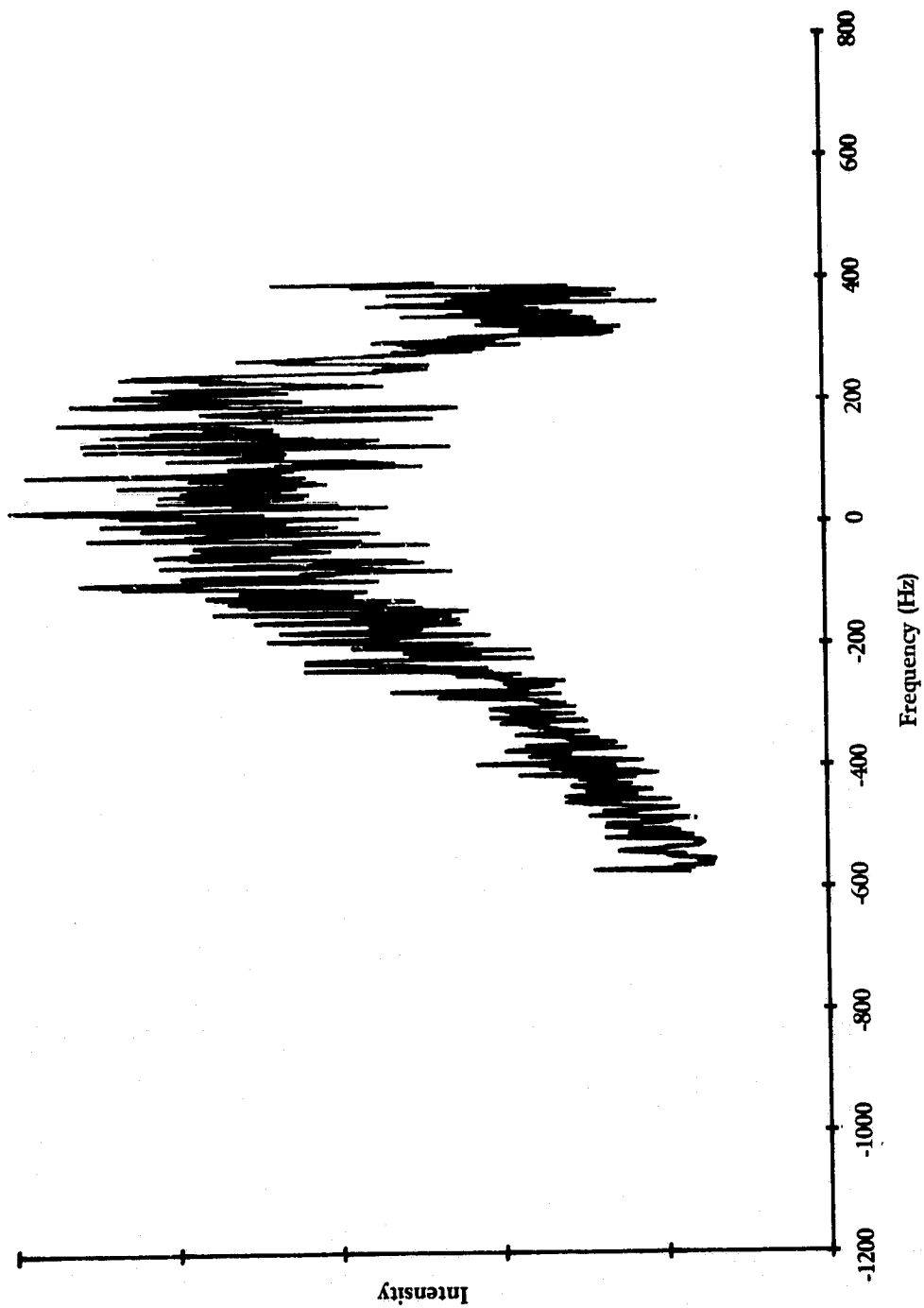


FIGURE 19(c). DOPPLER SPECTRUM FOR LAND NORTH OF DOVER STRAITS (SEASAT ORBIT 762).

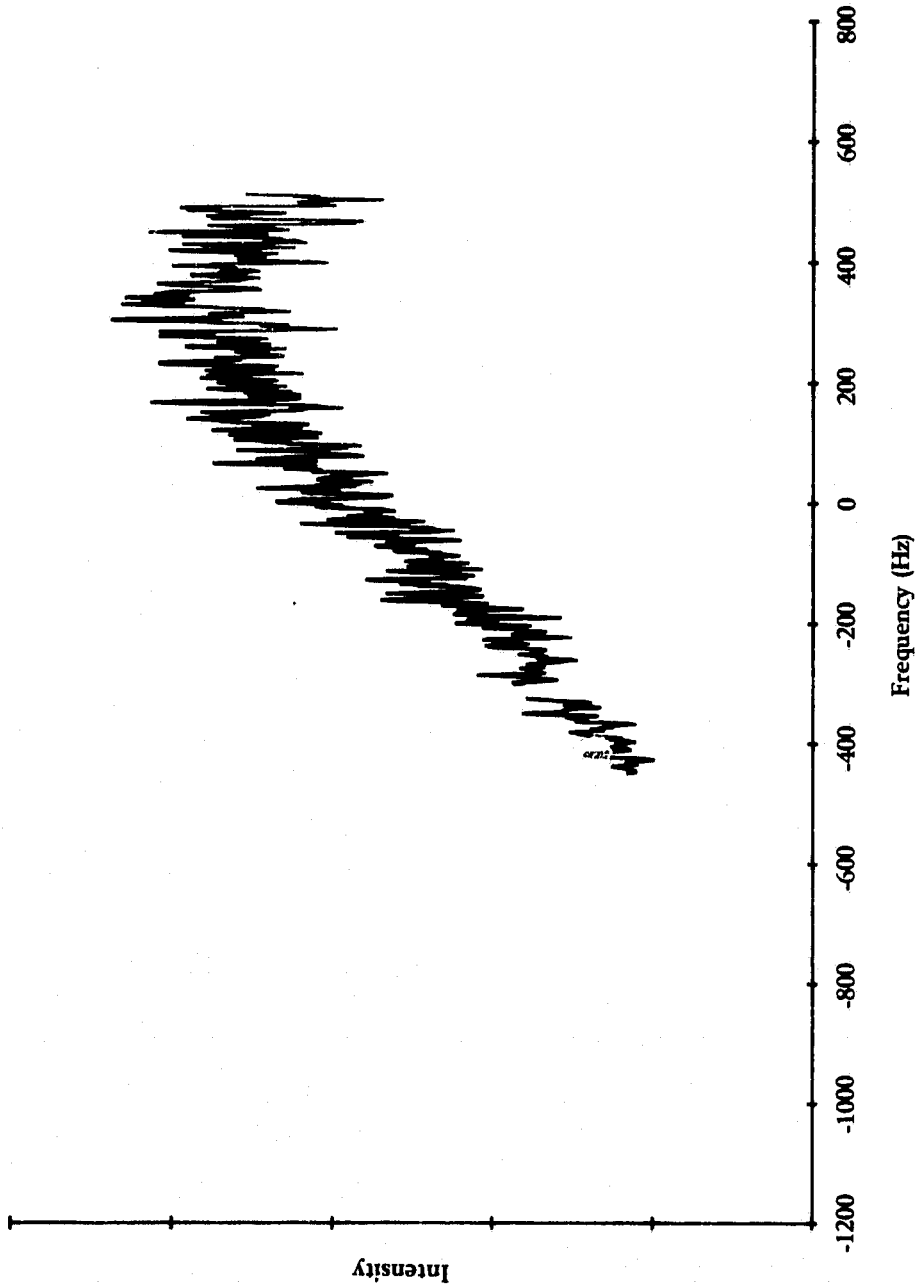


FIGURE 20(a). DOPPLER SPECTRUM FOR STATIONARY WATER AREA OFF FLORIDA COAST (SEASAT ORBIT 651).

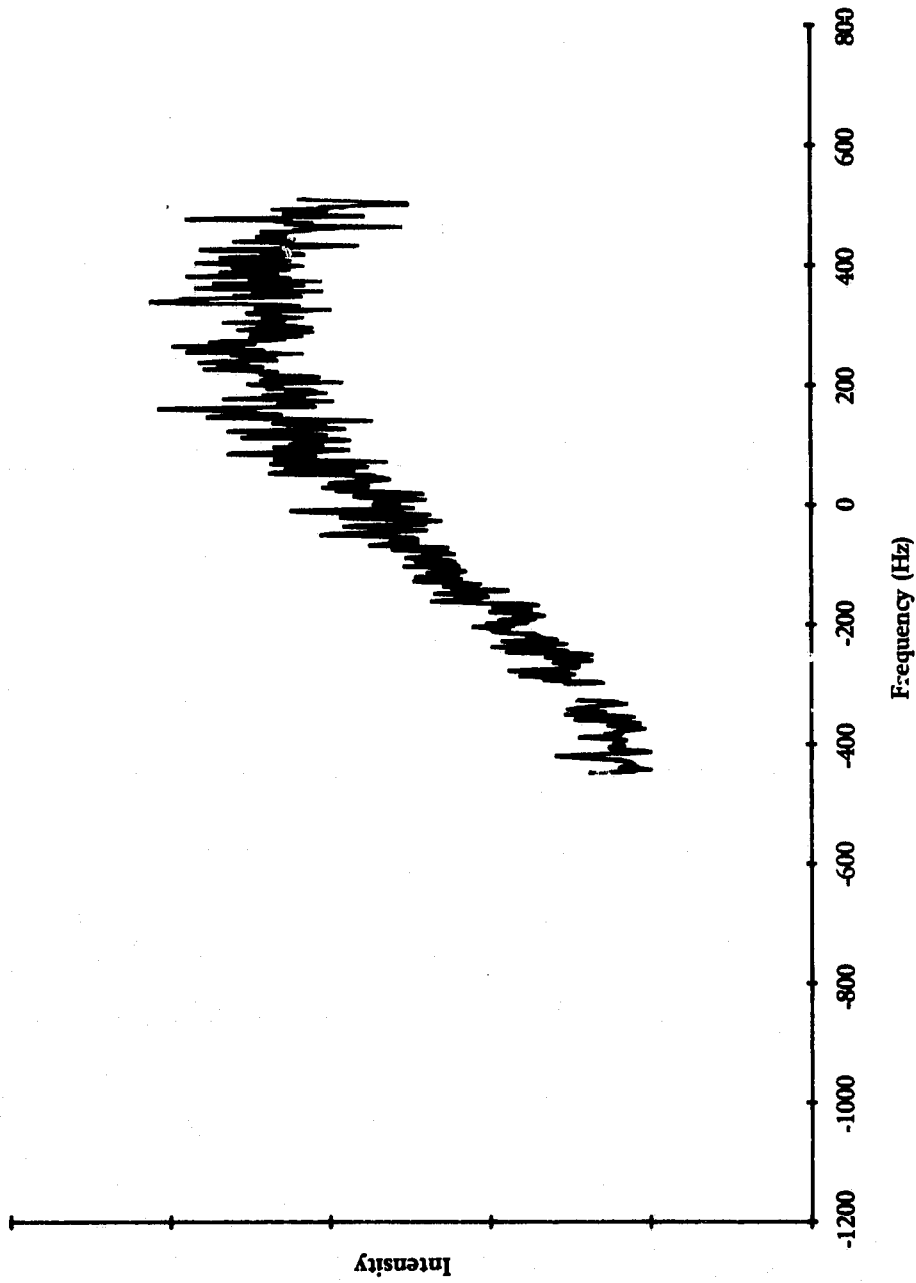


FIGURE 20(b). DOPPLER SPECTRUM FOR GULF STREAM OFF FLORIDA COAST (SEASAT ORBIT 651).

All of the preceding Doppler measurements were made on the ERIM optical processor as described at the beginning of this section. As a test of the feasibility of all-digital processing, a digitally processed complex (I and Q) data set was obtained from R. Gray of the Canadian Communications Research Centre. This data set consisted of an approximately 16 x 16 km segment of Seasat data from Orbit 681, processed at full resolution. The image covers the Straits of Juan de Fuca and includes a small portion of Cape Flattery, Washington. A distinct set of internal waves appears to be propagating into the Straits and a gravity wave field is also evident in the image. Test areas were selected over land, a uniformly high signal area over water, a low signal area over water, and a segment of the internal wave pattern. The first three areas consisted of 256 azimuth samples and a variable number of range samples. A digital Fourier transform was taken for each set of 256 azimuth samples and these spectra were averaged together in the range direction to yield the spectra shown in Figures 21(a)-(c). The means and standard deviations of the individual spectra for the three test areas are shown in Table 3. From these statistics, we can estimate the centroids for the test areas to be -9.1 ± 0.9 Hz for land, -13.6 ± 0.6 Hz for the high-signal water area, and -10.1 ± 0.8 Hz for the low-signal water area. Note that the size of these test areas are on the order of 1 km^2 as compared with the 9 km^2 areas used in the optical Seasat processing, yet the standard deviation of the centroid estimate is much lower.

The difference between the centroids for the two water test areas may be due to a variation in the current or to a systematic error in the spectrum measurement which is related to the signal level. The latter error could be explained by the presence of an additive "white noise" component in the signal, or any type of additive noise with zero mean frequency. This would cause the measured centroid to approach zero as the signal becomes smaller. Assuming this to be

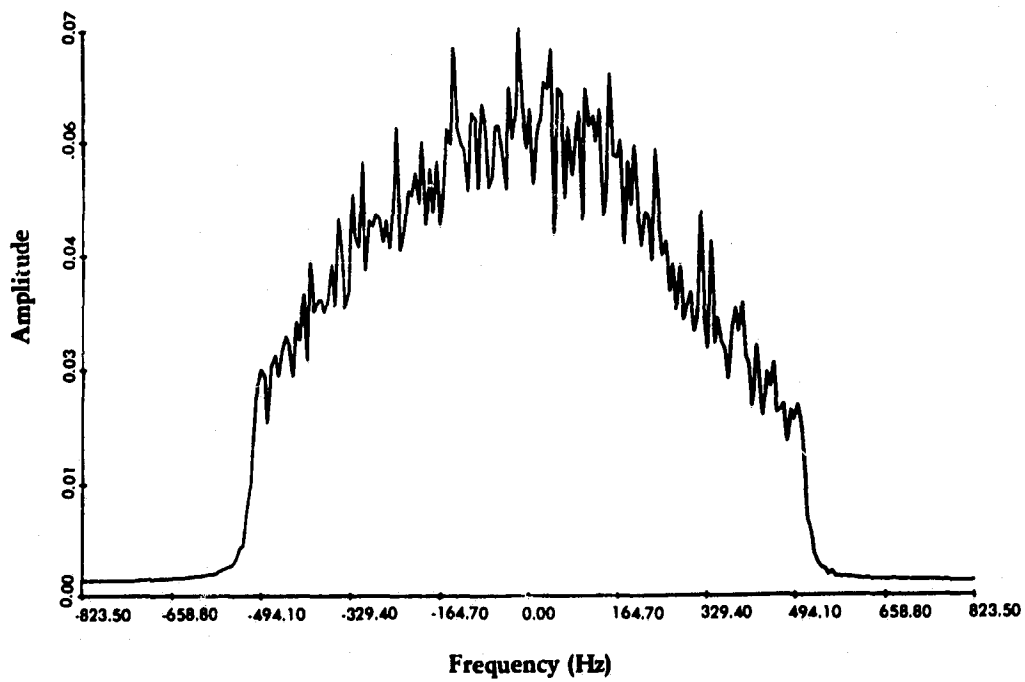


FIGURE 21(a). DOPPLER SPECTRUM FOR LAND AREA IN DIGITALLY PROCESSED DATA SET FOR STRAITS OF JUAN DE FUCA (SEASAT ORBIT 681).

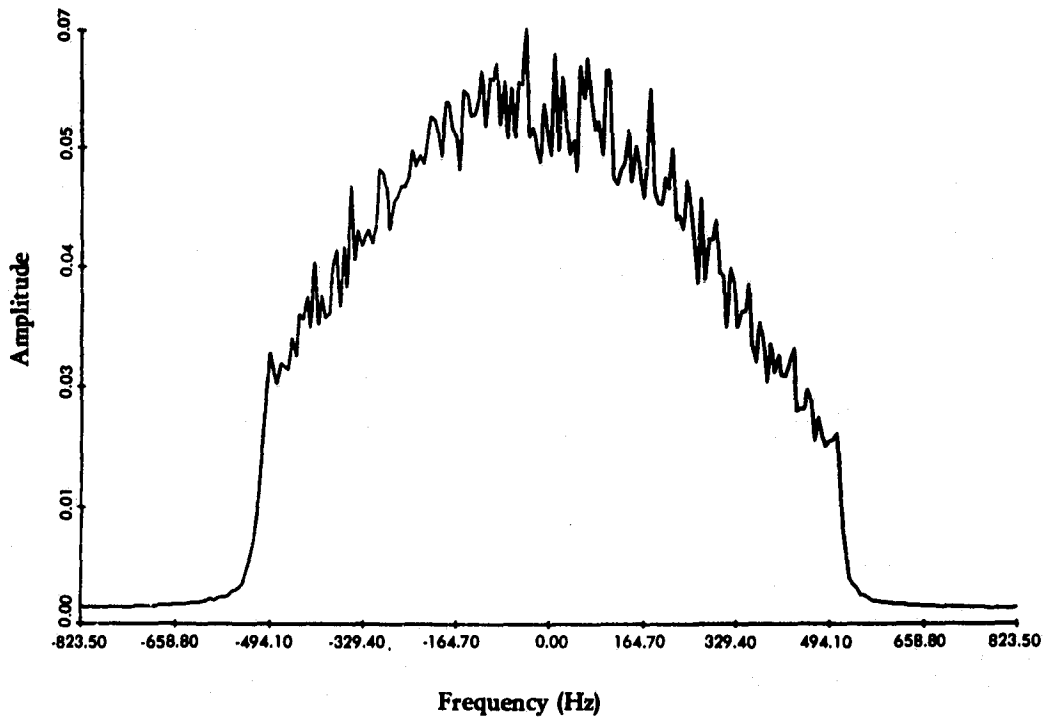


FIGURE 21(b). DOPPLER SPECTRUM FOR HIGH-SIGNAL WATER AREA IN DIGITALLY PROCESSED DATA SET FOR STRAITS OF JUAN DE FUCA (SEASAT ORBIT 681).

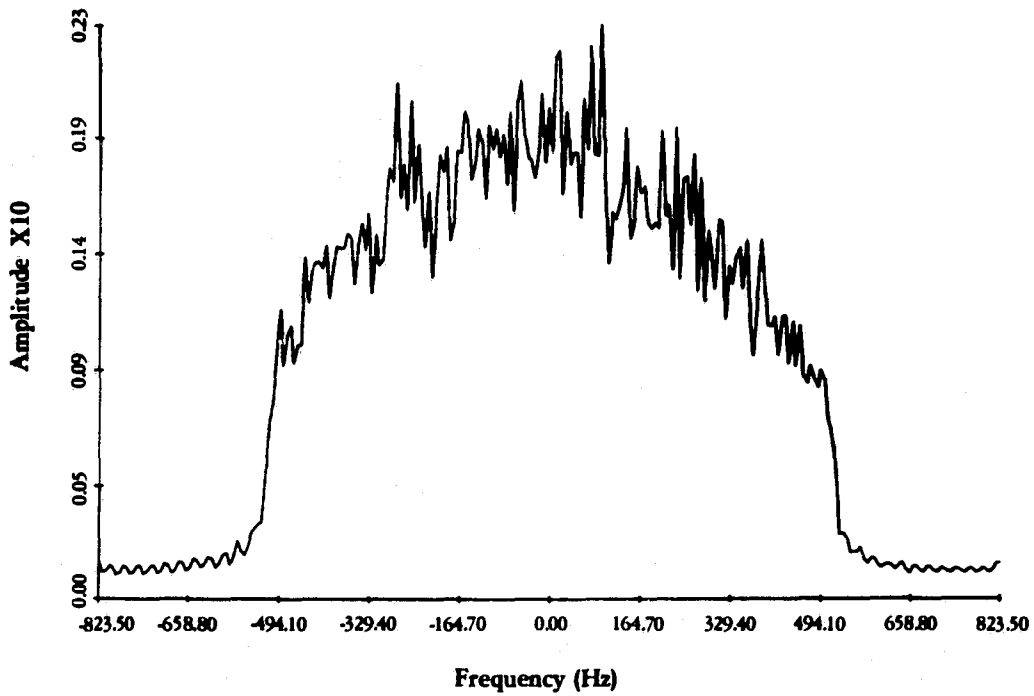


FIGURE 21(c). DOPPLER SPECTRUM FOR LOW-SIGNAL WATER AREA IN DIGITALLY PROCESSED DATA SET FOR STRAITS OF JUAN DE FUCA (SEASAT ORBIT 681).

TABLE 3
 DOPPLER SPECTRUM STATISTICS FOR THREE TEST AREAS
 IN SEASAT ORBIT 681 DIGITAL DATA SET

<u>Test Area</u>	<u>No. of Range Samples</u>	<u>Centroid (Hz)</u>		<u>Amplitude (arbitrary units)</u>	
		<u>Mean</u>	<u>Std. Dev.</u>	<u>Mean</u>	<u>Std. Dev.</u>
Land	151	-9.07	10.98	1.9×10^{-3}	1.9×10^{-4}
Water (high signal)	301	-13.63	10.52	2.0×10^{-3}	1.5×10^{-4}
Water (low signal)	151	-10.08	10.15	6.7×10^{-4}	5.7×10^{-5}

the case, the centroid of the first water test area would be more directly comparable to that of the land area, since the mean signal levels are nearly the same for these two areas. The Doppler shift between these areas is -4.5 Hz, which would imply a horizontal current of 1.5 m/sec into the Straits. This figure is approximately three times higher than the tide table prediction for this area. Averaging the two water test areas yields a Doppler shift of 2.8 Hz and a current of 0.9 m/sec.

A factor which has not been taken into account in these calculations is the phase speed of the Bragg waves responsible for radar scattering from the water surface. At L-band, the wavelength of these Bragg waves for a 20° incidence angle is

$$\lambda_w = \frac{0.235 \text{ m}}{2 \sin 20^\circ} = 0.34 \text{ m} \quad (26)$$

and the phase velocity of these waves is

$$c_w = \sqrt{\frac{\lambda_w g}{2\pi}} = 0.73 \text{ m/sec.} \quad (27)$$

Thus, the Doppler shift due to the phase velocity of the Bragg waves is

$$\Delta f_w = \frac{2c_w \sin 20^\circ}{0.235 \text{ m}} = 2.1 \text{ Hz.} \quad (28)$$

Assuming the direction of propagation of these waves is in the same direction as the large-scale gravity waves visible in the image, i.e., into the Straits, this Doppler shift should be subtracted from the measured shift before the current is calculated. This results in a current estimate of 0.8 m/sec using the high-signal area or 0.2 m/sec using the average of the two test areas. These values bracket the tide table prediction for this area.

Next, a test area covering the internal wave pattern was examined. This area consisted of 1024×1024 samples. A Doppler spectrum was calculated for each set of 1024 azimuth samples, and the

resulting centroid values were smoothed in the range direction using a 100-sample boxcar filter. A plot of these smoothed Doppler centroid values versus the range sample number is shown in Figure 22. The signal amplitude is shown for the same set of range sample numbers in Figure 23. Figure 22 shows variations in the Doppler frequency of about ± 3 Hz correlated with the signal amplitude for the first few cycles of the internal wave (on the left of the plot) and variations of about ± 6 Hz for the two cycles on the right. These Doppler shifts would imply a variation in the horizontal velocity of ± 1 m/sec for the waves on the left side and ± 2 m/sec for the waves on the right side. Comparing the signal amplitude variations in Figure 23 with those in Table 3, it is probable that these velocities are overestimated by at least a factor of two because of the noise effects mentioned earlier. However, a detailed analysis of these effects has not yet been carried out.

No surface truth data is available for these internal waves. However, in situ measurements on a set of smaller internal waves in the Gulf of Georgia indicate velocity fluctuations of ± 0.25 m/sec [Gower and Hughes, 1979]. Therefore, the results obtained from the Doppler analysis appear to be on the proper order of magnitude if the systematic errors are taken into account.

3.4 ORBITAL VELOCITY MEASUREMENTS

Theoretical calculations were presented in Section 3.1 which predict a broadening of the Doppler spectrum due to gravity wave orbital velocities. Figure 24 shows a plot of the amount of this broadening, i.e., the spectrum width divided by the width for a stationary surface, versus the scaled amplitude

$$A = \frac{\Omega a}{\beta V}$$

where Ω is the wave frequency in radians/sec, a is the wave amplitude in meters, β is the antenna beamwidth and V is the platform velocity.

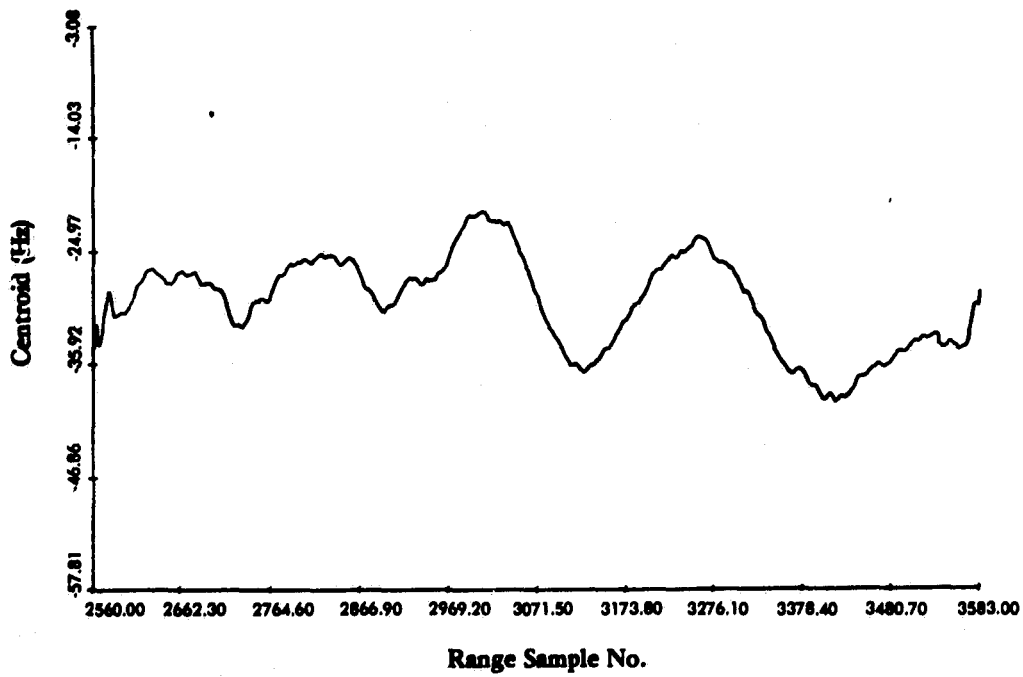


FIGURE 22. DOPPLER CENTROID VERSUS RANGE SAMPLE NUMBER FOR INTERNAL WAVE PATTERN IN STRAITS OF JUAN DE FUCA.

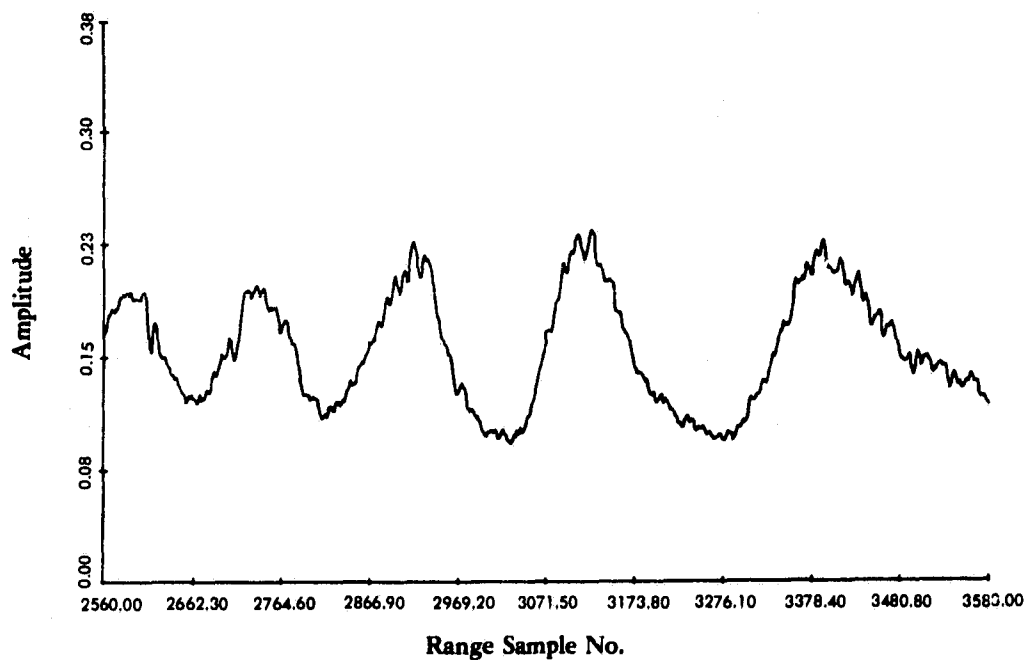


FIGURE 23. SIGNAL AMPLITUDE VERSUS RANGE SAMPLE NUMBER FOR INTERNAL WAVE PATTERN IN STRAITS OF JUAN DE FUCA.

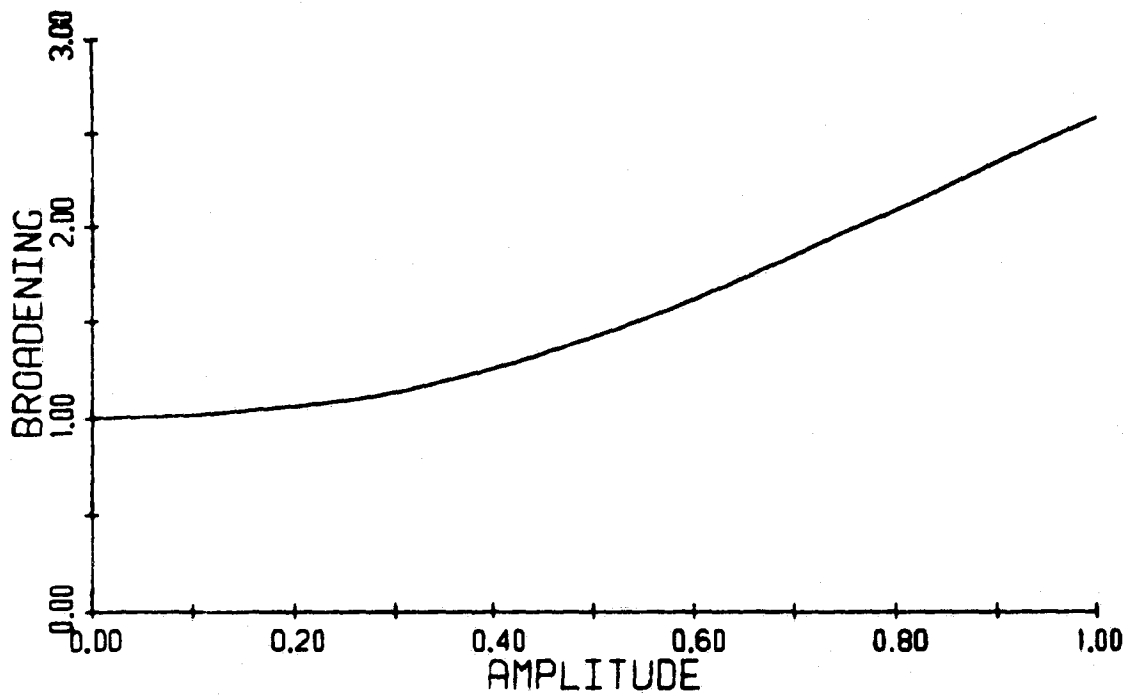


FIGURE 24. DOPPLER BROADENING FACTOR VERSUS SCALED WAVE AMPLITUDE $\left(\frac{\Omega a}{\beta v}\right)$ FOR AIRCRAFT X-BAND AIRCRAFT DATA WITH ANTENNA BEAMWIDTH OF 1.1° AND PLATFORM VELOCITY OF 75 m/sec.

This plot was generated for the same set of parameters as in Figure 3 of Section 3.1, although the results are not strongly dependent on these parameters.

Among the Doppler spectra presented in Section 3.4, the only ones showing a significant amount of broadening are the X-band Marineland spectra. The broadening for these cases range from 1.3 to 2.2 for the water spectra relative to the land spectra. Referring to Figure 24, these would imply a scaled wave amplitude ranging from 0.42 to 0.84.

Surface truth data for the Marineland test site indicate a dominant wavelength of 80 meters and a significant wave height of 1.56 meters. The frequency of these waves, from linear dispersion theory, is

$$\Omega = \sqrt{\frac{2\pi g}{\lambda}} = 0.88 \text{ rad/sec}$$

Using a wave amplitude (a) of one half the significant wave height, a beamwidth $\beta = 0.019$ rad and a platform velocity $V = 80$ m/sec, the scaled amplitude calculated from the surface truth data is

$$A = \frac{\Omega a}{\beta V} = 0.45$$

This would cause a Doppler broadening of approximately 1.4, which is within the range of the observed broadening factors. However, the observation of a much larger broadening in some of the cases (Pass 1 and Pass 3) would seem to imply that the theory presented in Section 3.1 is incomplete, or there is an additional broadening mechanism that has not been taken into account. Further experimental and theoretical work are needed to resolve this question satisfactorily.

3.5 ERROR ANALYSIS

There appear to be at least four factors influencing the apparent Doppler spectra of objects imaged by a SAR in addition to the actual

motion of the objects. If these factors are neglected or if their effects are not distinguishable from actual motion effects, they represent potential sources of error in the determination of ocean currents and orbital velocities from SAR data. These factors are:

1. Variations in backscatter cross section with view angle,
2. Recording system non-uniformities,
3. Effects of recording and/or processing system MTF and noise,
4. Aperture and illumination effects in the processing system.

Each of these factors is discussed in more detail below.

3.5.1 ANISOTROPIC SCATTERING

The apparent Doppler spectrum of an object or area will be distorted if the radar cross section varies over the duration of the signal history, i.e., if the cross section is a function of the viewing angle. An evaluation of this effect can be carried out by including the cross section in the expressions developed in Section 3.1. Re-defining $A(\phi)$ in Eq. (3) as

$$A(\phi) = \sqrt{\sigma(\phi)} g(\phi) \quad (29)$$

where $\sigma(\phi)$ is the radar cross section of the target and $g(\phi)$ is the antenna gain pattern, the Doppler spectrum for a stationary target may be written as

$$|\tilde{F}(\omega)| = \left| \int_{-\infty}^{\infty} \sqrt{\sigma\left(\frac{Vt}{R_0}\right)} g\left(\frac{Vt}{R_0}\right) e^{j(bt^2 + \omega t)} dt \right| \quad (30)$$

If the angular variation of the cross section is relatively slow, $\sigma(\phi)$ can be expanded in a Taylor series, and

$$\sqrt{\sigma(\phi)} \approx \sqrt{\sigma(0)} \left(1 + \frac{\sigma'(0)}{2\sigma(0)} \phi \right) \quad (31)$$

For small ϕ , the above integral can then be evaluated to yield

$$|\tilde{F}(\omega)| = \sqrt{\sigma(0)} \left| \tilde{F}_0(\omega) - j \frac{\sigma'(0)V}{2\sigma(0)R_0} \tilde{F}'_0(\omega) \right| \quad (32)$$

where $|\tilde{F}_0(\omega)|$ is the Doppler spectrum for a target with unit cross section. Assuming a Gaussian form for the antenna gain pattern, as in Section 3.1, we can write

$$\tilde{F}'_0(\omega) = \frac{-\omega}{2 \left[\left(\frac{2V}{\beta R} \right)^2 - jb \right]} \tilde{F}_0(\omega) \quad (33)$$

and

$$|\tilde{F}(\omega)| \approx \sqrt{\sigma(0)} \left[1 - \frac{\sigma'(0)V}{4\sigma(0)R_0 b} \omega \right] |\tilde{F}_0(\omega)| \quad (34)$$

since $b \gg (2V/\beta R)^2$. The centroid of this spectrum is located at

$$\Delta\omega = \frac{-\frac{\sigma'(0)V}{4R_0 b} \int_{-\infty}^{\infty} \omega^2 |\tilde{F}_0(\omega)| d\omega}{\sigma(0) \int_{-\infty}^{\infty} |\tilde{F}_0(\omega)| d\omega} = \frac{\sigma'(0)}{8\sigma(0)} k\beta^2 V \quad (35)$$

Expressed as a fraction of the Doppler bandwidth $\beta' = 2k\beta V$, the shift caused by a non-isotropic scatterer is

$$\frac{\Delta\omega}{\beta'} = \frac{\sigma'(0)\beta}{16\sigma(0)} = \frac{1}{16} \frac{\Delta\sigma}{\sigma(0)} \quad (36)$$

where $\Delta\sigma$ is the change in the radar cross section during the time that the object is in the field of view of the antenna. The degree of anisotropy required to produce a shift on the same order of magnitude as that seen in Seasat data is quite certain to occur over land targets, and is possible over water as well. The anisotropy of the ocean backscatter coefficient depends on the angular dependence of the wave height spectrum at short wavelengths, which is not well known. Assuming the wave height spectrum to have a $\cos^4(\theta/2)$ dependence [Tyler, et al., 1974], where θ is the direction of the Bragg

wave relative to the wind direction, the rate of change of the radar cross section (including Bragg waves travelling in both the positive and negative range directions) is

$$\frac{\sigma'(\theta)}{\sigma(\theta)} = \frac{-2 \sin \theta \cos \theta}{\sin^4 \left(\frac{\theta}{2}\right) + \cos^4 \left(\frac{\theta}{2}\right)} \quad (37)$$

Thus, for a view angle of 45° relative to the wind direction,

$$\frac{\sigma'(\theta)}{\sigma(\theta)} = 0.667$$

and the apparent Doppler shift caused by this anisotropy for Seasat data ($\beta = 1.73^\circ$) is

$$\frac{\Delta\omega}{\beta^r} = 0.0125$$

i.e., about 1.5 Hz, which is equivalent to the shift caused by a horizontal current of about 0.5 m/sec.

3.5.2 RECORDING SYSTEM NON-UNIFORMITIES

An effect similar to that described above could also be caused by changes in recording system parameters over the duration of the Doppler signal history. Such changes can be produced by variations in receiver gain, CRT bias, and/or film response. Film response variations can be induced either by emulsion non-uniformities or by the development process. Variations are not likely to be more than a few percent over a typical signal history, but may be of the same order of magnitude as the spectrum changes induced in Seasat data by ocean currents.

The phenomenon of small signal suppression represents another possible error source, in which the apparent Doppler spectrum is influenced by brightness variations in the scene. The signal film density (or transmission) at any point actually represents the superposition of many Doppler histories. As long as this superposition

is linear, the individual Doppler histories contribute equally (in proportion to their scattering cross sections) to the total. However, because of film response nonlinearities, the actual effect of a bright object's Doppler history is to reduce the effective contributions of the overlapping histories. This effect will cause the frequency spectra for nearby objects to be skewed, resulting in an erroneous Doppler shift. Although the effect is more prevalent over land, because of the larger range of reflectivities, it may be also present to some degree over water.

3.5.3 RECORDING SYSTEM MTF AND NOISE

Another factor influencing the apparent Doppler spectrum is the recording system frequency response and noise. The film recording medium obviously has an upper limit on the spatial frequency that can be recorded, and in fact the recording efficiency falls off continuously with frequency. This falloff is specified in terms of the modulation transfer function (MTF). In order to properly correct for this system characteristic, the measured spectrum should be divided by the MTF.

If the system bandwidth is greater than the signal bandwidth (i.e., the Doppler spectrum width), a correction can be made for the system MTF as outlined above, and the entire spectrum can be used to measure the Doppler shift and hence estimate the ocean current. If the system bandwidth is smaller than the signal bandwidth, as it may be in the case of Seasat data, the MTF correction can still be made, but only a portion of the Doppler spectrum can be recovered with adequate signal-to-noise ratio. Thus, the location of the centroid and the amount of the Doppler shift is difficult to measure.

There is also an additive correction factor which should be applied to the measured Doppler spectrum to remove the effect of the system noise background. Assuming that the noise entering the

recording system is frequency-independent, the shape of the noise component recorded will be the same as the shape of the MTF. If the signal is very large, the noise component may be negligible, but when the signal is low (as it frequently is over water), the noise spectrum may be an appreciable or even a dominant component of the recorded Doppler spectrum.

3.5.4 APERTURE AND ILLUMINATION EFFECTS

The azimuth frequency scan is obtained for an appropriate subset of the image by setting up the optical processor in a conventional manner up to the image plane. Instead of placing a film at the image plane, however, a small aperture is inserted so as to pass only those signals which correspond to the subset of the image under consideration. These signals are passed through an additional set of optics which essentially take the Fourier transform of the signals in the image plane. The light intensity in the resulting frequency plane is then scanned in the azimuth direction and recorded.

Ideally, the result of this process would be the average power spectrum (i.e., the amplitude of the Fourier transform) of the Doppler histories of all the objects within the image subset selected. The results should not be influenced by objects outside this area, even though their Doppler histories overlap those of the targeted objects, and the results should not depend upon the positions of the objects within the subset. In order to realize these objectives, the following conditions must be met:

1. The length of signal film illuminated must be at least equal to the length of an individual Doppler history plus the width of the image plane aperture (in equivalent units), and must be centered about the Doppler history of the object at the center of the image aperture,
2. The illumination must be uniform over this area, and
3. The aperture must be located precisely at the image plane.

If the first condition is not met, the high (positive or negative) frequency components of some of the Doppler histories will be truncated and the frequency distribution will be skewed, resulting in an apparent but false Doppler shift.

If the second condition is not met, the frequency distribution of each individual scatterer will be skewed, and the contributions from all the scatterers will be unequally weighted. This will again result in a false Doppler shift which is dependent on the brightness distribution in the scene.

If the third condition is not met, a perfect discrimination between objects inside and outside the image subset will not be achieved, and the measured frequency spectrum will be skewed by bright objects near the edges of the aperture. It is conceivable that this effect may always be present to a small extent (depending on the aperture size) due to diffraction effects at the edges of the aperture.

These conditions are all, in principle, controllable and therefore do not constitute a fundamental limitation of the technique (with the possible exception of the last-mentioned diffraction effect). It may be difficult to control these factors in practice, however, and failure to meet the conditions exactly can lead to large errors. This is particularly true for Seasat data which typically has signal histories occupying a much longer film distance than aircraft data. The following set of measurements serves to illustrate and quantify this error source.

The optical processor was arranged for Seasat processing and the signal film illumination pattern was widened as much as possible using the conventional setup. This resulted in a falloff of 2.2 dB in the illumination at the edges of the 60 mm aperture. A signal film from Seasat Orbit 982 over Goldstone Antenna was placed in the processor so that the image of the antenna was centered in the aperture, and the Doppler spectrum was measured. Next, the signal film

was moved so that the image appeared near the left edge of the 3 km aperture and the spectrum was re-measured. Finally, this was repeated with the Goldstone antenna image near the right edge of the aperture. The three recorded spectra (with corrections for system MTF and noise) are shown in Figure 25. There is a shift of approximately 100 Hz for each of the off-axis spectra as compared with the centered spectrum.

A theoretical explanation of this effect can be developed by extending the analysis presented in Section 3.1 to include the effects of the signal film illumination function, and to consider signal histories located off the axis of the processor. The analysis in Section 3.1 assumed that the object was broadside to the antenna at $t = 0$. For an object located an along-track distance x away from this point, the signal history is shifted in time by an amount x/V : i.e.,

$$S_1(x, t) = \sqrt{\sigma} g\left(\frac{Vt - x}{R_0}\right) \exp\left[j \frac{V^2}{2R_0} \left(t - \frac{x}{V}\right)^2 - V_r \left(t - \frac{x}{V}\right)\right] \quad (38)$$

If the signal-film illumination function is designated as $W(t)$, the output of the processor may be written as

$$S_2(x, t') = \int_{-\infty}^{\infty} S_1(x, t) W(t) q(t - t') dt \quad (39)$$

which has the Fourier transform

$$\tilde{S}_2(x, \omega) = Q(\omega) \int_{-\infty}^{\infty} S_1(x, t) W(t) e^{j\omega t} dt \quad (40)$$

where $Q(\omega)$ is the Fourier transform of the matched filter $q(t)$. Assuming the illumination function is Gaussian with width T_a , i.e.,

$$W(t) = e^{-4t^2/T_a^2} \quad (41)$$

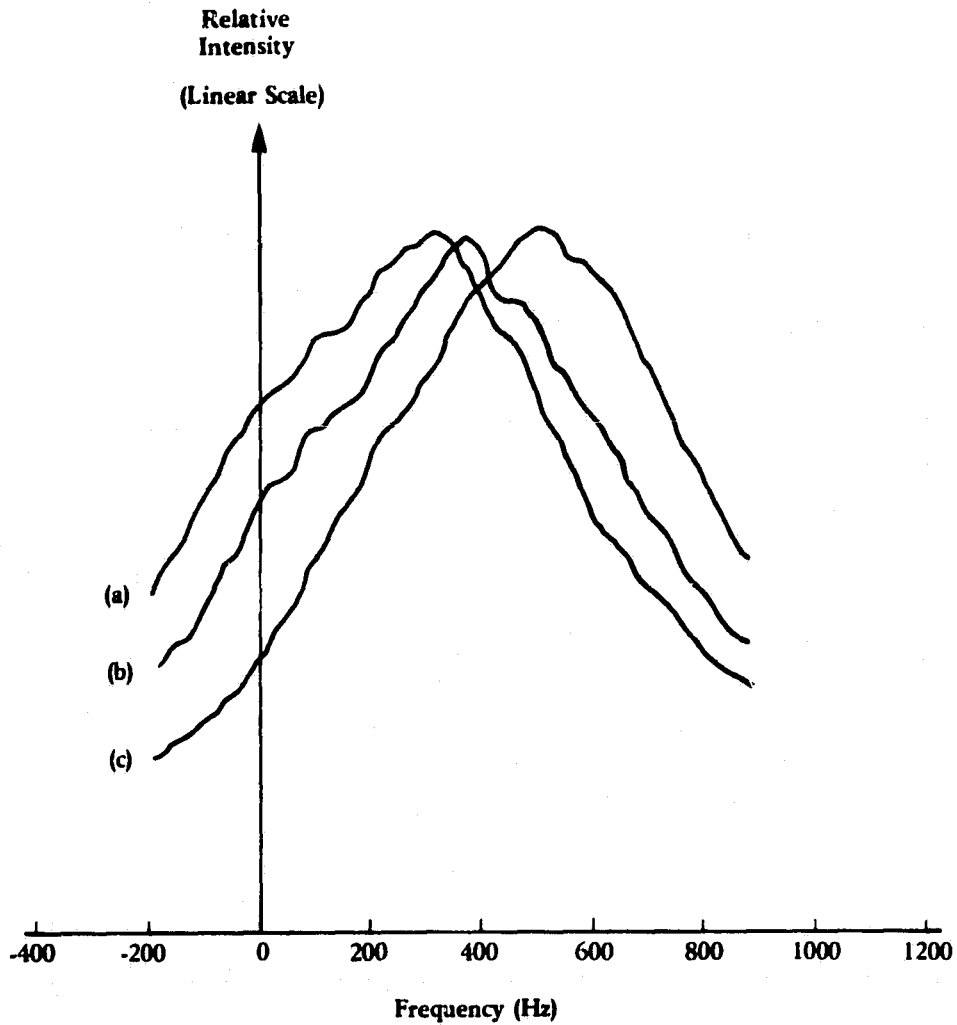


FIGURE 25. DOPPLER SPECTRA MEASURED FOR GOLDSTONE ANTENNA WITH IMAGE OF ANTENNA (a) AT LEFT EDGE OF APERTURE, (b) CENTERED IN APERTURE, AND (c) AT RIGHT EDGE OF APERTURE.

the above integral can be evaluated to yield the result

$$\begin{aligned} \tilde{S}_2(x, \omega) = Q(\omega) \exp \left\{ - \left(\frac{2x}{VT_a} \right)^2 + j\omega \frac{x}{V} \right\} \\ \exp \left\{ \frac{\left(\left(\frac{2x}{VT_a} \right)^2 - \left(\frac{\omega + \omega_d}{4} \right)^2 - j \frac{x}{VT_a^2} (\omega + \omega_d) \right)}{\frac{1}{T^2} + \frac{1}{T_a^2} - j b/4} \right\} \end{aligned} \quad (42)$$

where $T = \beta R/V$ and $\omega_d = 2kV_r$. Thus, the amplitude of the Doppler spectrum for a point target at x is

$$\begin{aligned} |\tilde{S}_2(x, \omega)| = |Q(\omega)| \exp \left\{ - \left(\frac{1}{bT} \right)^2 (\omega + \omega_d)^2 \right\} \\ \exp \left\{ - \left(\frac{2}{VT_a} \right)^2 \left[x + \frac{V}{2b} (\omega + \omega_d) \right]^2 \right\} \end{aligned} \quad (43)$$

This equation shows that for a point target whose Doppler history is centered in the processor (i.e., at $x = 0$), there is no shift in the spectrum although the spectrum is narrowed by the factor $(1 + T^2/T_a^2)^{-1/2}$. For a point target located off-axis, there is a false shift

$$\Delta\omega = \frac{2bx}{V} \left(1 + \frac{T_a^2}{T^2} \right)^{-1} \quad (44)$$

in the spectrum. The factor $Q(\omega)$ represents the frequency response of the processor, which can also cause a reduction in the observed Doppler shift. However, this factor can be corrected for by the methods discussed in Section 3.5.3 above. The shift caused by the aperture or illumination effort is not removable by post-processing, although it can be minimized by choosing test areas which have a uniform or symmetric brightness distribution. For a test area which

is, say, 50 percent brighter on one side of the aperture than the other, the spectrum can be approximated by the appropriately weighted superposition of the spectra for two point objects at $x = \pm x_a/4$, where x_a is the total width of the image plane aperture. The centroid of this spectrum would be

$$\begin{aligned} \omega_c &= \frac{1}{2.5} \left[\omega_d - \frac{bx_a}{2V} \left(1 + \frac{T_a^2}{T^2} \right)^{-1} \right] + \frac{1.5}{2.5} \left[\omega_d + \frac{bx_a}{2V} \left(1 + \frac{T_a^2}{T^2} \right)^{-1} \right] \quad (45) \\ &= \omega_d + \frac{bx_a}{10V} \left(1 + \frac{T_a^2}{T^2} \right)^{-1} \end{aligned}$$

that is, the error in the centroid divided by the bandwidth $2bT$ is

$$\frac{\Delta\omega}{2bT} = \frac{x_a}{10VT} \left(1 + \frac{T_a^2}{T^2} \right)^{-1} \quad (46)$$

If the signal plane aperture width is approximately the same as the signal history (i.e., $T_a \approx T$) and the image aperture width is 3 km, as in the case of the Seasat optical measurements reported here, this would represent a spectrum shift of about 1 percent of the spectrum width, i.e., 10 Hz.

Such a shift can easily mask the actual Doppler shift due to ocean currents, and probably represents the dominant error source in the Seasat measurements. Note that this effect may also be present in digitally processed data, depending on the number of azimuth samples used in the correlation process.

4
PHASE VELOCITY MEASUREMENTS

Since a SAR image is generated from a Doppler history which is acquired over a period of time on the order of a few seconds, it has been proposed that by considering only a portion of each Doppler history, a set of images could be generated which correspond to different time intervals during the acquisition of the data. Moving objects should then appear in different relative locations within these sub-images. This technique would not apply to fully coherent targets, since those having velocities large enough to cause a measurable displacement would have Doppler spectra outside of the system bandwidth. However, in the case of gravity waves on the ocean surface, the individual scatterers move with the orbital velocity of the wave while the positions of the wave crests move with the phase velocity, which can be orders of magnitude larger than the orbital velocity.

The theory for this method of measuring the phase velocity of a gravity wave is presented in Section 4.1, and a set of measurements supporting the theory and demonstrating the technique is presented in Section 4.2.

4.1 THEORY

The rate of change in the phase of the SAR signal reflected from a point object is given by

$$\omega_d = \frac{d\phi}{dt} = -2k \frac{dR}{dt} \quad (47)$$

where k is the radar wave number and R is the instantaneous range distance to the object. This rate of change is referred to as the Doppler frequency of the SAR signal. For an object having a nominal range R_0 (at $t = 0$), the instantaneous range is

$$R(t) = \sqrt{R_0^2 + V^2 t^2} \approx R_0 + \frac{V^2 t^2}{2R_0} \quad (48)$$

where V is the platform velocity. Thus, the instantaneous Doppler frequency is

$$f_d = \frac{\omega_d}{2\pi} = \frac{-2V^2}{\lambda R_0} t \quad (49)$$

If we apply a bandpass filter (i.e., place an aperture in the frequency plane of the optical processor) to the SAR data such that frequencies between f_1 and f_2 are passed, this is equivalent to including only those signals which were collected during the time interval t_1 and t_2 relative to the zero-Doppler time for each object in the scene, where

$$t_i = \frac{-\lambda R_0}{2V^2} f_i \quad (50)$$

If we make an image of the scene using this frequency interval, the positions of the objects in the image will correspond to their positions in the scene at the time

$$\bar{t}_1 = \bar{t}_1 + \frac{X_i}{V} \quad (51)$$

where \bar{t}_1 is an appropriate average over the time interval (t_1 , t_2) corresponding to the frequency interval (f_1 , f_2) selected, and X_i is the along-track coordinate of the object under consideration. If we make a second image using a different frequency interval, such that the average of the corresponding time interval is \bar{t}_2 , the position of the i th object in this image will be shifted relative to its position in the first image by an amount

$$\Delta \vec{r}_i = \vec{v}_i (\bar{t}_2 - \bar{t}_1) \quad (52)$$

where \vec{v}_i is the velocity of the object.

For the case of a gravity wave field being imaged by a SAR, the moving "objects" are actually collections of scattering centers which are themselves moving slowly compared to the phase velocity of the gravity wave, but which are varying in brightness in such a way that the locus of points having the maximum brightness moves with the phase velocity of the wave. This phase velocity is frequently large enough to cause a measurable change in the position of the wave crest during the imaging time. Thus, the phase velocity ought to be measurable by determining the shift in the position of the wave crests in images generated from different Doppler bands.

4.2 MEASUREMENTS

An experiment was carried out to test the technique outlined above using L-band SAR data collected by the ERIM X-L system over Marineland, Florida, on 14 December 1975. For the particular data set (Pass 2) chosen, a gravity wave field with a dominant wavelength of 80 meters was present, traveling in the range direction. From linear dispersion theory, the phase velocity of these waves is

$$C_w = \sqrt{\frac{\lambda g}{2\pi}} = 11.2 \text{ m/sec} \quad (53)$$

where λ is the wavelength and g is the acceleration of gravity.

Four digital images were generated from this data set using four different Doppler frequency bands. The frequency intervals used for each image are shown in Table 4. A typical Doppler spectrum for this data set is shown in Figure 26. This spectrum may be approximately represented by the function

$$A(f) = e^{-\frac{(f-f_0)^2}{\beta^2}} \quad (54)$$

where $f_0 = 3.5$ Hz and $\beta = 35$ Hz. The average frequency, weighted by the signal intensity over the interval (f_1, f_2) is therefore given by

TABLE 4
FREQUENCY BANDS AND CORRESPONDING TIMES FOR FOUR
MARINELAND IMAGE FILES

<u>Image File</u>	<u>f_1 (Hz)</u>	<u>f_2 (Hz)</u>	<u>\bar{f} (Hz)</u>	<u>\bar{t} (sec)</u>
1	0	11.28	5.60	0.556
2	0	-11.28	-5.48	-0.544
3	5.64	16.92	11.15	1.107
4	-5.64	-16.92	-11.03	-1.095

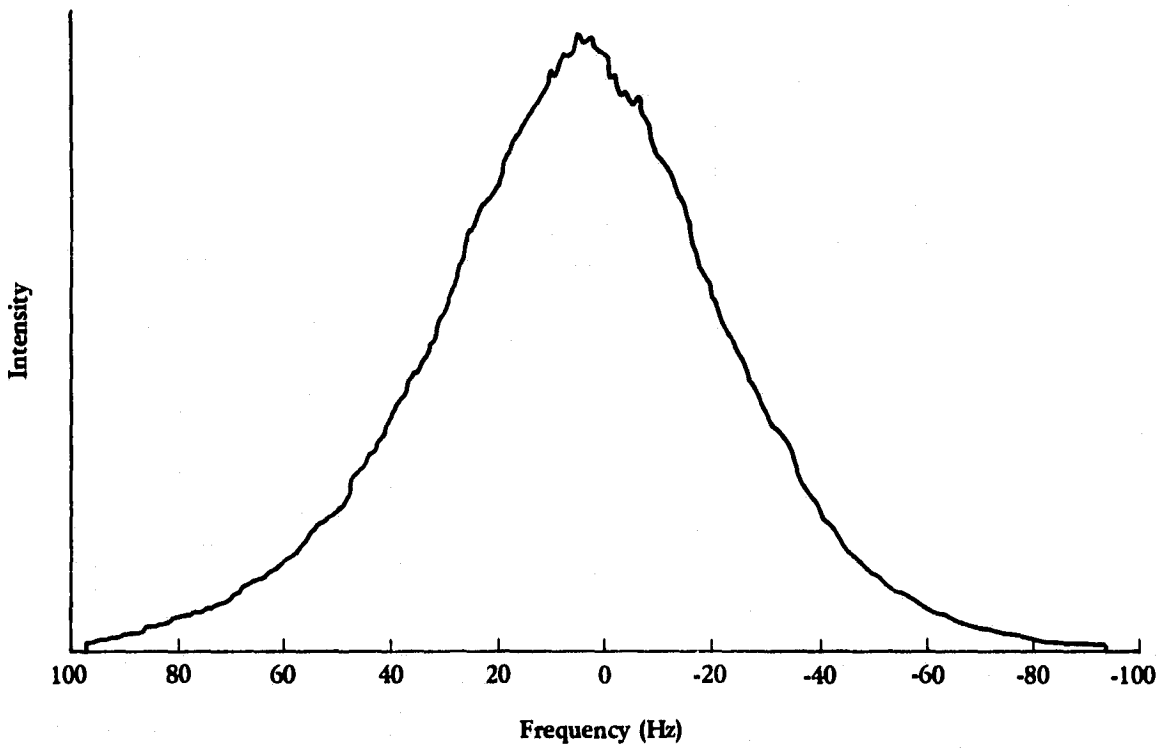


FIGURE 26. DOPPLER SPECTRUM FOR MARINELAND (PASS 2) L-BAND DATA.

$$\begin{aligned}
 \bar{f}_1 &= \frac{\int_{f_1}^{f_2} f A(f) df}{\int_{f_1}^{f_2} A(f) df} \\
 &= f_0 - \frac{\beta}{\sqrt{\pi}} \frac{\exp \left[-\left(\frac{f_1 - f_0}{\beta} \right)^2 \right] - \exp \left[-\left(\frac{f_2 - f_0}{\beta} \right)^2 \right]}{\operatorname{erf} \left(\frac{f_1 - f_0}{\beta} \right) - \operatorname{erf} \left(\frac{f_2 - f_0}{\beta} \right)} \quad (55)
 \end{aligned}$$

The average frequencies, and the corresponding average times were calculated for each image file from Eq. (50) for a range $R_0 = 6$ km and an aircraft speed $V = 83$ m/sec. The results are shown in Table 4. The effective time interval between Files 1 and 2 is 1.10 sec, and between Files 3 and 4 is 2.20 sec.

The shift in the position of the waves between Files 1 and 2, and between Files 3 and 4, was measured as follows. First, the two images in each pair were registered in the azimuthal direction by computing the cross-correlation function for the images over a land area. This analysis indicated that the maximum correlation was obtained when File 2 was shifted eight lines (in the azimuthal direction) relative to File 1, and when File 4 was shifted 14 lines relative to File 3. Next, a set of 200 corresponding azimuthal lines was selected from each file. In each subset, five azimuthal lines were averaged together (along the wave crests) to improve the signal-to-noise ratio, yielding a set of 40 smoothed azimuthal lines. A set of 256 range samples was selected from each smoothed azimuthal line and the cross correlation function was computed in the range direction.

The cross-correlation function was calculated both by direct computation and by Fourier transform methods. In the direct computation method, the correlation function is calculated as

$$\rho(i) = \frac{\sum_{j=1}^N S_1(j)S_2(j+i)}{\sigma_1\sigma_2} \quad (56)$$

where i and j represent range sample numbers, S_1 is the signal level in the first file, S_2 is the signal level in the second file, and σ_1 and σ_2 represent the standard deviations of the signals in Files 1 and 2, respectively. Using Fourier transform methods, the correlation function is given by

$$\rho(i) = \text{F.T.}^{-1} \left\{ \tilde{S}_1^*(j) \tilde{S}_2(j) \right\} / \sigma_1 \sigma_2 \quad (57)$$

where \tilde{S}_1^* is the complex conjugate of the Fourier transform of S_1 , \tilde{S}_2 is the Fourier transform of S_2 , and F.T.^{-1} indicates the inverse Fourier transform of the product of these two. In both cases, the mean signal is removed from S_1 and S_2 before the computation of the correlation function.

The correlation function calculated from a single line of data is an unreliable indication of the image shift because of noise in the data. The use of the Fourier transform method for calculating the correlation function allows some simple manipulations to be done to improve the quality of the results. Since it is the shift in the position of the dominant wave which is to be measured, it is desirable to suppress both the low-frequency signal variations and the high-frequency noise, leaving a range of wavelengths around the dominant wavelength. This is easily done by setting the Fourier coefficients to zero outside of this wavelength range.

The pixel spacing for this data set is 3 meters in range, which corresponds to a horizontal distance of 4.04 meters for an incidence angle of 48° . Thus, the dominant wavelength is approximately 20 pixels for the section of data considered (range samples 400-655). In the results presented here, the Fourier coefficients corresponding to wavelengths greater than 10 pixels and less than 40 pixels were set to zero. The correlation function was calculated for each of the 40 azimuth lines and averaged over this set. Figure 27 shows the resulting correlation function for image Files 1 and 2. There

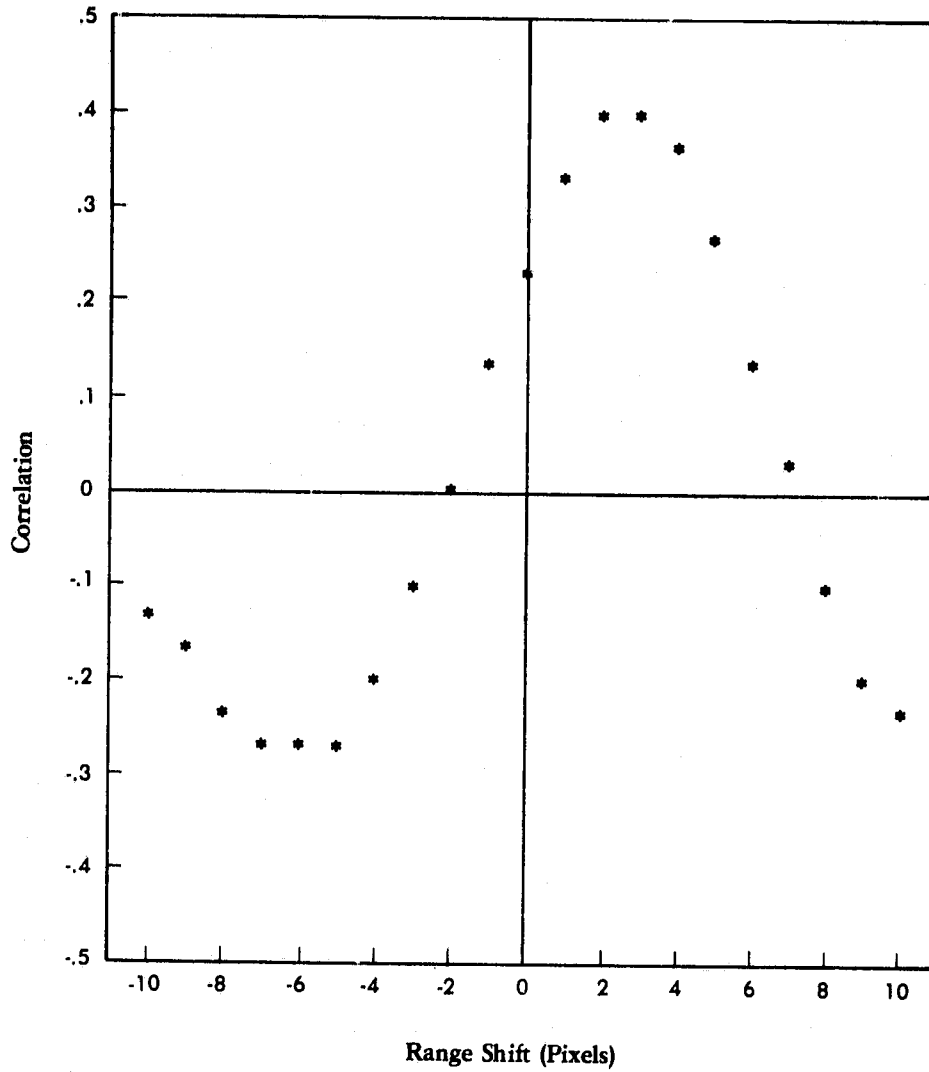


FIGURE 27. CORRELATION FUNCTION FOR MARINELAND IMAGE FILES 1 AND 2.

is a clear maximum at a shift of 2.5 pixels, which corresponds to a horizontal shift of 10.1 meters. Dividing this by the effective time difference of 1.1 seconds; one obtains a phase velocity of 9.2 m/sec. The correlation function for Files 3 and 4 (Figure 28) shows a maximum at six pixels which corresponds to a horizontal shift of 24.2 meters. Dividing this by 2.2 seconds yields a phase velocity of 11.0 m/sec. The latter measurement agrees well with the expected result for an 80-meter wavelength, while the former one is slightly smaller than the expected result. It should be noted that the zero crossings of the correlation function indicate a slightly smaller wavelength than 80 meters. The zero crossings occur at a displacement of $\lambda/4 = 18$ meters, which would imply a wavelength of about 72 meters and a deep-water phase velocity of 10.6 m/sec. In addition, shoaling of the waves may cause the actual phase velocity to be smaller than that calculated from the deep-water dispersion relation.

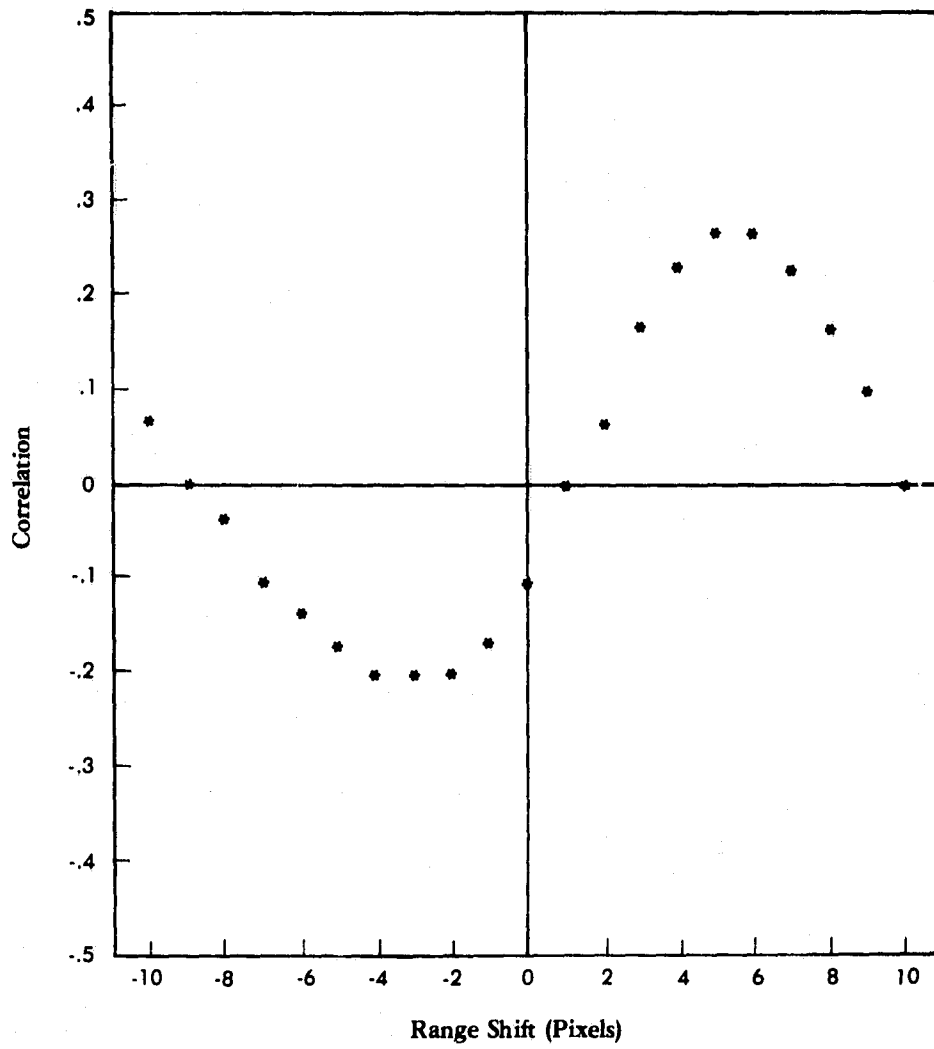


FIGURE 28. CORRELATION FUNCTION FOR MARINELAND IMAGE FILES 3 AND 4.

5
CONCLUSIONS AND RECOMMENDATIONS

Evidence has been presented in this report which demonstrates that synthetic aperture radar can potentially measure oceanic currents, orbital velocities and phase velocities. The evaluation to date using conventionally configured SAR systems has shown that there are significant errors in these measurements. However, none of these systems have been optimally configured for the purpose of measuring currents. Desirable system operating parameters for future SAR data collection efforts for the measurement of ocean currents should include consideration of:

1. Incidence Angle

From purely geometric considerations, it is desirable to have the incidence angle as large as possible in order to maximize the radial component of the velocity. However, the radar cross section becomes smaller as the incidence angle increases, so the geometric considerations may have to be balanced against signal/noise ratio considerations, particularly if the water surface is relatively smooth.

2. SAR Platform Velocity

Since the Doppler spectrum width is directly proportional to the SAR platform velocity, it is desirable to keep the velocity as low as possible.

3. Altitude

The altitude does not directly affect the width of the Doppler spectrum or the amount of the shift, so this is not a critical parameter. Stability of the platform is important, and the altitude for aircraft SAR's may indirectly affect that parameter, however.

4. Wavelength

The Doppler shift for a given radial velocity is inversely

proportional to the radar wavelength. Therefore, it is desirable to operate at shorter wavelengths to maximize the Doppler shift.

5. SAR Platform Heading

It would be useful to have at least two passes in orthogonal directions in order to resolve the current direction. One of the flight paths should be perpendicular to the current to maximize the radial component of the velocity. More than two passes would be desirable to reduce errors by averaging or to have a backup in case of data quality problems.

6. Antenna Gain Pattern

The use of image spatial resolution as the primary design criterion for a SAR system leads to a maximization of the antenna beamwidth. However, this limits the accuracy of the current measurement because the Doppler spectrum width is directly proportional to the antenna beamwidth. Therefore, if current measurement accuracy is included as a criterion in the design of a SAR system, a tradeoff is required. Alternatively, it may be possible to improve the current measurement accuracy while maintaining spatial resolution by introducing some structure into the antenna gain pattern. For example, a sharp "notch" could be created in the antenna pattern by introducing a phase delay over one half of the antenna. Also, the tradeoff between spatial resolution and current measurement accuracy may be improved by the use of advanced systems such as the spotlight technique discussed below.

Both aircraft and satellite SAR current measurements have been presented. The majority of the examples presented have utilized analog data. Basically, a SAR signal film has been used as the data source and lenses are employed to Fourier transform the data in order to extract the Doppler information. Recently, SAR digitally correlated data that retains phase (I and Q) information has been used

to evaluate SAR current detection. Digital data appears to be advantageous over analog data in that system effects are more easily correctable.

The measurement of surface currents by the Doppler analysis method described in this report is inherently harder using satellite data as opposed to aircraft data. This is primarily due to the higher velocity of satellite platforms, which causes the Doppler spectrum to be wider and hence the measurement of a given Doppler shift to be more difficult. In the case of Seasat, this problem is compounded by the longer wavelength and smaller incidence angle, which cause the Doppler shift for a given current to be smaller by an order of magnitude than that for X-band aircraft data. Thus, a current which would cause a Doppler shift equal to the spectrum width in an aircraft X-band SAR causes a shift of less than one percent of the spectrum width for Seasat. It should be noted, however, that a satellite platform is more stable than an aircraft platform and a one percent Doppler shift may indeed be measurable.

In view of the advantages offered by satellite platforms, it is recommended that studies be carried out to design a more optimal SAR system for measuring ocean currents from space. These studies should include an optimization of "conventional" SAR systems by the appropriate choice of the antenna pattern, wavelength, and incidence angle as discussed previously in this report. They should also include consideration of new SAR concepts including bistatic and angle-diversity techniques [Walker, 1980] for reducing the Doppler spectrum width and resolving the components of the current vector.

Angle-diversity SAR systems, utilizing the so-called spotlight technique, could provide radial line-of-sight measurements in two or more directions in order to resolve the components of the current vector. The spotlight technique uses a rotating antenna which "follows" a given target area on the surface, rather than a fixed antenna

orientation as in a conventional SAR. This allows the system to achieve a fine spatial resolution with a relatively narrow antenna beamwidth by collecting and processing data coherently over the required integration time. However, by choosing to process a shorter segment of the data, one can, in effect, narrow the Doppler spectrum and therefore increase the accuracy of the Doppler shift measurement. Thus, the system provides the flexibility of trading off spatial resolution for Doppler measurement accuracy during processing. In addition, it may be possible to devise special processing techniques which would allow accurate Doppler measurements to be made over an extended integration time, and thus preserve a high spatial resolution in the current measurement.

Bistatic SAR systems, utilizing separate transmit and receive platforms could also be used to narrow the Doppler spectrum, since the spectrum width in this case is proportional to the vector sum of the platform velocities. For example, two platforms moving in opposite directions produce a Doppler spectrum equivalent to that for a monostatic SAR with a velocity equal to the difference between the bistatic platform speeds. In both of these cases, tradeoffs must be made between spatial resolution and current velocity resolution, and a design study would be required to determine the constraints on the various system parameters.

In addition to investigating these new techniques, it is recommended that a review be made of previously developed SAR moving-target indication (MTI) techniques for their potential application to the problem of mapping ocean currents. These techniques include the use of delay lines for comparing subsequent pulses from the same antenna or from different antennas. The ocean current problem is somewhat different from the MTI problem in the sense that the motion of an extended surface area is involved, rather than the detection of a small moving target in a stationary background. Nevertheless, some of the techniques developed for MTI systems may be applicable to the problem of measuring ocean surface currents.

This report has also indicated the possibility of measuring gravity wave orbital and phase velocities under certain conditions. The evaluation of these methods has been limited by the small number of available aircraft data sets containing suitable gravity wave fields. The orbital velocity measurement using the Doppler broadening effect has potential applications to the measurement of wave heights, which is a topic of considerable oceanographic interest. A further evaluation of this technique and a study of its possible application to satellite data, as is the case of the current measurement, would appear to be warranted. The phase velocity measurement is of interest in verifying wave imaging models but has a smaller range of applications and is probably not suitable for use with satellite data.

REFERENCES

- Brown, W.M., "Synthetic Aperture Radar," IEEE Trans. Aerospace and Electronics Systems, AES-3, pp. 217-229, 1967.
- Cindrich, I., J. Marks, and A. Klooster, "Coherent Optical Processing of Synthetic Aperture Radar Data," Proc. SPIE, 128, 1977.
- Gonzalez, F.I., R.A. Shuchman, and C.L. Rufenach, "Ocean Surface Current Detection by Synthetic Aperture Radar," in Oceanography from Space, J. Gower (ed.), Proc. of the COSPAR/IUCRM Symp. on Oceanography from Space, Venice, Italy, Plenum Publishing Corp., NY, 1981.
- Gower, J.F.R. and B.A. Hughes, "Radar and Ship Observations of Coastal Sea Surface Roughness Patterns in the Gulf of Georgia," Proceedings of the 13th International Symposium on Remote Sensing of Environment, Ann Arbor, MI, pp. 103-115, 1979.
- Hayes, J.G. and R.A. Shuchman, "Seasat SAR Ocean Surface Current and Shallow Water Wave Refraction," Proceedings of the COSPAR/SCOR/IUCRM Symposium on Oceanography from Space (in Press), 1981.
- Keller, W.C. and J.W. Wright, "Microwave Scattering and Straining of Wind Generated Waves," Radio Sci., 10, pp. 139-147, 1975.
- Kozma, A., E.N. Leith, and N.G. Massey, "Tilted Plane Optical Processor," Applied Optics, 11, pp. 1766-1777, 1972.
- Raney, R.K., "Synthetic Aperture Imaging Radar and Moving Targets," IEEE Trans. Aerospace and Electronics Systems, AES-7, pp. 499-505, 1971.
- Shemdin, O.H., A. Jain, S.V. Hsiao, and L.W. Gatto, "Inlet Current Measured with Seasat-1 Synthetic Aperture Radar," Shore and Beach, Vol. 48, pp. 35-39, 1980.
- Shuchman, R.A., C.L. Rufenach, F.I. Gonzalez, and A. Klooster, "The Feasibility of Measurement of Ocean Surface Currents Using Synthetic Aperture Radar," Proceedings of the 13th International Symposium on Remote Sensing of Environment, Ann Arbor, MI, Vol. 1, pp. 93-102, 1979.
- Tyler, G.L., C.L. Teague, R.H. Stewart, A.M. Peterson, W.H. Munk, and J.W. Joy, "Wave Directional Spectra from Synthetic Aperture Observations of Radio Scatter," Deep Sea Res., 21, pp. 989-1016, 1974.
- Walker, J.L., "Range-Doppler Imaging of Rotating Objects," IEEE Trans. Aerospace and Electronics Systems, AES-16, pp. 23-52, 1980.

THE FEASIBILITY OF MEASUREMENT OF OCEAN SURFACE
CURRENTS USING SYNTHETIC APERTURE RADAR*

R. A. Shuchman

Environmental Research Institute of Michigan (ERIM)
Ann Arbor, Michigan

C. L. Rufenach

Wave Propagation Laboratory
Boulder, Colorado

F. I. Gonzalez

Pacific Marine Environmental Laboratory
Seattle, Washington

A. Klooster

Environmental Research Institute of Michigan (ERIM)
Ann Arbor, Michigan

ABSTRACT

Synthetic aperture radar (SAR) has potential for mapping ocean surface currents. This instrument responds primarily to backscatter from capillary waves, which, in conventional SAR processing, are assumed stationary. However, these scatterers are not stationary; they move with a velocity which is the resultant of their own phase velocity plus velocities due to the presence of currents and longer gravity waves. The radial (line of sight) component of this resultant velocity produces a Doppler shift in the temporal frequency of the return signal, which translates to a spatial frequency shift recorded on SAR signal film. The relative contributions to this shift by currents, gravity wave orbital motions, and capillary phase velocities are being studied by a theoretical model now under development.

The authors, using X- and L-band SAR data of near shore and Gulf Stream ocean surfaces, measured the Doppler shift of moving ocean scatterers relative to stationary scatterers. Currents deduced from these Doppler shift calculations (averaged over a 500 x 500 m² area) were found to be consistent with available sea truth gathered during the Marine-land Experiment. Additionally, SAR-SEASAT satellite data of the Columbia River, Oregon is being evaluated to assess the potential of using SAR to map ocean surface currents.

* The ERIM work reported herein is supported by NOAA Contract No. A01-78-00-4822.

1. INTRODUCTION

This paper discusses the potential use of Synthetic Aperture Radar (SAR) to measure surface currents on the ocean. The surface current velocity is measured by exploitation of the SAR Doppler signal history. Radial (line of sight) velocities of currents shift the Doppler signal history and it is this shift that is measured and exploited to obtain the horizontal current velocity.

Synthetic Aperture Radar is a specialized form of Side-Looking Airborne Radar (SLAR), it utilizes the Doppler history (change of phase) associated with the motion of the aircraft, recording both the phase and the amplitude of the backscattered energy, thus improving the along-track or azimuth resolution. The longer the radar data length, the greater the improvement in the along-track resolution of the system.

Synthetic Aperture Radar is a coherent airborne or spaceborne radar that uses the motion of a moderately broad physical antenna beam to synthesize a very narrow beam thus providing fine azimuthal (along-track) resolution (Brown and Porcello, 1969; Harger, 1970). Fine range (cross-track) resolution is achieved by transmitting either very short pulses or longer coded pulses which are compressed by matched-filtering techniques into equivalent short pulses. Usually, the coded pulse is a waveform linearly modulated in frequency.

Typically, the phase history of a scattering point in the scene is recorded on photographic film as an anamorphic (astigmatic) Fresnel zone plate. The parameters of the zone plate are set in the azimuth direction by the Doppler frequencies produced by the relative motion between the sensor and the point scatterer, and in the range direction by the structure of the transmitted pulses. The film image is a collection of superimposed zone plates representing the collection of point scatterers in the scene. This film is used by a coherent optical processor which focuses the anamorphic zone plates into the points which produced the micro-wave scatter of the scene (Kozma, et al, 1972).

The radial motion of an ocean current imaged by a SAR will produce an apparent tilt to the phase history as recorded on the signal film. In addition, the scatterer history will also shift across the signal film. Since the synthetic aperture technique utilizes the small range rates of stationary reflecting objects to separate their images in the azimuth coordinate, targets moving in the range direction appear with altered azimuth positions in the processed image, but are still focused. A non-moving target will produce zero Doppler when it is on a line perpendicular to the aircraft track. However, if the reflecting object is moving toward the aircraft, zero Doppler will be produced after the aircraft has passes this perpendicular line, shifting the apparent position of the object in the same direction as the flight direction. Conversely, if the object is moving away from the aircraft, the apparent position will be shifted opposite the flight direction. To illustrate the displacement effects which can result from target motion in the range direction, observe Figure 1 which shows a SAR image of a moving railroad train displaced from its track. This displacement occurs because the radial component of its velocity produced radar echo phase rates that are different than the phase rate from the fixed targets. The magnitude of the azimuth displacement can be expressed as:

$$\Delta X = \frac{V_R}{V_A} R_s \quad (1)$$

where ΔX = displacement,
 V_R = line-of-sight velocity component of reflecting object,
 V_A = velocity of the radar aircraft,
 R_s = radar range of the reflecting object.

Note that image displacement is directly proportional to object radial velocity and radar range. It is inversely proportional to aircraft velocity and independent of radar wavelength.

The principle in imaging any surface with a radar is that the backscattered microwave energy (echo) received by the radar receiver contains information on the roughness characteristics (shapes, dimensions, and orientations) of the reflecting area. The principal reflectivity mechanism of a SAR imaging an ocean area is via the capillary wave structure. The SAR reflectivity estimate provides an apparent brightness that approaches the Bragg-Rice-Philips upper bound (Shuchman, et al, 1978). It is therefore necessary to have capillary wave structure present before one can attempt to measure current velocities. Additionally, the radar observes coherently the projection of $\vec{V}_C = \vec{V}_{\text{currents}} + \vec{V}_{\text{capillaries}} + \vec{V}_{\text{wave}}$ orbital motions onto the slant range vector. The projection of \vec{V}_C is V_r , the coherently sensible range velocity which Doppler modulates the SAR signal (Raney and Shuchman, 1978).

2. THEORY

The Doppler frequency shift for a moving target relative to a stationary target in a SAR system is

$$\Delta f_D = \frac{2V_r}{\lambda} \quad (2)$$

where V_r = radial component of target velocity, and λ = transmitted radar wavelength.

This temporal frequency shift will produce an azimuth spatial frequency shift of

$$\Delta f' = \frac{\Delta f_D P}{V_{AC}} \quad (3)$$

on the SAR signal film,
where P = azimuth packing factor, and
 V_{AC} = aircraft velocity.

Equations 2 and 3 can be combined to relate radial target velocity to Doppler spectrum shift:

$$V_r = \frac{\Delta f' \lambda V_{AC}}{2P} \quad (4)$$

This relationship can be used to measure the average radial velocity component of an ocean-wave scattering field relative to a fixed-land scattering field. A shift in the azimuth spatial frequency spectrum between fixed-land and moving-ocean surfaces yields an estimate for $\Delta f'$. Variations in spectrum locations due to antenna pointing may be eliminated by choosing imagery having land and ocean imaged simultaneously.

3. EXPERIMENTAL TECHNIQUE

The optical processing configuration used to make the measurements is shown in Figure 2. A scanning photomultiplier was used at the output of the optical processor to record the azimuth spectrum profile shown in the figure. Note in the figure that an image-plane aperture corresponding to an ocean area of 1 km x

1 km was used in this experiment. Measurements were also made using apertures (ocean areas) of 0.5 x 0.5 and 0.25 x 0.25 km. These measurements indicated that, although the azimuth Doppler scans become noisy as smaller ocean areas are used, acceptable scans can be obtained using an aperture corresponding to 0.25 x 0.25 km in radar space. Additionally, the SEASAT measurements to be discussed were made with a 3 x 3 km aperture.

Figure 3 presents the X-band (3.2 cm) azimuth profiles for 1 km x 1 km land and ocean areas imaged on Pass 3 at Marineland on 14 December 1975 (Shemdin, et al, 1978). Both areas were centered 6.8 km from the end of the pass. The land area was near nadir and the sea area was just inside the 60° incidence angle bounce line. As the figure indicates, the Doppler shift is to the left with respect to the land, thus indicating that the radial motion sensed is toward the radar (see bottom of Figure 2). The mid-point of a line across the 3 dB points of each spectrum was plotted for each scan. The separation of the mid-points was approximately 1.55 divisions. This separation indicated a shift of ~8 line-pairs/mm (1 div. = 5.2 lp/mm) between the two scans. Using this value for $\Delta f'$ in Eq. (4) yields

$$V_r = \frac{\Delta f' \lambda V_{AC}}{2P} = \frac{8 \times 10^3 (0.032) (76 \text{ m/sec})}{2(13,327)} = 0.75 \text{ m/sec} \quad (5)$$

Figure 4 presents the X-band azimuth profile for Pass 7 (180° heading with respect to Pass 3). Note that the spectrum has shifted an amount approximately equal but in an opposite direction to that of Pass 3.

Figure 5 is an L-band (23.5 cm) example of a near-shore scan showing that L-band can also be used to detect radial motion. The shift distance is not as great as for X-band. However, similar velocities can be measured. Recall that Eq. (4) is a function of radar wavelength (λ) and azimuth scaling factor (P). It should be noted that, since the shift for a given velocity is larger on the azimuthal Doppler scans for X-band than for L-band, the X-band scans are potentially more accurate, due to the larger scale in comparing stationary and moving Doppler scans.

4. EXPERIMENTAL RESULTS

A series of motion scans of near-shore surface currents were made at L-band and X-band. Additionally, motion scans of the Gulf Stream were also made at X-band only.

Figure 6 is a graph of the L-band near-shore measurements per pass vs. the spectrum shift from the DC reference (see Figure 5). In the figure, the letter "L" represents land or stationary scans while S and D represent wave scans made from data collected in shallow and deep water, respectively. Although this data indicated spectrum shifts from stationary to moving targets, the data was disappointing, in that neither the land measurements (L) nor the ocean data clustered. This rather disappointing result was felt to be caused by the operation of ERIM's L-band radar at Marineland* rather than an inherent limitation of SAR in sensing currents.

Alternatively, Figure 7 presents X-band spectrum shifts as a function of the three passes. The X-band results were encouraging, in the sense that stationary and moving Doppler scans clustered and Passes 3 and 7 (180° with respect to each other) shifted in opposite directions. Note that Pass 1 showed no azimuthal shift induced by velocity. This confirms the limited surface-current truth provided by CERC (Army Corps of Engineers). The CERC data indicated that an 85 cm/sec current existed on 14 December at Marineland, with a direction of travel toward shore.

* For a description of the ERIM X-L SAR system see Rawson, et al (1975).

X-band data from the Gulf Stream was also evaluated. Scans A-H (locations shown in Figure 8) were made using a 1 x 1 km aperture. Figure 9 compares azimuth scans of location A and location G. A graph plotting the location of the scans on the Gulf Stream data versus Δf from the DC reference is shown in Figure 10. If the average Δf between the Gulf Stream and non-Gulf Stream data is calculated using Eq. (4), a radial velocity (V_r) of 0.63 m/sec results. The direction of this velocity is determined by examination of Figures 8 and 9. Unfortunately, gravity-wave components were present during data collection. These waves were traveling in the same general direction as the Gulf Stream. Thus, there is some question as to whether the velocity sensed by the SAR could be an orbital velocity wave component. The authors do not believe this to be the case, however, because deep-water waves were measured both in the Gulf Stream and out of it; thus, any orbital motion effect from the gravity waves was the same on each side of the Gulf Stream boundary.

5. SEASAT CONSIDERATIONS

NASA launched in June 1978, an oceanographic satellite called SEASAT. One of the five sensors on board the satellite was a SAR. This SAR, which imaged the ocean at a range of 850 km produced imagery 100 km wide by up to 4000 km in length. The incident angle of the SEASAT SAR is nominally 20°. The resolution obtainable is 8 m azimuth by 25 m ground range.

SEASAT data collected between June and October 1978* is being evaluated by the authors in respect to its ability to measure surface currents. Data from Revolution 150 (July 7, 1978) is being evaluated in detail. In particular, Revolution 150 imaged the Columbia River, Oregon. Figure 11 shows the resulting SEASAT imagery. The image represents subswath 2, its resolution is on the order of 10 m azimuth, 25 m ground range. The scale factor is nominally 1:215,000, thus the image represents an area of ~52 x 35 km.

This image offers the advantage of attempting to calculate the velocity of the Columbia River (reported to be 2.5-3.0 m/sec at the time of flight) by either the use of Eq. (1) or the Doppler centroid method. A 3 m/sec velocity using Eq. (1) would result in a displacement of 115 meters. This corresponds to shift of approximately 0.5 mm on the image, a distance too small to accurately discern.

The Doppler method was also used in an attempt to measure the velocity of the Columbia River. Four land scans were compared to four Columbia River scans (different areas). The four data values resulting from the four pairs of measurements produced a horizontal velocity of 4.8 m/sec. This value is somewhat higher than the reported 2.5-3.0 m/sec velocity. All SEASAT measurements of the currents area to date appear to have higher than reported velocities. The cause for this apparent bias is not well understood at present.

6. SUMMARY

The above described technique utilizes the measurement of Doppler shifts in the SAR signal history induced by radial velocities. Thus oceanic surface currents to be measured must be traveling perpendicular to the SAR flight track. Additionally, because a radial velocity is sensed (line-of-sight) the measurements must be corrected to the horizontal datum plane. This is done knowing the SAR geometry.

Azimuth traveling currents can theoretically be measured by observing defocusing effects in the SAR signal processor (Shuchman and Zelenka, 1978). However, the authors believe the defocusing effects are too subtle to be accurately measured.

Surface currents are inherently harder to measure using satellite data as opposed to aircraft. This is due to the increased Doppler bandwidth of the satellite in respect to aircraft. For example, the aircraft Doppler bandwidth at Marineland is approximately 100 Hz, while SEASAT's is approximately 1000 Hz.

* On October 10, 1978 SEASAT suffered a catastrophic power loss.

A 1.5 m/sec radial velocity produces a Doppler shift of approximately 10 Hz thus a shift measurement for the aircraft is a 10% change while for the satellite the change is 1%. It should be noted, however, that the satellite platform is more stable than an aircraft's and a 1% measurement may indeed be measurable.

The effect of a gravity wave field on a current area to be measured has not been studied in detail to date. Initial observations indicate the wave motion causes a symmetrical broadening of the Doppler history and therefore does not alter the shift induced by the current.

In conclusion, the current measurements presented herein appear consistent, in the sense that Doppler shifts were detected and the shifts appear in the proper direction. However, the limited sea truth available for Marineland prevents a definitive statement as to the ultimate feasibility of using SAR to sense current motion. Additionally, high velocity current data has been collected off Vancouver Island, which is a physical situation very different from the large area, low velocity situation of Marineland. This data will be analyzed in the near future. The SEASAT measurements need further theoretical consideration to explain the overly large Doppler shift in the Columbia River bar example.

REFERENCES

- Brown, W. M. and L. J. Porcello, 1969. "An Introduction to Synthetic Aperture Radar," IEEE Spectrum, 6, pp. 57-62.
- Harger, R. O., 1970. Synthetic Aperture Radar Systems, Academic Press, New York
- Kozma, A., E. N. Leith, and N. G. Massey, 1972. "Tilted Plane Optical Processor," Applied Optics, 11, p. 1766.
- Raney, R. K. and R. A. Shuchman, 1978. "SAR Mechanism for Imaging Waves," Proc. of Fifth Canadian Symposium on Remote Sensing, Victoria, B. C.
- Rawson, R., F. Smith, and R. Larson, 1975. "The ERIM X- and L-Band Dual Polarized Radar," IEEE 1975 International Radar Conference, New York, p. 505.
- Shemdin, O. H., W. E. Brown, Jr., F. G. Staudhammer, R. Shuchman, R. Rawson, J. Zelenka, D. B. Ross, W. McLeish, and R. A. Berles, 1978. "Comparison of In-Situ and Remotely Sensed Ocean Waves off Marineland, Florida," Boundary Layer Meteorology, 13, pp. 225-234.
- Shuchman, R. A., A. Klooster, and A. L. Maffett, 1978. "SAR Mechanism for Imaging Ocean Waves," Proc. EASTCON '78 Record, IEEE Electronics and Aerospace Systems Convention.
- Shuchman, R. A. and J. S. Zelenka, 1978. "Processing of Ocean Wave Data from a Synthetic Aperture Radar, Boundary Layer Meteorology, 13.

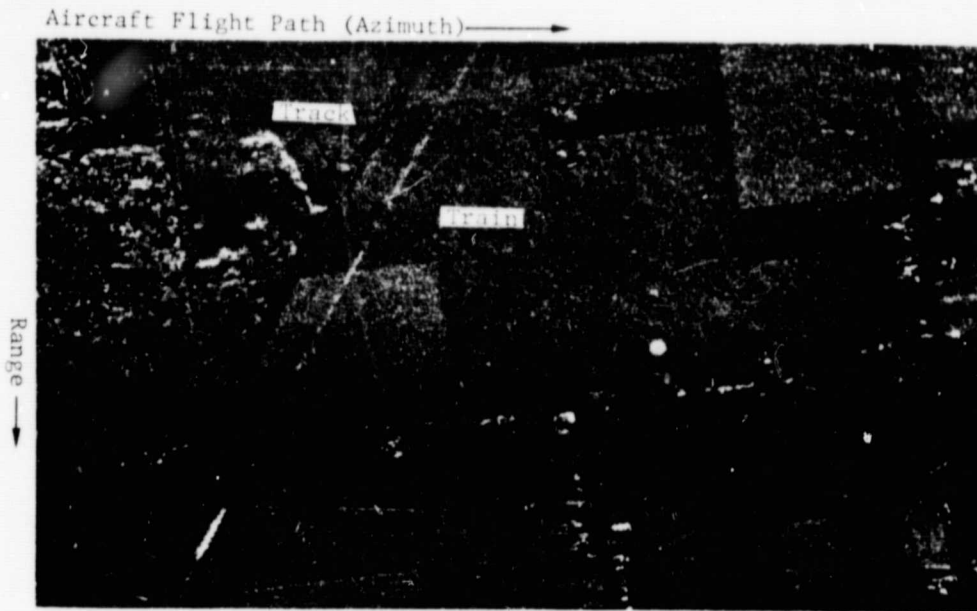


Figure 1. Moving Train Displaced from Track

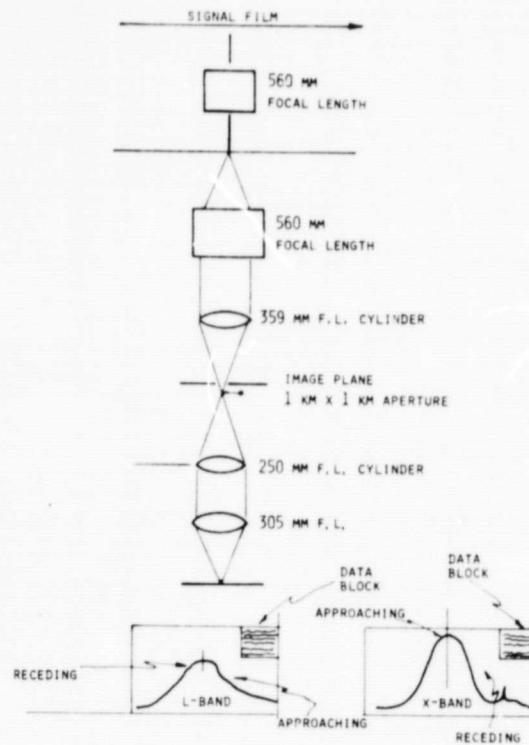


Figure 2. Optical Configuration Utilized to Make Azimuth Frequency Scans

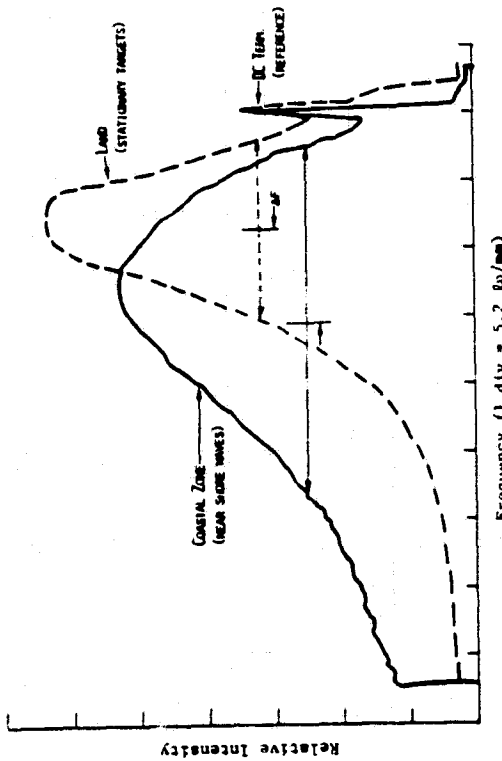


Figure 3. X-Band Azimuthal Doppler Frequency Scans for Pass 3, 14 December 1975

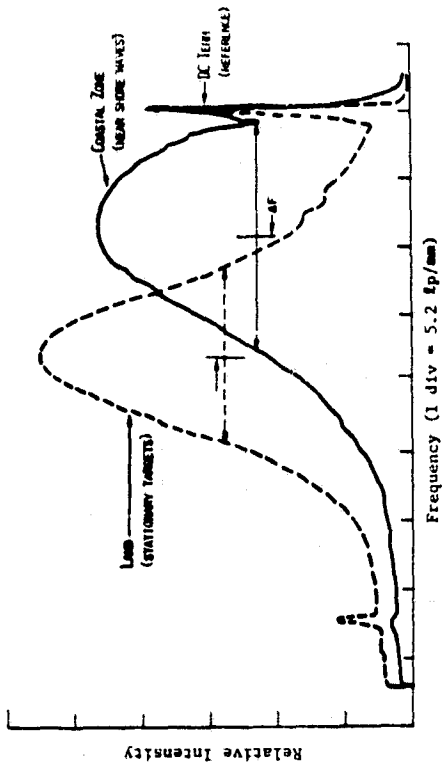


Figure 4. X-Band Azimuthal Doppler Frequency Scans for Pass 7, 14 December 1975

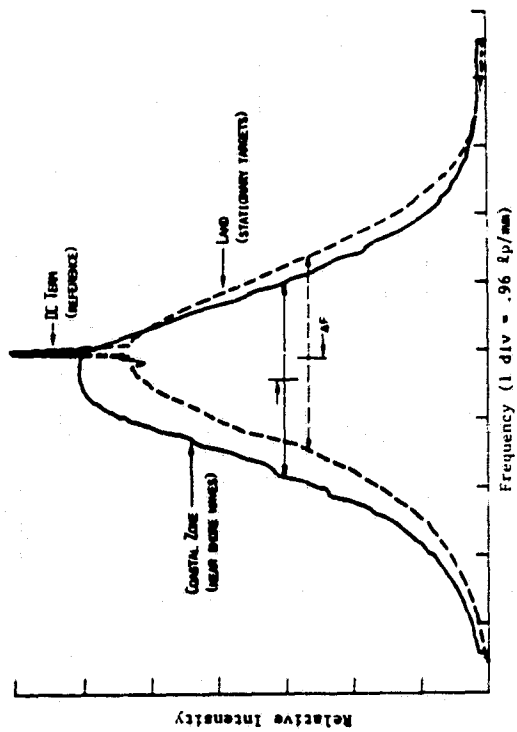


Figure 5. L-Band Azimuthal Doppler Frequency Scan, 14 December 1975

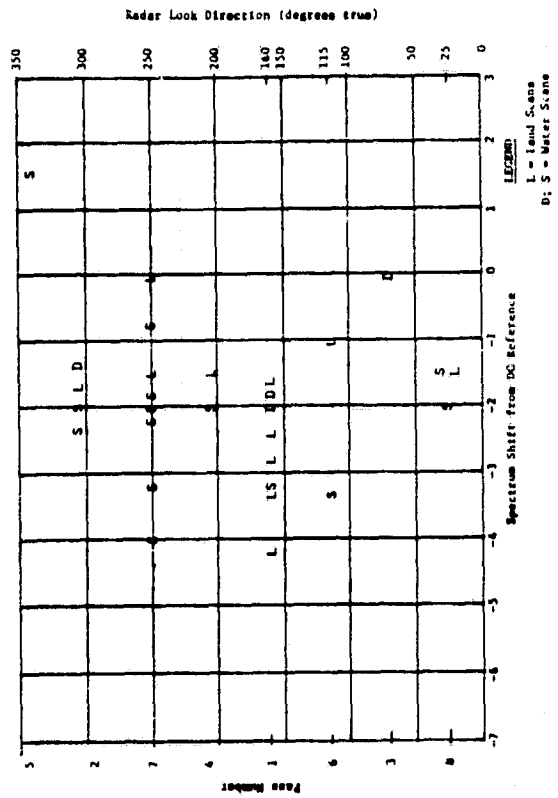


Figure 6. L-Band Spectrum Shift as a Function of Pass.

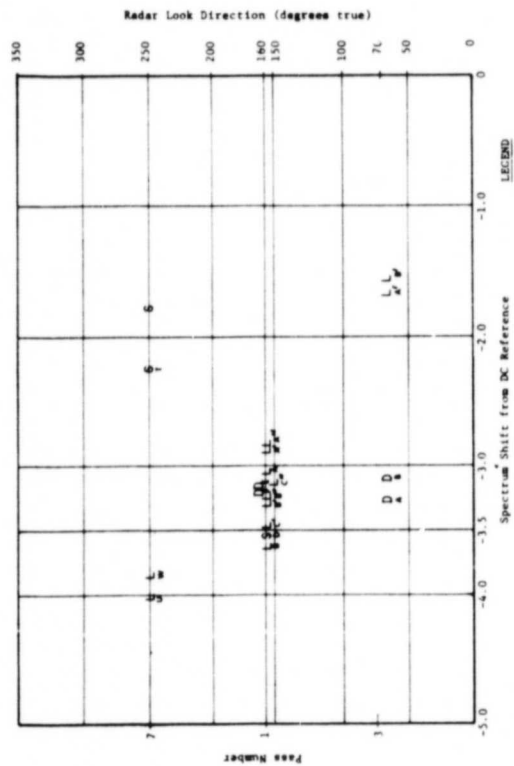


Figure 7. X-Band Spectrum Shift as a Function of Pass

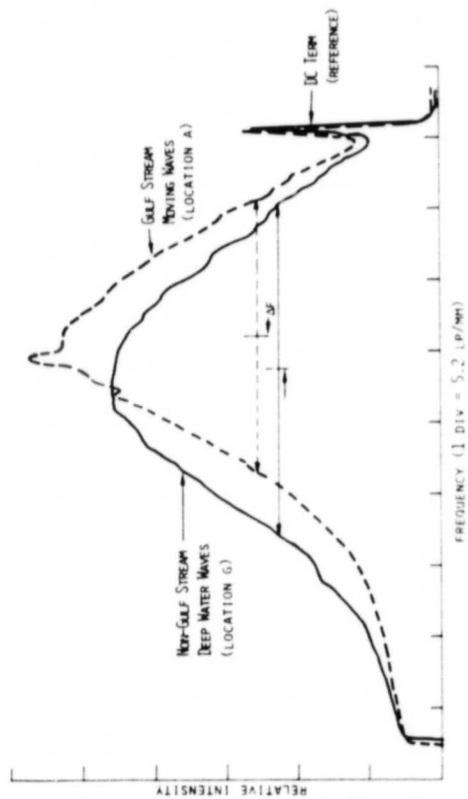


Figure 9. Azimuthal Scans of Gulf Stream and Non-Gulf Stream Ocean Areas

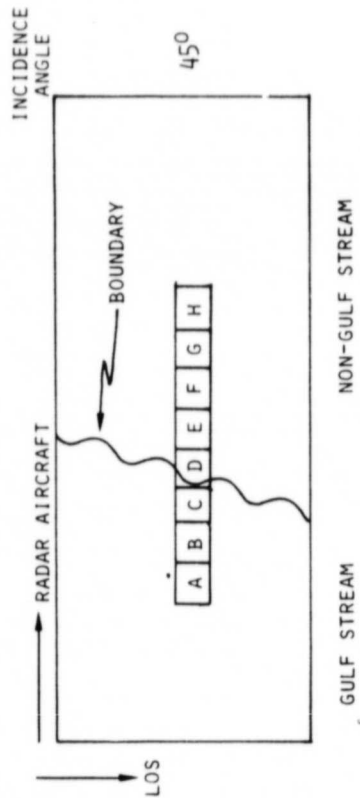


Figure 8. Location of X-Band Gulf Stream Azimuth Velocity Scans

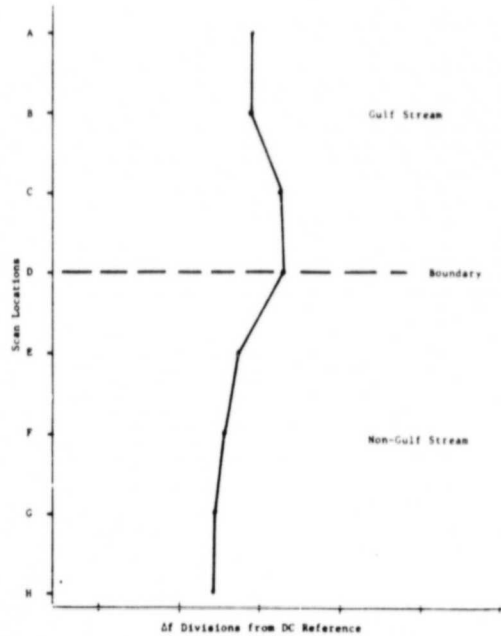


Figure 10. Scan Location Vs. Δf Divisions from DC Reference

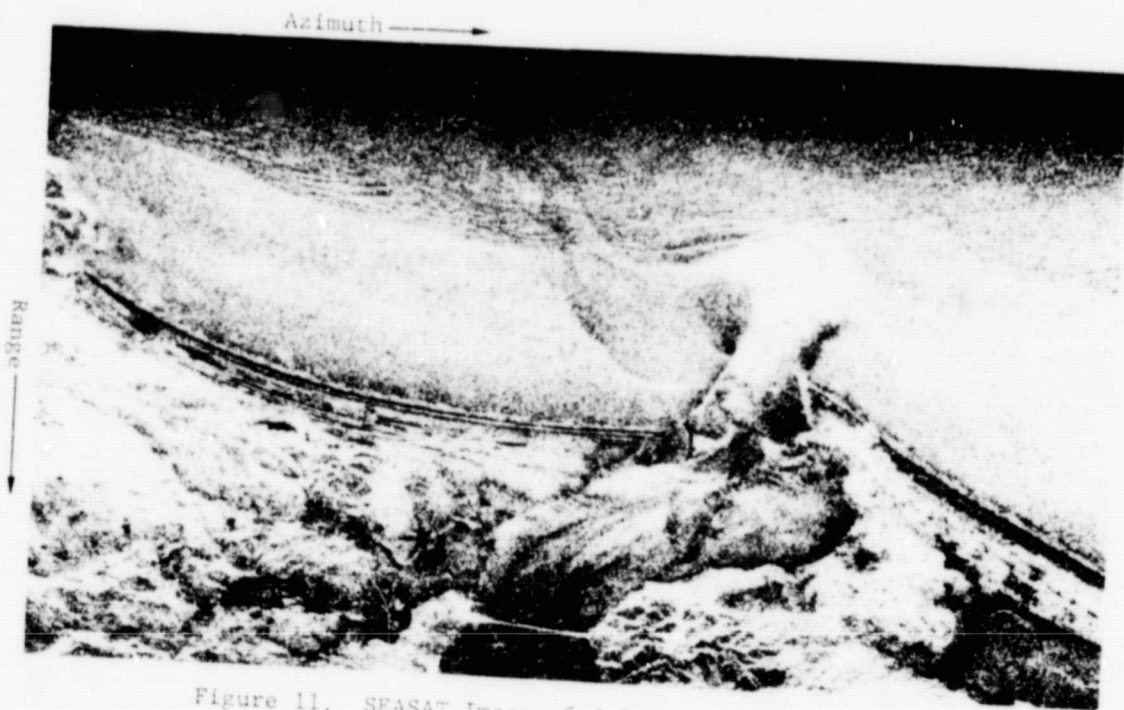


Figure 11. SEASAT Image of Columbia River Bar

OCEAN SURFACE CURRENT DETECTION BY SYNTHETIC APERTURE RADAR

F.I. Gonzalez
National Oceanic and Atmospheric Administration
Pacific Marine Environmental Laboratory
Seattle, Washington, 98105 U.S.A.

C.L. Rufenach
National Oceanic and Atmospheric Administration
Wave Propagation Laboratory
Boulder, Colorado, 80302 U.S.A.

R.A. Shuchman
Environmental Research Institute of Michigan
Radar and Optics Division
Ann Arbor, Michigan, 48107 U.S.A.

1. ABSTRACT

Synthetic aperture radar Doppler histories have been used to obtain estimates of ocean surface currents. For currents in excess of 1 meter/second, airborne radar measurements agree with surface observations to within 25 percent. Satellite measurements, however, yield current speeds far in excess of surface estimates. The technique developed to obtain the Doppler information is described, and possible sources of error are discussed.

2. INTRODUCTION

This paper discusses the potential use of synthetic aperture radar (SAR) to measure ocean surface currents. SAR systems are characterized by an azimuth (along-track) resolution comparable to that in the range (cross-track) coordinate. The azimuth resolution is achieved by using the Doppler history associated with the platform motion to synthesize an antenna (aperture) many times longer than the physical antenna; this in turn produces a correspondingly reduced effective radar beam width. In effect, the Doppler information is employed to locate targets in the azimuth coordinate.

The Doppler shift is positive as the platform approaches the target, zero as the target is directly abeam, and negative as the target recedes.

However, such processing assumes stationary targets, and in the case of ocean SAR imagery this assumption does not hold true. Rather, the primary radar scatterers are short gravity and capillary waves whose net velocity is the vector sum of their own phase velocity, the spatially and temporally periodic orbital velocities of longer gravity waves on which they may be borne, and the larger scale, more uniform velocity of any surface currents which may be present (Shuchman et al, 1978). The radial component of this resultant velocity vector (i.e. its projection along the radar line of sight) will induce an additional Doppler shift in the radar return signal. In principal, this additional shift should be detectable by comparison with the Doppler history of stationary targets.

3. THEORY

SAR Doppler frequency shifts for moving targets relative to stationary targets are given by Shuchman et al (1979)

$$\Delta f_D = \frac{2v_r}{\lambda} \quad (1)$$

where

v_r = radial component of target velocity
 λ = transmitted radar wavelength

This temporal frequency shift will produce in turn an azimuth spatial frequency shift on the SAR signal film given by

$$\Delta f' = \frac{\Delta f_D P}{V} \quad (2)$$

where

$P = \frac{V}{v_f}$ = the azimuth packing factor
 V = platform speed
 v_f = recording film speed

Combining Equations (1) and (2) yields an expression which can be used to estimate the average radial velocity component of an oceanic scattering field

$$v_r = \frac{\Delta f' \lambda V}{2P} \quad (3)$$

The required estimate of $\Delta f'$ can be obtained by the experimental technique described in the next section.

In conventional SAR processing, the target induced Doppler shift causes a corresponding shift of the apparent azimuth position of the target in the image; thus, target movement toward the radar will induce positive Doppler, and the target will appear to be farther ahead of the platform than it really is. Direct measurement of these azimuth displacements may yield estimates of surface currents, especially in regions of very high shear (Shemdin et al, 1980). For a target at range R, the magnitude of this azimuth displacement is given by

$$\Delta x = \frac{v}{V} r R \quad (4)$$

Note that this displacement is directly proportional to target velocity and range, but inversely proportional to platform velocity and independent of radar wavelength.

4. EXPERIMENTAL TECHNIQUE

The optical processing configuration used to make the Doppler measurements is shown in Figure 1. A scanning photomultiplier was used at the output of the optical processor to record the azimuth spectrum profiles such as those shown in the Figure. The estimate for $\Delta f'$ in Equation (3) is obtained from the difference in peak frequency for scans corresponding to land and ocean imagery. Errors in the location of each peak due to antenna pointing can be eliminated by comparing land and ocean data obtained simultaneously, i.e. having identical azimuth coordinate. Note in the Figure that an image-plane aperture corresponding to an ocean area of 1 km x 1 km is indicated. Aircraft measurements were also made using apertures (ocean areas) of 1.0 x 1.0, 1.0 x 0.5, 0.5 x 0.5, 0.5 x 0.25 and 0.25 x 0.25 km². These measurements indicated that, although the azimuth Doppler scans become noisier as smaller ocean areas are used, acceptable aircraft scans can be performed using an aperture corresponding to 0.25 x 0.25 km² in radar space. The SEASAT measurements to be discussed were made with a 3 x 3 km² aperture.

5. RESULTS

5.1 Aircraft

In July of 1978, several flights were made in the Straits of Georgia in the west coast of Canada, by the Canadian CV-580 research aircraft equipped with the ERIM dual polarized X- and L-band SAR (Rawson et al, 1975). The site selection for the experiment was an attempt to maximize the ocean surface current signal and minimize complications due to the presence of gravity waves. Narrow channels

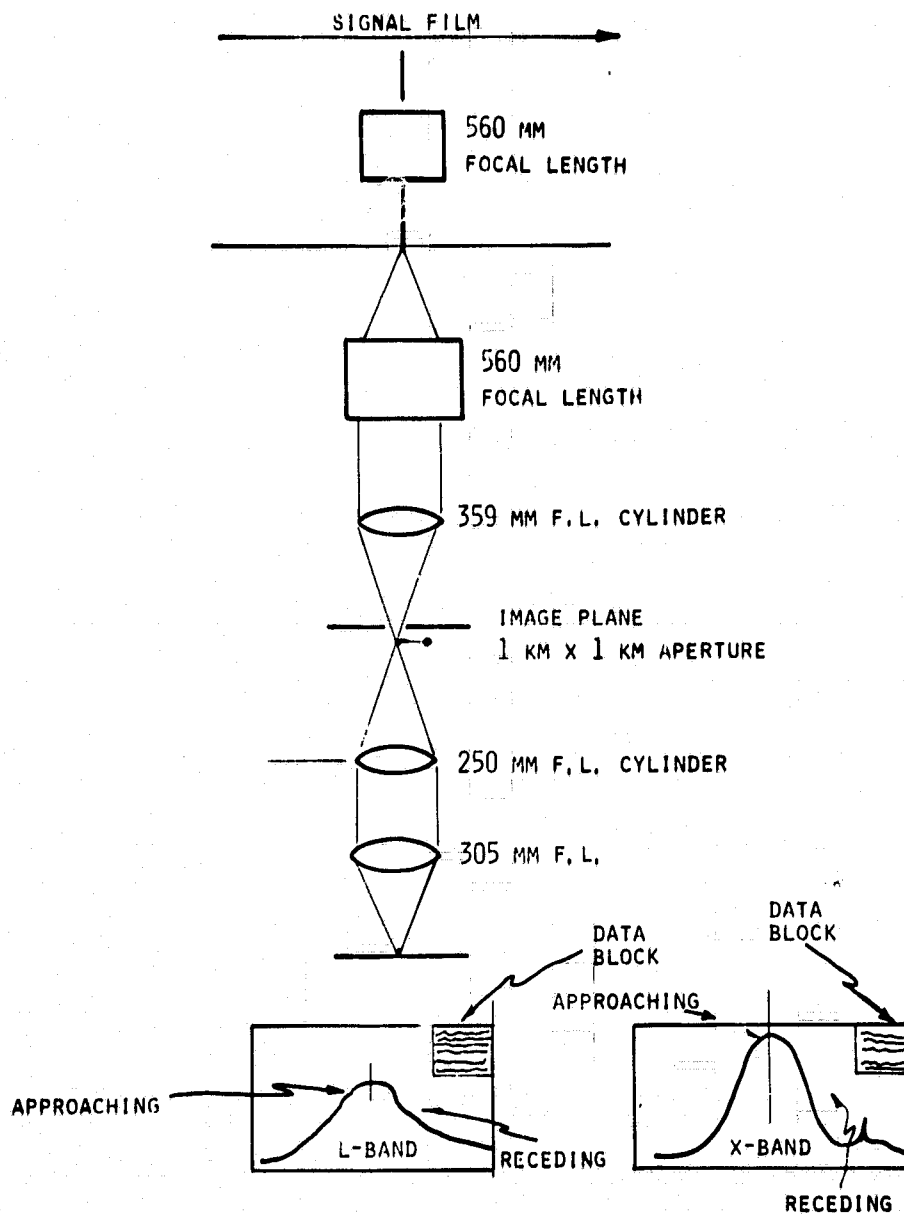


Fig. 1: Optical processing configuration for azimuth Doppler frequency scans.

in this region, such as Active Pass and Porlier Pass, are protected from Pacific Ocean waves by Vancouver Island, and are characterized by peak tidal currents commonly in excess of 2 meters/second.

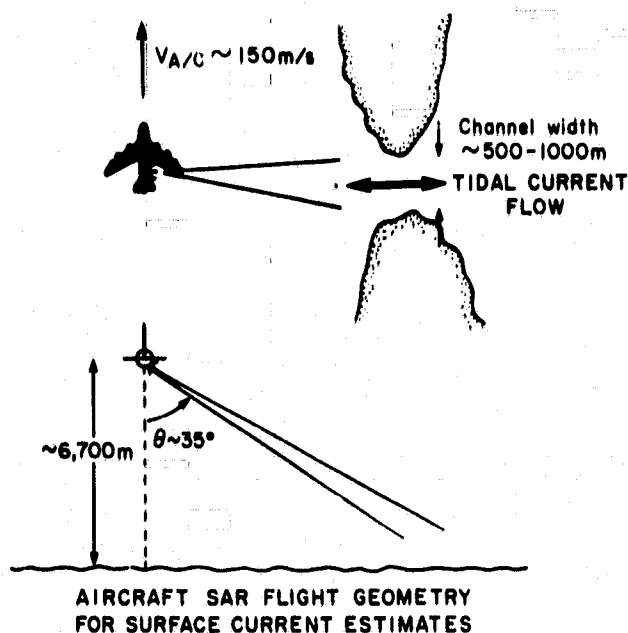


Fig. 2: Aircraft flight geometry for SAR-derived current estimates.

Figure 2 shows the SAR aircraft flight geometry for the X-band surface current estimates. Figure 3 is a sketch which indicates the resulting velocity measurements obtained for Porlier pass. Note that eight scans were made of (stationary) land to compare to (non-stationary) water. All surface current estimates by SAR are compared with surface observations in Figure 4. In all cases, the aircraft SAR correctly sensed the direction of the current but underestimated the magnitude. This bias may be the result of comparing spatially averaged SAR estimates with relatively higher point measurements obtained in situ near the center of each channel.

5.2 SEASAT

SEASAT, an experimental oceanographic satellite, was launched in June 1978. One of the five sensors on board was an L-band SAR, which imaged the ocean at a range of 850 km and incident angle of about 20° , producing imagery 100 km wide by up to 4000 km in length, and an obtainable resolution of 8 m azimuth by 25 m ground range (1 look). A SAR image of the Columbia River obtained 7 July 1978, and one of the English Channel obtained 19 August 1978 will be examined here.

The Columbia River image is shown in Figure 5. The resolution is approximately 10 m in azimuth and 25 m in ground range. The scale

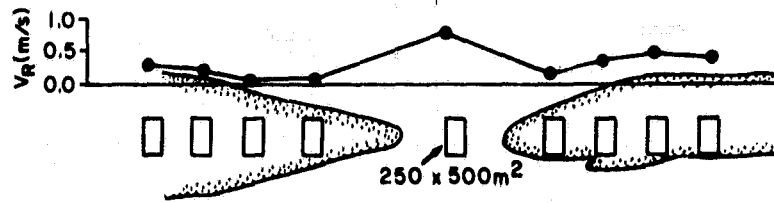
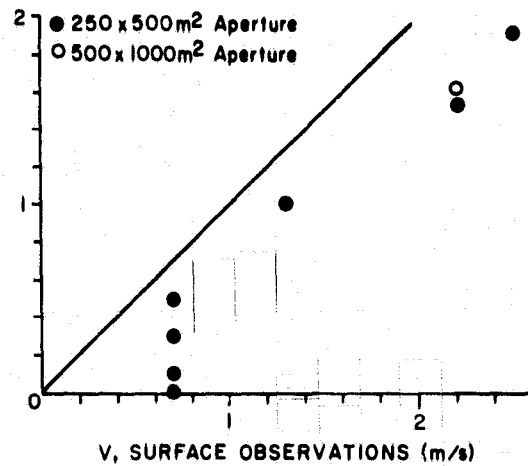


Fig. 3: SAR-derived surface current estimates for Porlier Pass. (Radial velocities deduced from airborne X-band SAR.)



Location	Surface Observation	A/C SAR Observation	E=Ebb F=Flood
Active Pass	.7E	0E	
	.7E	.1E	
	.7E	.5E	
	.7E	.4E	
Porlier Pass	1.3E	1.0E	
	2.2F	1.6F	
Active Pass	2.2F	1.7F	
	2.5F	1.9F	

Fig. 4: SAR-derived surface current estimates for Active and Porlier Pass compared with in situ observations.

factor of the original imagery is nominally 1:215,000, and represents an area of about $52 \times 35 \text{ km}^2$. Tide table predictions indicate that the current at the mouth of the Columbia River was oriented approximately perpendicular to the satellite track, with a speed of about 2.5 - 3.0 m/sec at the time of image acquisition.

The radial component of a 3 m/sec velocity vector perpendicular to the SEASAT track is about 1 m/sec. For this value of v_r , Equation (4) predicts an azimuth displacement of about 115 meters for a moving



Fig. 5: SEASAT SAR image of the Columbia River entrance.

target; this corresponds to a distance of about .5 mm on the original imagery. For a point-like moving target, such as a surface vessel, the velocity distribution of the scene is discontinuous and the associated displacement is detectable. In contrast, ocean currents are typified by smooth, continuous velocity distributions, and the "targets" are patches of ocean water with spatially varying average radial velocities. It is unclear at the present time what the final radar signature would be as a result of such velocity distributions, and more work is needed to develop these ideas as a potential technique for surface current estimation.

The Doppler method was used in an attempt to measure the velocity of three sections of the Columbia River (Figure 6). The three measured areas produced radial velocities of 1.5, 4, and 5.5 m/sec. The latter pair of values, when translated to the horizontal, are much higher than the reported 2.5 - 3.0 m/sec velocity. The cause of these large overestimates is being investigated.

The image of the English Channel shown in Figure 7 was acquired at a time corresponding to a predicted tidal current with a component perpendicular to the SEASAT track of 0.5 to 1.5 knots. The prominent linear features which appear in the Channel apparently represent surface manifestations of Channel bottom topography, as they correlate well with submerged sand waves which appear on local bathymetric charts (Alpers, in prepn.). To investigate the possibility that such features in the SAR imagery are induced by the surface current velocity distribution, scans were made across the imagery to measure both relative image intensities and Doppler shifts.

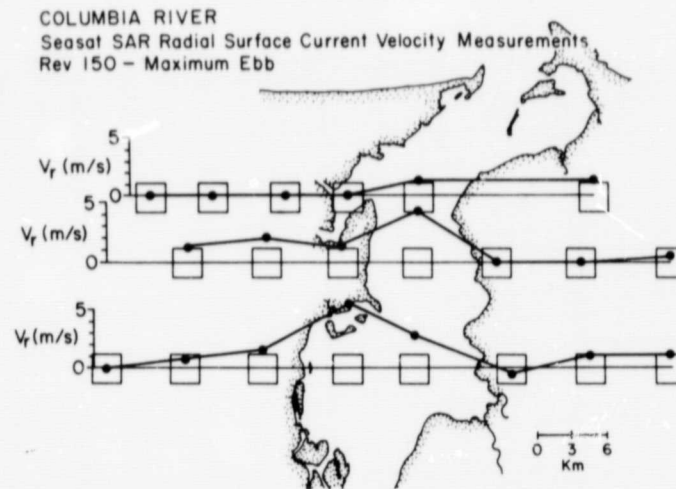


Fig. 6: SAR-derived surface current estimates for the Columbia River.



Fig. 7: SEASAT SAR image of the Thames Estuary and English Channel between Clacton and Calais. (Orbit 762)

The results are shown in Figure 8. There does appear to be significant correlation among the linear bathymetric features (as indicated by the intensity scan) and the surface current distribution (as implied by the Doppler shift scan).

6. DISCUSSION

The ocean current measurement techniques we have described here yield only a single component of the current. Thus, measurements must be made from at least two different viewing angles (preferably differing by 90°) in order to resolve the full current vector. Such measurement pairs can be acquired almost synoptically by aircraft, whereas a single satellite system would collect such data only over

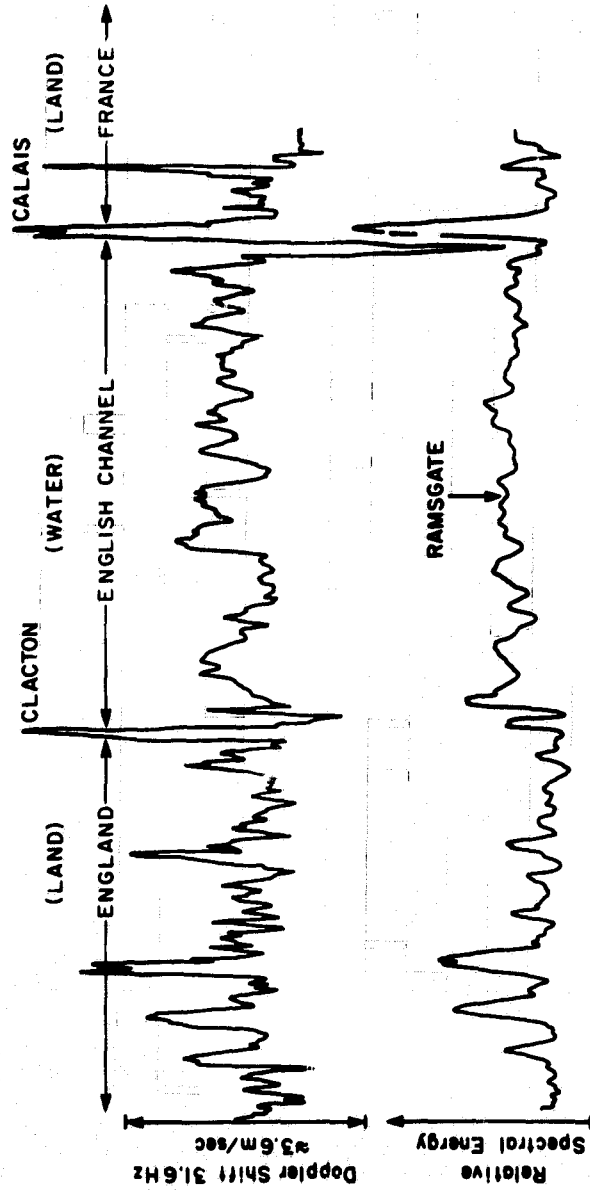


Fig. 8: Continuous Doppler shift and image intensity scans across Fig. 7. (Zero delay, Swath 1)

a number of hours or days, and thus might be restricted to the measurement of longer term mean currents. In principal, it is possible to estimate a second current component perpendicular to the radar line of sight by measuring the degree of defocusing induced; however, these effects may be too subtle for accurate measurement (Shuchman and Zelenka, 1978). The application of the hydrodynamic equation of continuity to a field of radial current components may also lead to resolution of the complete vector field; however, the initial radial vector field must probably be of much higher accuracy than that presently obtainable by this method.

The short discussion which follows outlines the more significant sources of experimental error and their relative importance with regard to aircraft and satellite applications.

6.1 System Sensitivity (Geometry and Doppler Bandwidth)

The radial component of an ocean surface current is given by (refer to Figure 2)

$$v_r = v \sin\theta_A \sin\theta_i$$

where

$$\begin{aligned} v &= \text{the magnitude of the current} \\ \theta_A &= \text{the current direction referred to azimuth} \\ \theta_i &= \text{the radar incidence angle} \end{aligned}$$

The aircraft data examined here was obtained at incidence angles of 30 to 60 degrees, while SEASAT viewed the ocean at a less favorable angle of about 20 degrees.

Furthermore, the ocean current signal v_r and the associated Doppler shift Δf_D for a moving target referred to land must be detected against the background of Doppler shifting induced by the platform motion (V) itself. Assuming that motion is uniform, the bandwidth for a SAR system with azimuth resolution δ is given approximately by (Tomiyasu, 1978)

$$B = \frac{V}{\delta}$$

Thus, a measure of the system sensitivity to ocean surface currents is the ratio of the deviation Δf_D to this Doppler background, given by

$$\frac{\Delta f_D}{B} = \left(\frac{2\delta}{\lambda V} \cdot \sin\theta_i \right) v \sin\theta_A \equiv s \cdot v \sin\theta_A \quad (5)$$

The sensitivity factor s is shown in Table 1 for the SAR's used.

Table 1

The Factor s (Sensitivity to Ocean Surface Currents)
For CV-580 and SEASAT SAR

SAR System	δ (m)	λ (m)	V (m/s)	θ_i (deg)	s (m/s) ⁻¹
CV-580 X-band	3	.032	125	45	1.1
CV-580 L-band	3	.23	125	45	0.15
SEASAT L-band	10	.23	7000	20	0.0042

By this measure, we see that the CV-580 X-band channel is inherently about 7 times more sensitive than the L-band channel, and 250 times more sensitive than the SEASAT system. Values of s larger than 1 cause image suppression due to bandwidth limitations, since this implies that the moving targets are Doppler shifted entirely out of the scene. This is a problem which can be avoided by special processing.

Note also that, in principle, an X-band satellite system with azimuth resolution of about 350 meters would have an s factor equivalent to that of the CV-580 X-band channel.

6.2 Platform Stability

The true velocity vector of an aircraft or satellite-borne radar antenna is not constant in time. In particular, changes in the magnitude and direction of the antenna velocity can result in non-zero velocities and accelerations in the radial direction; this in turn can cause shifts in the Doppler signal history which contaminate the current-induced shifts being sought. Satellite platforms are more stable than aircraft, although it should be noted that some aircraft are equipped with an inertial system which may partially compensate for these contaminations.

6.3 Surface Gravity Waves

Interaction of the short gravity and capillary wave scatterers with the almost periodic orbital motions of longer gravity waves may broaden the Doppler spectrum and/or make it asymmetric. Preliminary observations have detected such asymmetries and broadening, though a detailed study of these effects has not been completed. It should be noted that generally low sea state conditions existed during the collection of data summarized in Figure 4.

6.4 Anisotropic Backscattering

In the course of synthesizing a SAR aperture, a particular

target region is viewed by the radar from differing angles. If the backscattering cross section of that region is anisotropic, the associated Doppler spectrum will not be uniformly weighted for all frequencies. Pertinent examples of such anisotropic scatterers might be surface gravity waves, or the banks of tidal channels. Experiments are planned to determine the effects of this anisotropy on the radar phase history.

7. SUMMARY

Airborne and SEASAT SAR Doppler histories have been examined as a means of estimating ocean surface currents.

For currents in excess of 1 meter/second, airborne X-band SAR measurements of the current speed were found to be about 25 percent lower than the corresponding surface observations. This discrepancy may be due in part to the fact that SAR estimates are spatially averaged instantaneous measurements, while the in situ observations represent temporal averages taken at a point. Additional errors may be introduced into the SAR estimates by platform instability, the presence of surface gravity waves, and target regions with anisotropic backscattering properties.

The SEASAT L-band SAR is poorly suited for this type of measurement, and estimates obtained with this system were in substantial disagreement with tidal current predictions. The poor SEASAT results may be due in part to unfavorable viewing geometry, large Doppler bandwidth induced by high platform speed, and the effects of gravity waves and anisotropic backscatterers. A future satellite SAR system designed for measuring ocean surface currents might be improved using a shorter radar wavelength and a coarser azimuth resolution.

While the aircraft results reported here are encouraging, much more experimental and theoretical work is needed to determine the effects on SAR Doppler spectra of such things as long wave orbital motions, anisotropic backscatterers, and spatially varying surface velocity distributions.

8. ACKNOWLEDGEMENTS

The authors wish to thank the SEASAT SAR experiment team for numerous discussions regarding this work. The SEASAT SAR signal film needed to carry out this research was provided by ERIM and by the SAR Data Processing Center of the Jet Propulsion Laboratory. The special processing needed to extract Doppler information from the SAR data was ably performed by A. Klooster and E. Kasischke at the Environmental Research Institute of Michigan.

The NOAA portion of this research was supported by the NOAA

SEASAT Project, under the management of Mr. John W. Sherman, III.

The ERIM portion of this research was supported by NOAA/NESS-NASA AO Contract No. MO A01-78-00-4322.

REFERENCES

- Raney, R.K. and Shuchman, R.A., 1978, "SAR Mechanism for Imaging Waves," Proc. of Fifth Canadian Symposium on Remote Sensing, Victoria, B.C.
- Rawson, R., Smith, F. and Larson, R., 1975, "The ERIM Simultaneous X- and L-Band Dual Polarized Radar," Proceedings of the IEEE 1975 International Radar Conference, New York, 505.
- Shemdin, O., Jain, A., Hsiao, S.V. and Gatto, L.W., 1980, "Inlet Current Measurement with SEASAT-1 Synthetic Aperture Radar," Shore and Beach, (in press).
- Shuchman, R.A., Klooster, A. and Maffett, A.L., 1978, "SAR Mechanism for Imaging Ocean Waves," Proc. EASTCON '78 Record, IEEE Electronics and Aerospace Systems Convention.
- Shuchman, R.A. and Zelenka, J.S., 1978, "Processing Ocean Wave Data from a Synthetic Aperture Radar," Boundary Layer Meteorology, 13, 181-191.
- Shuchman, R.A., Rufenach, C.L., Gonzalez, F.I. and Klooster, A., 1979, "The Feasibility of Measurement of Ocean Surface Currents Using Synthetic Aperture Radar," Thirteenth International Symposium on Remote Sensing of the Environment, Ann Arbor, Michigan.
- Tomiyasu, K., 1978, "Tutorial Review of Synthetic Aperture Radar (SAR) with Applications to Imaging of the Ocean Surface," Proceedings of the IEEE, Vol. 66, No. 5.

SEASAT SAR OCEAN SURFACE CURRENT AND
SHALLOW WATER WAVE REFRACTION

John G. Hayes
Global Scientific, Inc.
Concord, Massachusetts 01741, U.S.A.

formerly of
Environmental Research & Technology, Inc.
Concord, Massachusetts 01742, U.S.A.

Robert A. Shuchman
Environmental Research Institute of Michigan (ERIM)
Radar and Optics Division
Ann Arbor, Michigan 48107, U.S.A.

1. ABSTRACT

The propagation of gravity waves and the wave-current interaction phenomenon has been studied with SEASAT synthetic aperture radar (SAR) data obtained along the east coast of the United States near Cape Hatteras, North Carolina. Particular attention is focused on SEASAT Revolution 974, where the meteorological conditions, wave generation in deep water and the resulting wave field are discussed and compared to a numerical shallow water wave model.

The resulting coastal wave data results show a reasonable representation of the refraction pattern near Cape Hatteras. Optical Fourier Transforms (OFT) and Fast Fourier Transforms (FFT) generated in deep and shallow water are compared with the resulting measured and modeled wave field. Results indicate that the SAR is a valuable instrument for current and wave detection and particularly for wave-current interaction studies. Wave length versus water depth inversion techniques have shown encouraging results for using SAR data in determining bathymetric structures.

2. INTRODUCTION

Remote sensing techniques have recently become an increasingly

important tool in the oceanic sciences, especially in the detection of ocean waves, currents and oceanic bottom features. The imagery collected from a specialized form of a side looking imaging radar called SAR flown on SEASAT was examined for these phenomena. A limited data set of SAR imagery obtained for Revolution 974 along the east coast of the United States, near Cape Hatteras, North Carolina, showed particularly interesting wave patterns including interaction or the refraction of surface waves by the Gulf Stream and shoaling due to the bathymetry (Figure 1).

Analysis of OFT produced estimates of wave length and wave direction for several sites in deep water, in the Gulf Stream and in shoaling waters. These data and the FFT information of all dominant wave periods and directions were input for a wave refraction and ocean current numerical model. The resulting wave rays, including the interaction of the wave field with the ocean current and the

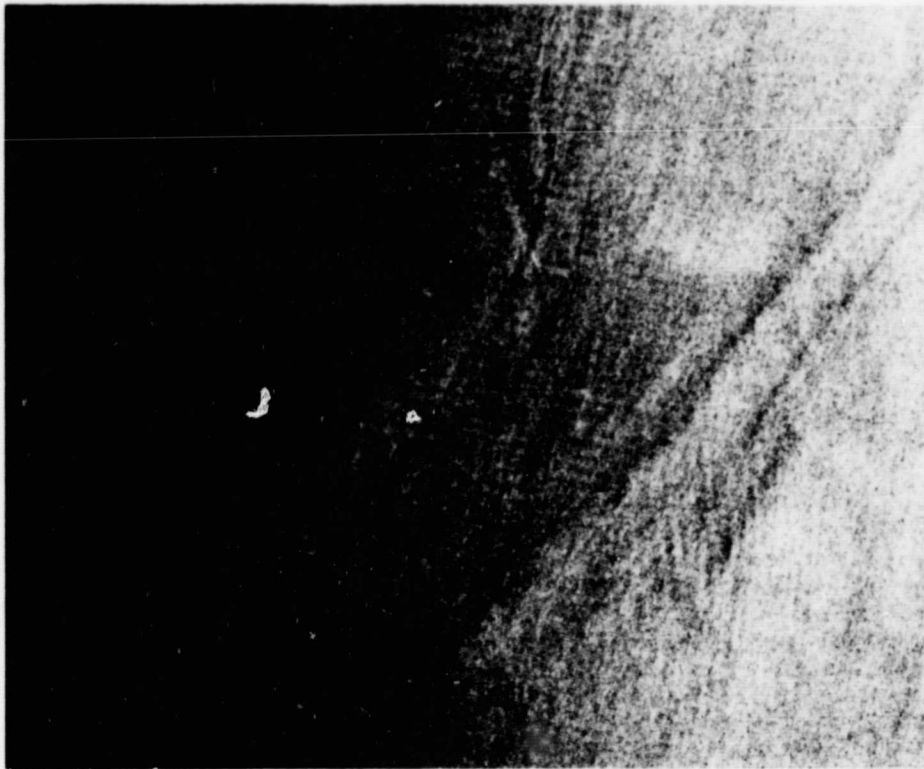


Fig. 1: SEASAT SAR Digital Image (100 x 100 km area) of Cape Hatteras Region.

shallow water refraction were compared to SAR FFT's and surface measurement.

3. OPTICAL AND DIGITAL FOURIER TRANSFORMS

Anticipating the necessity of optically processing SEASAT SAR data, ERIM investigated means of optically extracting wave information. The methods that appear to hold the most promise are based on the two-dimensional Fourier transform. Wave parameters which can be inferred from the Fourier transform of the corrected SAR data are wavelength, wave direction, and spatial uniformity (straightness of the wavefronts, amount of refraction, number of wave directions, and continuity of wavefronts). The optical two-dimensional transform is simply achieved by Fraunhofer diffraction, as reported by Shuchman, et al (1977).

In addition to approximately 80 OFT's made of the Cape Hatteras data, eight fast Fourier transforms were made on the digital data (Figure 1) processed by the Jet Propulsion Laboratory. The range coordinates of the digital data were analytically corrected for slant-to-ground geometry (Feldkamp, 1978). Subsections of 9.2 km x 9.2 km with 18 meter resolution were extracted from the digital data. The 18 meter pixel spacing were converted to 36 meter data by 4 pixel averaging in order to increase the coherence in the image. The average value of each azimuthal line was subtracted from the line to remove the trend of intensity falloff with increasing range distance. Two-dimensional fast Fourier transforms were performed on each 256 x 256 cell subsection to yield raw directional wave number spectra with a Nyquist wave number of 0.09 M^{-1} . The raw spectra were smoothed by replacing each value with the average of the surrounding 5 x 5 cell. The approximate number of degrees of freedom for the resulting spectrum is 142 (Kinsman, 1965). The 99% confidence limits are then $\pm 1.5 \text{ dB}$ (Jenkins and Watts, 1968). Figure 2 is an example of deep water spectra obtained approximately 80 km due west of Cape Hatteras.

4. WAVE REFRACTION

The Cape Hatteras data (Revolution 974) demonstrated the capability of the SEASAT SAR to image shallow water gravity waves undergoing refraction, and the interaction of the Gulf Stream with the wave field.

A graphical wave refraction diagram was drawn using the local bathymetry of the Cape Hatteras region and compared to the SAR derived wave orthogonals (Figure 3). The solid lines on the figure were constructed using classical methods outlined by Johnson, et al (1948) with the deep water wave length and direction information being obtained from the ERIM OFT's. The dotted lines were SAR derived, coming from the OFT and FFT analysis. Care was taken to begin the refraction landward of the Gulf Stream boundary so that

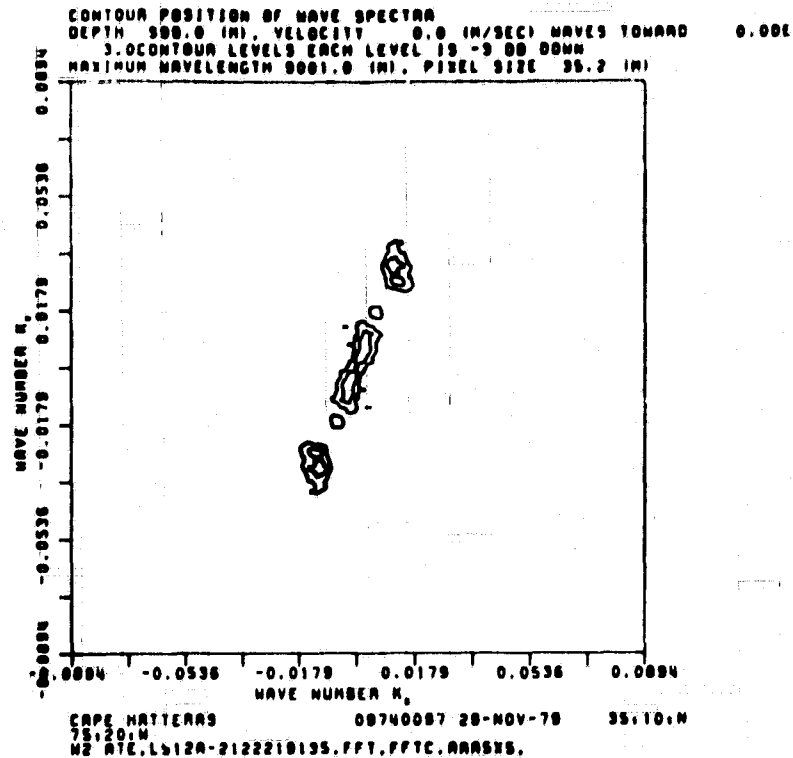


Fig. 2: Contour Plot of Fast Fourier Transform of Deep water Spectra.

the effect Gulf Stream current on wave refraction would not enter into the comparison. In general, the comparison between the refraction diagram and the SAR derived orthogonals is good.

To carry the refraction study one step further, a wave refraction and ocean current refraction model developed by Hayes (1977, 1980) was employed to compare the results of the OFT and FFT data to surface measurements.

The basis for the ocean current interaction study lies in early work by Johnson (1948) which pointed out that major ocean currents such as the Gulf Stream may have an appreciable effect on the height, length, and direction of waves approaching the shore and, under some circumstances, may cause almost complete reflections.

Also, Kenyon (1971) points out that this phenomenon of wave-current interaction may cause trapping of waves at certain incident

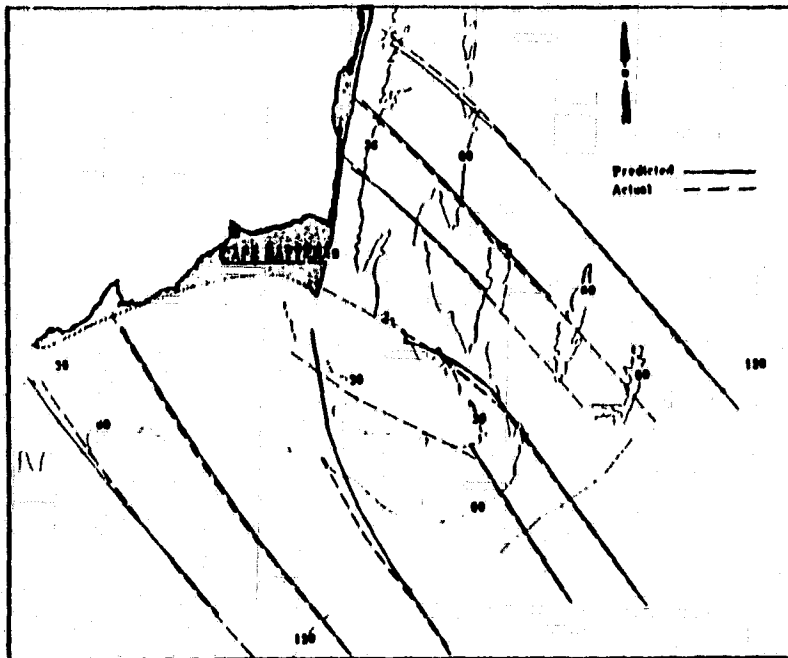


Fig. 3: Actual SAR-Derived (dotted lines) versus predicted (solid lines) orthogonals for SEASAT Revolution 974 (depth in feet on figure).

angles. He also shows that the radius of curvature is a characteristic length scale for the refraction and that it decreases with increasing current vorticity and with decreasing group speed relative to the current. He continues, "For waves that propagate with (against) a variable current, the rays will bend in the direction of decreasing (increasing) current speed. Therefore, under the right conditions, it is possible for waves that propagate with (against) a current to be trapped about a local minimum (maximum) in current speed. It is also possible that waves that propagate with (against) a current could be reflected from a local maximum (minimum) in current speed."

Longuet-Higgins and Stewart (1960) show the change in angle of a refracted wave to be the same as that reported by Johnson (1948); that is,

$$\sin \theta = \frac{\sin \theta_0}{(1 - (V/C_0) \sin \theta_0)^2}$$

where θ is the refracted angle, θ_0 is the incident angle, V is the current speed, and C_0 is the incident phase velocity.

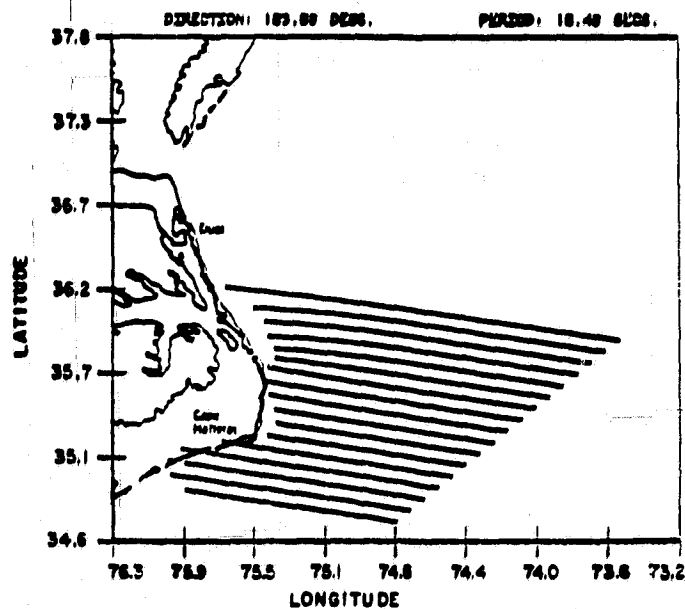


Fig. 4: Sample wave refraction diagram without the Gulf Stream.

OFT and FFT periods and directions were first input to the wave-current model and wave rays were produced without consideration for refraction due to the Gulf Stream (Figure 4). The resulting angles and wave spectra were linearly recombined (Kinsman, 1965) in shallow water and along the ray paths and compared to other FFT spectra. The results indicated that the magnitude and direction of the model runs did not compare favorably to the FFT's produced in the Gulf Stream and in shoaling waters. Therefore, the rays were initialized again, this time including a non-uniform current distribution (Hayes 1980). The resulting rays (Figure 5 and 6) illustrate the bending of the wave rays due to the shear produced by the wave-current interaction. When the recombined shallow water spectra, which included the modeled Gulf Stream, were compared to the SAR FFT's in shallow water, the directional resolution compared more favorably than cases without the modeled current.

Therefore, the results illustrated here indicate that the SAR apparently has the ability to image the effect of ocean currents as well as of shallow water and deep water refraction.

5. ACKNOWLEDGEMENTS

The ERIM portion of this work was supported by NOAA/NESS - NASA AO Contract No. MO-A01-78-00-4339.

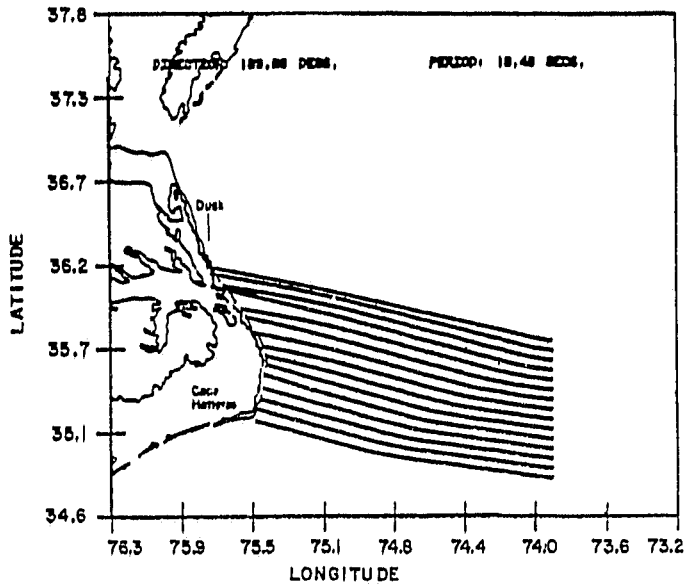


Fig. 5: As for Figure 4 with the Gulf Stream included, at a period of 10.40 seconds.

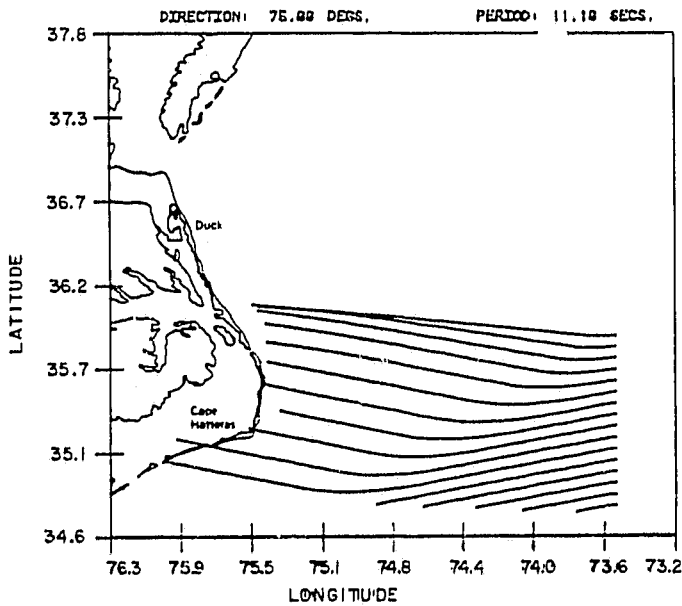


Fig. 6: As for Figure 4 with the Gulf Stream included, at the peak period of the NOAA Data Buoy (11.1 seconds).

The remaining portion of the work was supported by NOAA/NESS AO Contract No. 78-4338.

REFERENCES

- Feldkamp, G.B., 1978, "Correction of SAR-Induced Distortion in SEASAT Imagery," Paper for SPIE Conference on Applications of Digital Image Processing, San Diego, California, August.
- Hayes, J.G., 1977, "Ocean Current and Shallow Water Wave Refraction in an Operational Spectral Ocean Wave Model," Technical Note No. 77-1, Fleet Numerical Weather Central, Monterey, Calif.
- Hayes, J.G., 1980, "Ocean Current Wave Interaction Study," Journal of Geophysical Research (Ocean and Atmospheres), 85, No. 9, 5025-5031, Sept.
- Jenkins, A.M. and Watts, D.G., 1968, "Spectral Analysis and Its Applications," Holden-Day, San Francisco, California, 525pp.
- Johnson, J.W., O'Brien, M.P. and Isaacs, J.D., 1948, "Graphical Construction of Wave Refraction Diagrams," U.S. Navy Hydrographic Office, H.O. Pub. 605, 45pp.
- Kenyon, K.E., 1971, "Wave Refraction in Ocean Currents," Deep-Sea Res., 18, 1023-1034.
- Kinsman, B., 1965, "Wind Waves— Their Generation and Propagation on the Ocean Surface," Prentice-Hall, Englewood Cliffs, N.J., 676pp.
- Longuet-Higgins, M.S. and Stewart, R.W., 1960, "Changes in the Form of Short Gravity Waves on Long Waves and Tidal Currents," J. Fl. Mech., 8, 565-583.
- Shuchman, R.A., Jackson, P.L. and Feldkamp, G.B., 1977, "Problems of Imaging Ocean Waves with Synthetic Aperture Radar," ERIM Report No. 124300-1-t, Environmental Research Institute of Michigan, Ann Arbor, Michigan, 111pp.